

A STUDY OF CRACK-INCLUSION INTERACTION USING MOIRÉ
INTERFEROMETRY AND FINITE ELEMENT ANALYSIS

Except where reference is made to the work of others, the work described in this thesis is my own or was done in collaboration with my advisory committee. This thesis does not include proprietary or classified information.

Piyush Chunilal Savalia

Certificate of Approval:

Jeffrey C. Suhling
Quina Distinguished Professor
Mechanical Engineering

Hareesh V. Tippur, Chair
Alumni Professor
Mechanical Engineering

Robert L. Jackson
Assistant Professor
Mechanical Engineering

Stephen L. McFarland
Acting Dean
Graduate School

A STUDY OF CRACK-INCLUSION INTERACTION USING MOIRÉ
INTERFEROMETRY AND FINITE ELEMENT ANALYSIS

Piyush Chunilal Savalia

A Thesis

Submitted to

the Graduate Faculty of

Auburn University

in Partial Fulfillment of the

Requirements for the

Degree of

Master of Science

Auburn, Alabama
December 15, 2006

A STUDY OF CRACK-INCLUSION INTERACTION USING MOIRÉ

INTERFEROMETRY AND FINITE ELEMENT ANALYSIS

Piyush Chunilal Savalia

Permission is granted to Auburn University to make copies of this thesis at its discretion upon request of individuals or institutions and at their expense. The author reserves all publication rights.

Signature of Author

Date of Graduation

VITA

Piyush Savalia, son of Chunilal and Kanchan Savalia, was born on December 13, 1979, in Gujarat, India. He earned a Bachelor's degree in Mechanical Engineering from Sardar Patel University, Vallabh Vidyanagar, India in 2002 with first class. After Graduation he worked for Videocon Narmada Glass, a manufacturer of panels and funnels for glass picture tubes in TV, in company's captive power plant division as a graduate engineer trainee. In August 2003, he began his graduate study in Mechanical Engineering at Auburn University. He joined Dr. Hareesh V. Tippur's research group in January 2004, as a Graduate Research Assistant. He also worked as a Graduate Teaching Assistant for the undergraduate course of Mechanics of Materials at Department of Mechanical Engineering.

THESIS ABSTRACT

A STUDY OF CRACK-INCLUSION INTERACTION USING MOIRÉ INTERFEROMETRY AND FINITE ELEMENT ANALYSIS

Piyush Chunilal Savalia

Master of Science, December 15, 2006
(B. E., Sardar Patel University, Vallabh Vidyanagar, India, 2002)

131 Typed Pages

Directed by Hareesh V. Tippur

Failure of composite materials is intrinsically linked to the fundamental problem of a matrix crack interacting with a second phase inclusion. In this work, the critical issue of matrix-inclusion debonding in the presence of a nearby crack is addressed experimentally and numerically. Optical measurement of surface deformations in the vicinity of a crack-inclusion pair is carried out using moiré interferometry. The measurements are used to validate an approach for simulating evolution of inclusion-matrix debonding. The numerical model is subsequently used to parametrically study crack-inclusion interactions.

In the first phase of this work, a process based on microlithography is developed for creating master gratings on silicon wafers. Two methods are then developed to transfer gratings to polymeric specimens. Edge cracked epoxy beams, each with a

cylindrical glass inclusion ahead of the crack tip, are fabricated to experimentally model crack-inclusion interactions. A moiré interferometer for mapping displacement fields in the crack-inclusion vicinity is developed. Debonding of an inclusion from the surrounding matrix is detected successfully by the interferometer. The measured displacements are analyzed to estimate surface strains and study the evolution of strain fields associated with crack-inclusion debonding phenomenon. The associated effects on fracture parameters namely, crack mouth opening displacements (CMOD), crack mouth compliance, mode – I stress intensity factors (SIF) and energy release rates (ERR), are extracted. A sharp rise in crack mouth compliance values and strains in the close vicinity of the inclusion due to debonding is observed.

Next, a finite element model is developed to simulate the experimentally observed behavior. Interfacial debonding between the matrix and the inclusion is simulated using the element stiffness deactivation method. A failure criterion based on a critical radial stress is shown to capture the onset and progression of debonding and finite element results are in good agreement with measurements. A follow up parametric study is performed to examine effects of inclusion size and inclusion proximity to the crack tip. The results show that debonding is delayed as the inclusion size increases for a constant L/d ratio where L and d are crack tip-inclusion distance and inclusion diameter, respectively. For a constant L , debonding occurs at lower loads for larger inclusions along with higher crack mouth compliance following inclusion-matrix debonding.

ACKNOWLEDGEMENTS

I would like to thank my academic advisor, Dr. Hareesh V. Tippur for the financial support and constant guidance throughout this work. Special thanks are due to Madhusudhana Kirugulige, a doctoral candidate in our group and Charles Ellis, the lab manager of Alabama Microelectronics Science and Technology Center (AMSTC), at Auburn University's Department of Electrical Engineering. Madhu's help throughout my stay at Auburn in many aspects is greatly appreciated. He introduced me to many techniques and methods in the laboratory. His expertise and suggestions regarding the finite element analysis issues were very helpful. This work would not have been possible without cordial help by Charles. His suggestions and expertise in microelectronics fabrication processes were of immense help. It was great to work with Dr. Rajesh Kitey, a recent graduate and Taylor Owens, a master's candidate in our group. Thanks are due to my thesis committee members Dr. Jeff Suhling and Dr. Robert Jackson for reviewing this work. I am very thankful to all my friends in Auburn and my cousin Dr. Jignesh Dholaria for their constant support and for not letting me miss my family throughout my stay at Auburn. I am indebted to my parents for their financial support and constant moral support during my course of study at Auburn. Without their constant encouragement and love it would not have been possible for me to do this work. I dedicate this work to my parents.

Style manual or journal used Discrete Mathematics (together with the style known as “auphd”).

Computer software used The document preparation package Microsoft Word 2002 . SigmaPlot2001 was used for plotting the graphs.

TABLE OF CONTENTS

LIST OF FIGURES	xi
LIST OF TABLES	xv
1. INTRODUCTION	1
1.1 Composite materials: An overview.....	1
1.2 The crack-inclusion interaction problem	4
1.3 Background and literature survey	6
1.4 Objectives	10
1.5 Organization of the thesis	12
2. GRATINGS FABRICATION AND TRANSFER TECHNIQUES	13
2.1 Master gratings fabrication	15
2.2 Grating transfer methods.....	21
2.2.1 Direct grating transfer from a silicon master	21
2.2.2 Grating transfer using silicone rubber submasters.....	23
2.3 Crack-inclusion specimen fabrication.....	27
2.4 Materials characteristics.....	29
3. MOIRÉ INTERFEROMETRY.....	32
3.1 Experimental Setup.....	33
3.2 Deformation field mapping.....	37

3.3 Interference of plane waves	37
3.4 In-plane moiré interferometry.....	40
3.5 Benchmark experiment	46
4. CRACK-INCLUSION INTERACTION	53
4.1 Interaction between crack and inclusion.....	53
4.2 Fracture parameters and strains	56
4.3 Experimental repeatability	61
5. FINITE ELEMENT MODELING	63
5.1 FEA model description	64
5.2 Inclusion-matrix debonding	66
5.3 Effect of β on debonding	70
5.4 Convergence study.....	77
5.5 Parametric study.....	79
5.5.1 Constant L/d ratio: Effect of inclusion size.....	79
5.5.2 Varying L/d ratio: Crack-inclusion proximity effect	85
5.6 Estimation of glass-epoxy interface strength.....	90
6. CONCLUSIONS	94
BIBLIOGRAPHY.....	97
APPENDICES	100
A. ANSYS APDL Macros	101
B. Analysis of uncracked beam with inclusion.....	114

LIST OF FIGURES

Figure 1.1 : Some applications of composite materials and relevance of the crack-inclusion interaction study.	3
Figure 1.2 : Schematic of a matrix crack interacting with an inclusion.	5
Figure 2.1 : (a) LASI window showing mask design (b) Enlarged view of the gratings design in LASI (c) Mask (Ronchi gratings) made according to the design. 14	
Figure 2.2 : (a) Wafer cleaning. (b) Dehydration bake.	15
Figure 2.3 : (a) HMDS application. (b) Photoresist application.	17
Figure 2.4 : (a) Soft baking of the wafer. (b) The mask aligner showing the mask and The wafer. (Mask is held in the frame by vacuum.)	17
Figure 2.5 : (a) Photoresist development (b) Rinsing (c) Drying (d) Inspection under microscope.	18
Figure 2.6 : STS Multiplex ICP used to etch silicon.	19
Figure 2.7 : Micrographs of silicon wafer gratings (a) Cross section. (b) Front view.....	19
Figure 2.8 : Schematic of steps involved in fabrication of silicon wafer gratings.....	20
Figure 2.9 : Aluminum coated silicon wafer gratings.....	21
Figure 2.10: Direct transfer of gratings from silicon wafer with aluminum coating.....	22
Figure 2.11: Silicone rubber casting molds and submasters.....	24
Figure 2.12: Steps involved in fabrication of silicone rubber submaster grating and transferring grating pattern onto specimen surface. (Note: specimen and grating are shown in the thickness dimension)	25
Figure 2.13: Micrographs of (a) Cross-section of a silicone rubber submaster (b) Front view of epoxy gratings transferred using a silicone rubber submaster.	26

Figure 2.14: (a) Specimen preparation, (b) Specimen geometry and loading configuration.....	28
Figure 2.15: (a) Notch-sharpening setup. (b) Sharp-crack: front-side view of the specimen. (c) Sharp-crack: back-side view of the specimen.....	30
Figure 2.16: Stress-strain response of neat epoxy.	31
Figure 3.1 : Schematic of moiré interferometer.....	34
Figure 3.2 : 3-D representation of the moiré interferometry setup.....	35
Figure 3.3 : Photograph of moiré interferometry setup.	36
Figure 3.4 : Interference of plane waves. (a) Plane wave propagation. (b) Geometry and (c) Intensity on the image plane.....	37
Figure 3.5 : Diffraction from a grating.	40
Figure 3.6 : Moiré interferometry principle.....	43
Figure 3.7 : Double exposure moiré interferometry principle.....	44
Figure 3.8 : Neat epoxy three-point bend sample.....	46
Figure 3.9 : Interferograms showing evolution of opening displacement field around the crack-tip in neat epoxy sample. (Sensitivity = 1.25 μm /half-fringe).....	47
Figure 3.10: Results from benchmark study: (a) Variation for CMOD with load. (b) Variation of mode –I SIF with load.....	49
Figure 3.11: Comparison of strain distribution in neat epoxy sample along line $x \sim 3$ mm ($L = 5$ mm, and indicated by ‘ m ’) from moiré data and finite element analysis.....	52
Figure 4.1 : Crack-inclusion specimen geometry loading configuration and crack-tip coordinate system.....	54
Figure 4.2 : Selected moiré interferograms of crack-inclusion specimen before debonding occurs between inclusion and matrix.....	54
Figure 4.3 : Selected moiré interferograms of crack-inclusion specimen after Debonding between inclusion and matrix.....	55

Figure 4.4 : Comparison between experimentally obtained crack mouth opening displacements for the crack-inclusion and neat epoxy specimens with load.	56
Figure 4.5 : Comparison of experimentally obtained variation of crack mouth compliance with applied load for crack-inclusion and neat epoxy specimens.	57
Figure 4.6 : Variation of mode-I SIF with load for crack-inclusion specimen.	58
Figure 4.7 : Strain field evolution along ($x/L \sim 0.6, y/L$) (shown by line 'm') during the loading phase.	59
Figure 4.8 : CMOD variation with load for two different crack-inclusion specimens.	61
Figure 4.9 : Crack compliance variation with load for two different crack-inclusion specimens.	62
Figure 5.1 : (a) Finite element mesh used for simulating crack-inclusion interaction in a three-point bend specimen (b) Enlarged view of the mesh in the vicinity of crack-tip and inclusion.	65
Figure 5.2 : Crack tip and inclusion coordinate systems.	66
Figure 5.3 : Analysis methodology for debond simulation using ANSYS APDL.	68
Figure 5.4 : (a) Variation of radial stress variation around the inclusion for $b = 0.12$ (applied load P is normalized by P_0 , the load corresponding to tensile failure of an uncracked neat epoxy beam).(b) CMOD variation for various β values (eq. (5.1)) used in finite element simulations and comparison with experimental results. ($L/d = 1.31, d = 4$ mm)	69
Figure 5.5 : Crack mouth compliance comparison between experimental and FEA data.	70
Figure 5.6 : Strain field evolution along ($x \sim 3$ mm, y) (shown by line 'm') for (a) pre-debonding and (b) post-debonding stages.	71
Figure 5.7 : Crack opening displacement field from finite element analysis showing perturbed displacement contours in the crack-inclusion vicinity. (a) Before debonding (b) After debonding. Contours levels are approximately same as the experimental ones. ($a = 8.5$ mm, $d = 4$ mm, $L/d = 1.31, \beta = 0.14$).	73
Figure 5.8 : Energy release rate variation with applied load.	74

Figure 5.9 : Normal Strain evolution along line ‘ <i>m</i> ’ (a) ε_x (b) ε_y	75
Figure 5.10: Evolution of (a) Shear strain ε_{xy} (b) Von-Mises stress along line ‘ <i>m</i> ’.....	76
Figure 5.11: Validation of CMOD with load for different bond layer element sizes.....	78
Figure 5.12: CMOD variation with load for <i>L/d</i> ratio of 1.31.....	80
Figure 5.13: Variation of crack mouth compliance with respect to applied load. (<i>L/d</i> =1.31).....	81
Figure 5.14: Crack mouth compliance values for different inclusion diameters (<i>L/d</i> = 1.31).	81
Figure 5.15: Energy release rates for different diameter inclusions (<i>L/d</i> = 1.31).....	82
Figure 5.16: Strain (ε_y) evolution along line ‘ <i>m</i> ’ for <i>L/d</i> =1.31 (a) Before debonding (<i>P/P_o</i> = 0.023) (b) After debonding (<i>P/P_o</i> = 0.30). (Note: <i>a</i> = 8.5 mm.).....	84
Figure 5.17: Variation of crack mouth opening displacement with the applied load.....	85
Figure 5.18: Variation of crack mouth compliance with the applied load.....	86
Figure 5.19: Steady state and maximum values of crack mouth compliance with variation of <i>L/d</i> ratio.	87
Figure 5.20: Energy release rates for different <i>L/d</i> ratios.....	88
Figure 5.21: Strain (ε_y) evolution along line ‘ <i>m</i> ’ for <i>L</i> = 5 mm. (a) Before debonding (<i>P/P_o</i> = 0.023) (b) After debonding (<i>P/P_o</i> = 0.30).	89
Figure 5.22: Schematic of specimens and loading configuration used for estimating glass-epoxy bond strength. (Note: All dimensions are in mm.)	90
Figure 5.23: Silicone rubber molds cast on a flat surface.....	91
Figure 5.24: Experimental setup for glass-epoxy interfacial strength measurement.....	92
Figure B.1 : Radial stress in the bond layer elements at different load levels.....	115
Figure B.2 : Opening displacement field in uncracked beam with inclusion. (a) Before debonding (<i>P/P_o</i> = 0.12) (b) After onset of debonding (<i>P/P_o</i> = 0.30).....	116

LIST OF TABLES

Table 2.1: Elastic properties of matrix and inclusion.....	27
Table 5.1: Geometric parameters used for study with a constant L/d ratio.....	80
Table 5.2: Geometric parameters used for studying effect of L/d ratio.....	85
Table 5.3: Glass-epoxy interfacial failure strength data.....	92

CHAPTER 1

INTRODUCTION

1.1 Composite materials: An overview

Structures made of composite materials have been used over the millennia by mankind. Adobe bricks are the earliest known composite materials used by Israelites by mixing in which straw (a fibrous material) with clay (a binder with strong compressive strength). The straw promotes water in the brick to evaporate and distribute cracks in the clay evenly resulting in improved strength. Ancient Egyptians used plywood to enhance the strength by exploiting grain structure and resistance to hygro-thermal expansion.

In many modern engineering applications such as civil aviation, space exploration and microelectronics structural members are exposed to harsh environments during service. Engineered materials in general and composite materials in particular offer solutions in such demanding situations. A composite member made of two or more different material phases on microscopic/macroscopic scales, utilizes beneficial mechanical and thermal characteristics of individual phases to get the desired overall behavior. Broadly, composite materials are classified into the following categories [1]:

- (1) Fibrous composites,
- (2) Laminated composites,
- (3) Particulate composites,

(4) Combination of some or all of previous three types.

In general a structure made of a composite material contains a binder material known as the matrix phase and one or more reinforcing phases at the microscopic scale. The secondary phase can be in the form of long fibers, whiskers or particles of different geometries.

Long fibers (very high length-to-diameter ratio) generally being much stiffer and stronger than the bulk material have found applications in fiber reinforced composite materials. For example, strength of commercially available micron size glass fibers is almost 140 to 240 times that of bulk glass. Common fiber reinforced plastics (FRP) generally contain fibers such as carbon, boron or glass oriented in either unidirectional or multidirectional architecture and bonded together by a polymer such as epoxy, polyester, etc. They offer high strength-to-weight and strength-to stiffness ratios along with good impact and fatigue resistance crucial to aerospace and military applications. Accordingly, investigation of failure of fiber reinforced composites at various length scales have received much attention in recent years.

Particle reinforced metal matrix composites (MMC) (such as, aluminum matrix reinforced with silicon carbide (SiC) or titanium carbide (TiC) particles) have shown great potential for many elevated temperature applications. As the name suggests particulate composites involve discrete filler/reinforcement phase/s in a binder unlike continuous fibers in FRPs. The use of particulates enables a cost effective production of this class of composites while offering flexibility in terms of filler size, volume fraction, shape and distribution to alter properties for a given application. Additionally, the macroscopic isotropy of these composites greatly simplifies the mechanical design. The

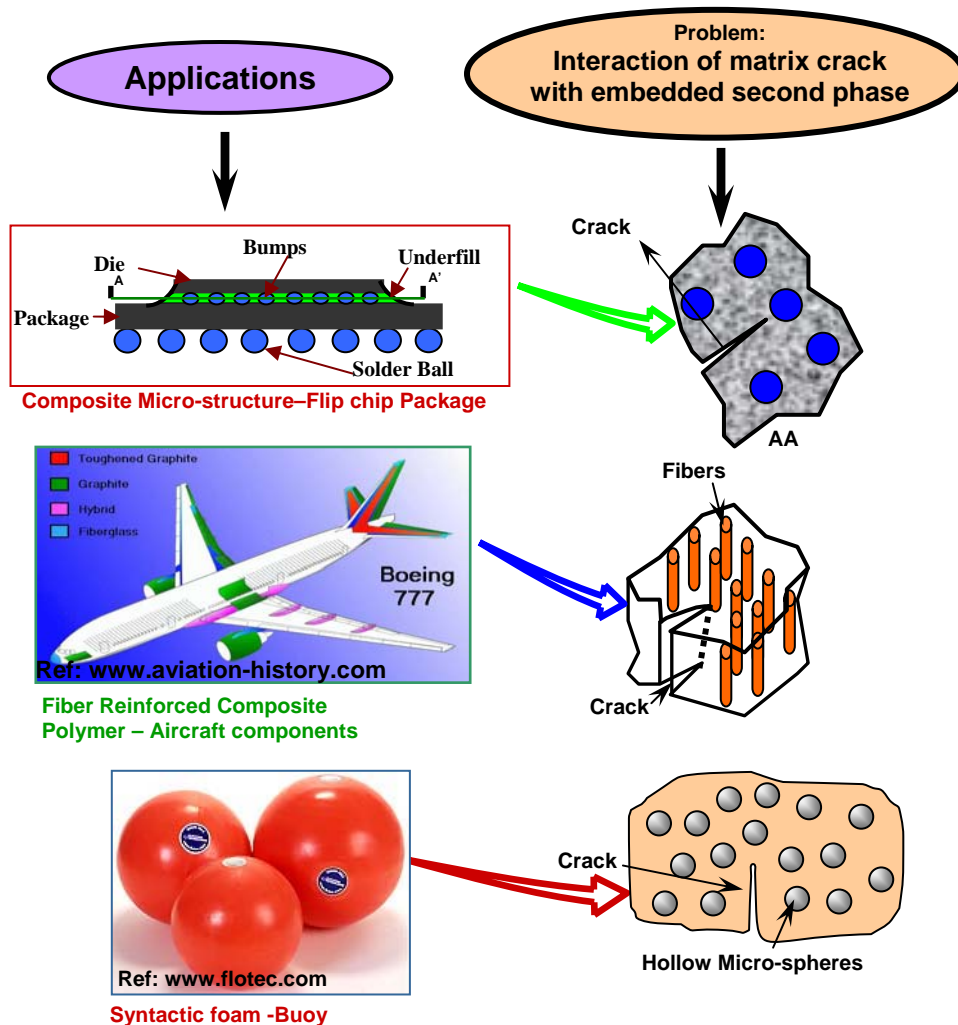


Figure 1.1: Some applications of composite materials and relevance of the crack-inclusion interaction study.

filler particles could also be either metallic (aluminum, silver, etc.) or non-metallic (alumina, silica, etc.). For example, structural syntactic foam (Kirugulige *et. al.* [8]) is a type of particulate composite in which prefabricated micro hollow spheres are dispersed in a binder. In these foams porosity is microscopic unlike conventional foams and can be varied by controlling the size and the density of hollow spheres in the matrix during

fabrication. Among the typical applications of syntactic foams are the high compression applications such as undersea probes and marine platforms. The electronics industry also utilizes particulate composites as underfill materials which are generally silica-filled epoxy or urethane compounds are used to relieve stresses in electrical interconnects such as solder ball grid array (BGA). One of the recent advances in particulate composites is the development of the so-called Functionally Graded Materials (FGM) having directional variations of their thermo-mechanical properties. This is achieved by varying the volume fraction (and/or other micro-structural features) along a desired direction during material processing. Techniques such as slip casting [2], centrifugal casting [3], laser alloying and cladding [4], plasma-spray forming [5] and gravity casting [6, 7] have been used successfully to fabricate such materials.

By combining of one or more types of composites discussed above gives numerous variations of materials for structural applications. In view of these, it is important to study failure of these materials in order to predict their thermo-mechanical performance and reliability during service. Figure 1.1 shows some of the common applications discussed in the previous section along with representative insets where potential crack-inclusion interactions are possible. These generally include a matrix crack interacting with a filler phase such as a reinforcing fiber or a particle.

1.2 The crack-inclusion interaction problem

The fundamental problem of a matrix crack interacting with a second phase inclusion is of vital interest to researchers due to the increasing use of composite materials and their complex failure behavior. Generally, the mechanical behavior of

composite materials depends mainly on properties of the individual phases involved and the strength of the bond between them. As shown in Fig. 1.2 the intrinsic failure process under the influence of a pre-existing or a service induced flaw (such as a crack) can be explained by studying a simplified problem of a matrix crack interacting with the second phase which can be a fiber or a particle. Simplifying the problem in this manner facilitates parametric investigation of the problem for possible material design. Some of these variations include (a) the geometry and the size of the inclusion, (b) the orientation of the inclusion with respect to the crack, (c) the mismatch between elastic properties of

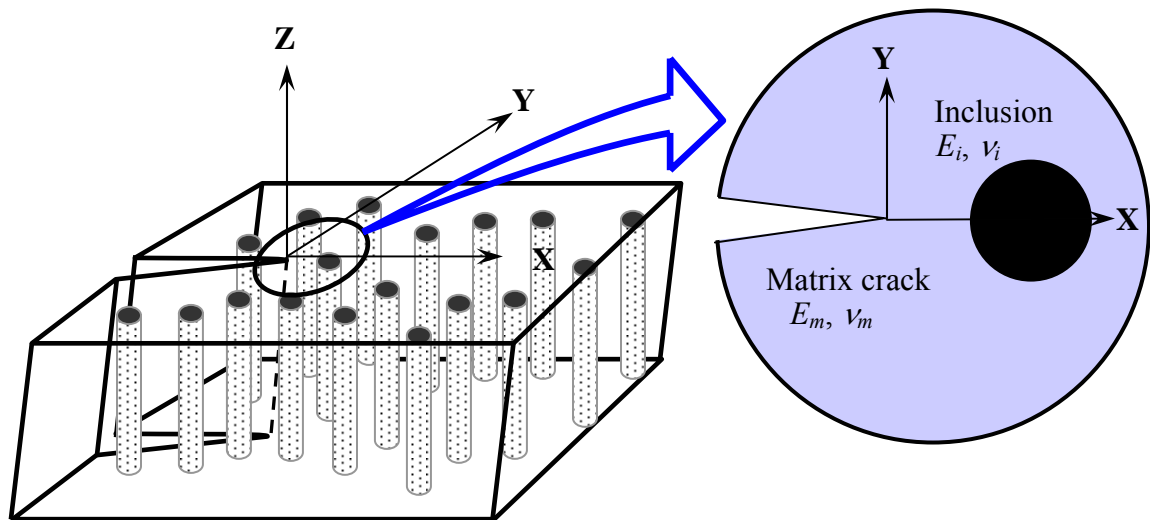


Figure 1.2: Schematic of a matrix crack interacting with an inclusion.

the matrix (E_m, ν_m) and the inclusion (E_i, ν_i), (d) effects of bond strength between the inclusion and the matrix and (e) a crack interacting with multiple inclusions.

1.3 Background and literature survey

Several investigations of the aforesaid problem have been carried out from both analytical and numerical perspectives since the early study of its kind by Tamate [9]. Using Mushkelishvili's complex potentials, he studied the interaction of a radial matrix crack with a circular inclusion in a uniaxially loaded plate. He showed that a relatively stiff inclusion ahead of a compliant matrix reduces the stress intensity factors whereas a compliant inclusion ahead of a stiff matrix crack increases the same. Atkinson [10] investigated the problem of a crack outside a perfectly bonded elastic inclusion under uniaxial and biaxial tensions for different crack lengths and elastic properties of the inclusion and the matrix. He solved singular integrals numerically to obtain the stress intensity factor variations as a function of the distance between the inclusion and the crack tip. Erdogan *et. al.* [11] investigated interaction between a circular inclusion and an arbitrarily oriented crack using Green's functions. They developed expressions for mode-I and mode-II stress intensity factors in terms of asymptotic values of density functions of integral equations which are given in terms of crack face displacements. Gdoutos [12, 13] studied interaction between a crack and a hole or a perfectly bonded inclusion in an elastic medium under uniform tension. He investigated critical values of the applied stress for crack extension and initial crack extension angle in both the cases and reported that rigid inclusion increases the fracture strength of the plate while the opposite occurs in case of a hole. He also later studied stable crack growth when a crack is oriented along a diameter of the inclusion using strain energy density theory. The investigation included dependence of the stable crack growth on loading rate and showed that critical value of failure stress decreases as the number of loading steps decreases (i.e. at higher loading

rates) and lower loading rates results in a more stable crack growth. Kunin and Gommerstadt [14] used projection integral equation approach for studying a crack-inclusion system and developed a relationship between J and M (where J is the energy release rate and M is the interaction integral) integrals for translation of the inclusion with respect to the crack and the effect of the inclusion size. Hasebe *et. al.* [15], studied stress fields when debonding occurs between a rigid circular inclusion from the matrix and the resultant interfacial crack in an infinite plate loaded in uniform tension. They modeled the phenomena as a mixed boundary value problem and reported stress intensities at debond tip. Patton and Santare [16] investigated interaction of a crack with elliptical inclusions. They examined the problem using Mushkhelishvili's complex potentials and used them to formulate singular integral equations for crack opening displacement and solved for stress intensity factors numerically. They studied the problem of a straight crack near a rigid inclusion in an infinite medium. It was observed that for relatively flat elliptical inclusions and radially oriented crack with respect to the inclusion, as the crack rotates towards the flat side of the inclusion the crack tip stress intensity decreases drastically. Li and Chudnovsky [17, 18] performed energy analysis and examined effects of an elastic inclusion on the energy release rate for crack extension. They studied variations due to inclusion translation, rotation and expansion with respect to the crack tip and showed that a crack approaching a soft inclusion accelerated while a crack approaching a stiff inclusion slowed down.

Boundary element (BE) methods have been used widely to address crack-inclusion interaction problems. Bush [19] used BE formulation to model a matrix crack interacting with single and multiple inclusions and reported crack paths and energy

release rates (ERR) for crack initiation and growth. This study showed that a crack tip approaching a particle is shielded from far field stresses whereas after it passes the inclusion the crack tip stresses are amplified. It was also observed that no substantial crack deflection occurs until the tip is within approximately one radius away although ERR effects are noticeable when the distance between the crack and the stiff inclusion is about five radii. He also modeled a weak interface between an inclusion and matrix by introducing a flaw between them and showed that the flaw increases ERR substantially and attracts the crack. Knight *et. al.* [20] studied the effect of introducing an interphase region between an inclusion and the matrix on ERR and crack trajectories using BE technique. They studied effects of Poisson's ratio of the inclusion and the matrix in the absence of interphase and observed that as the Poisson's ratio of the matrix approaches incompressibility limit of 0.5, shielding effect and deflection experienced by the crack reduces. They showed that the Poisson's ratio of the inclusion being higher than that of the matrix results in distinct shielding whereas amplification occurs in the opposite scenario. Interphase thickness was shown to affect the crack behavior depending on the relative elastic property mismatch between the three phases. Recently, Kitey *et. al.* [21] and Kitey [22] investigated interaction between a crack and a single inclusion and a cluster-of-inclusions using symmetric Galerkin BE method. They showed that a crack propagating through a particle cluster exhibits different trajectories with respect to cluster orientation whereas the overall energy dissipation remains unaltered. In this study it was also observed that increase in the area ratio of inclusions to matrix increases ERR and hence material becomes more fracture resistant.

Although many researchers have contributed analytically and numerically to the problem, strikingly few experimental investigations are found in the literature owing to the obvious experimental complexities. O'Toole and Santare [23] have investigated crack-inclusion interaction experimentally using photoelasticity. They simulated an inclusion by bonding rather than embedding two identical steel inclusions on two opposite faces of a polycarbonate plate ahead of a crack. Influence of elliptical inclusions on an edge crack was studied by calculating stress intensity factors from experimental data and showed toughening effect to be the greatest for an elliptical inclusion when its major axis is normal to the crack plane. Another interesting experimental study of the problem is by Li *et. al.* [24]. They experimentally modeled perfectly bonded 'second phase' in a matrix by altering the chemical structure by selectively exposing specific regions of a polymer to UV radiation. Under fatigue loading conditions, they experimentally measured crack speed and qualitatively observed fractured surface morphology. They reported energy release rates and crack speeds for a crack approaching and penetrating softer inclusion and showed that interaction with a soft or a stiff inclusion affects the resulting crack path significantly. Single fiber pull-out test is used to characterize interfacial properties of fiber-matrix bond, namely interfacial fracture energy (in shear dominated failure) and shear stress. Easley *et. al.* [25] used moiré interferometry to investigate stress field in a fiber pull-out test in the presence of nearby matrix cracks when the crack plane is perpendicular to the axis of the fiber. Specimens with partially exposed fibers were used to investigate shear stress in the vicinity of the fiber and the crack. They reported a decrease in shear stress near the fiber-matrix interface at peak pullout load.

A perfect bond between a matrix and an inclusion seldom exists in reality due to finite interfacial strength. This results in interfacial debonding between the two which in turn plays a significant role in the overall failure process. The presence of a nearby crack would likely aggravate or accelerate the process as well. Apart from the interfacial bond strength, debonding may depend on material properties of the matrix and the inclusion, geometry of the crack-inclusion pair and the type of loading. The matrix-inclusion debonding causes redistribution of strains and hence stresses in the vicinity of both the inclusion and the crack. These make it important to study and model mechanical fields in the vicinity of a crack-inclusion pair as debonding evolves. Debonding of the inclusion matrix can be easily detected if full-field displacements are measured. None of the reported investigations address this very important issue of matrix-inclusion debonding in presence of a nearby crack. Dearth of experimental investigations regarding this issue emphasizes the need for further investigation in this regard. Also, experimental investigation of this problem can offer valuable insight for developing numerical models and help achieve reliable solutions.

1.4 Objectives

As discussed in the previous Section, the issue of debonding of a matrix from an inclusion in the presence of a crack requires further experimental investigation. Optical techniques are extensively used for mapping full-field deformations in various solid mechanics problems. Among these techniques moiré interferometry is a well-known whole field experimental tool used to study in-plane displacement and strain fields. This technique in its various forms has been employed to study macro and micro mechanics

problems by many researchers. To be able to employ this technique successfully, fabrication of physical specimen gratings of desired spatial frequency in the region of interest is of key importance. Microlithography processes are extensively adopted in recent years by microelectronics and MEMS industries to fabricate micro and nano features on different substrates. The most common substrate used is silicon which is commercially available in the form of wafers. Microfabrication of gratings on a silicon wafer is a well-known process that uses photolithography and can be used to fabricate gratings on specimen substrates. Considering all the requirements of the stated problem and the availability of resources, the main objectives identified for this research are as follows:

- Fabricate square-wave profile gratings on silicon wafer and devise reliable method/methods to transfer gratings to specimens.
- Fabricate a specimen to study the crack-inclusion interaction problem in a two-dimensional setting.
- Develop a moiré interferometer to map full-field displacement fields in real-time and extract strains at strategic locations in the vicinity of a crack-inclusion pair.
- Measure fracture parameters such as crack opening displacements and stress intensity factors (K), energy release rates (ERR) under quasi-static loading conditions and identify matrix-inclusion debonding.
- Model matrix-inclusion debonding in the crack tip vicinity using finite element method and experimentally validate the model.

- Parametrically study crack-inclusion interaction using the validated finite element model.

1.5 Organization of the thesis

Including the current chapter this thesis comprises of five chapters. Chapter 2 presents details of the microfabrication used to develop silicon wafer gratings. In this chapter the methods developed to fabricate the specimen gratings are elaborated. This chapter also describes fabrication of crack-inclusion specimen for experimental study. Chapter 3 discusses the basics of interference of light waves and the working principle of moiré interferometry. Results of benchmark experiment with homogeneous cracked sample (without inclusion) are presented in this chapter. The experimental investigation of the crack-inclusion interaction problem using moiré interferometry is described in Chapter 4. Chapter 5 describes a finite element methodology to simulate crack-inclusion interaction including the method used to model debonding between an inclusion and a matrix. This chapter also covers comparison between experimental and numerical results followed by a parametric study for the crack-inclusion problem using the adopted methodology. Chapter 6 concludes the work with a summary of observations and outcome of the thesis work.

CHAPTER 2

GRATINGS FABRICATION AND TRANSFER TECHNIQUES

A critical requirement for successfully implementing moiré interferometry is to have high quality gratings printed on the specimen. Modern day lithography processes have been used in the current work to fabricate amplitude gratings on silicon wafers. Two methods are developed to transfer gratings to specimens. Photolithography is the underlying methodology used here to achieve the desired patterns [26]. It involves transfer of geometric shapes on a mask to a substrate coated with photosensitive polymer called photoresist. Accounts of various other methods used to develop and print gratings on specimens for moiré interferometry can be found in works by Post [27] and his co-researchers. Among these, a method extensively used now-a-days involves fabrication of a master (sinusoidal) grating using high spatial frequency interference pattern of photoresist. The photoresist is developed following exposure to create a master grating. Replicas made from master gratings are used to create specimen gratings after depositing a reflective aluminum layer on them. In the current work photolithography technique is used in conjunction with various microelectronic fabrication tools and methods to create ‘square-wave’ amplitude gratings on a silicon wafer. This process is executed in various steps and requires a careful control over the process parameters to achieve the desired results. Next the various necessary steps are described.

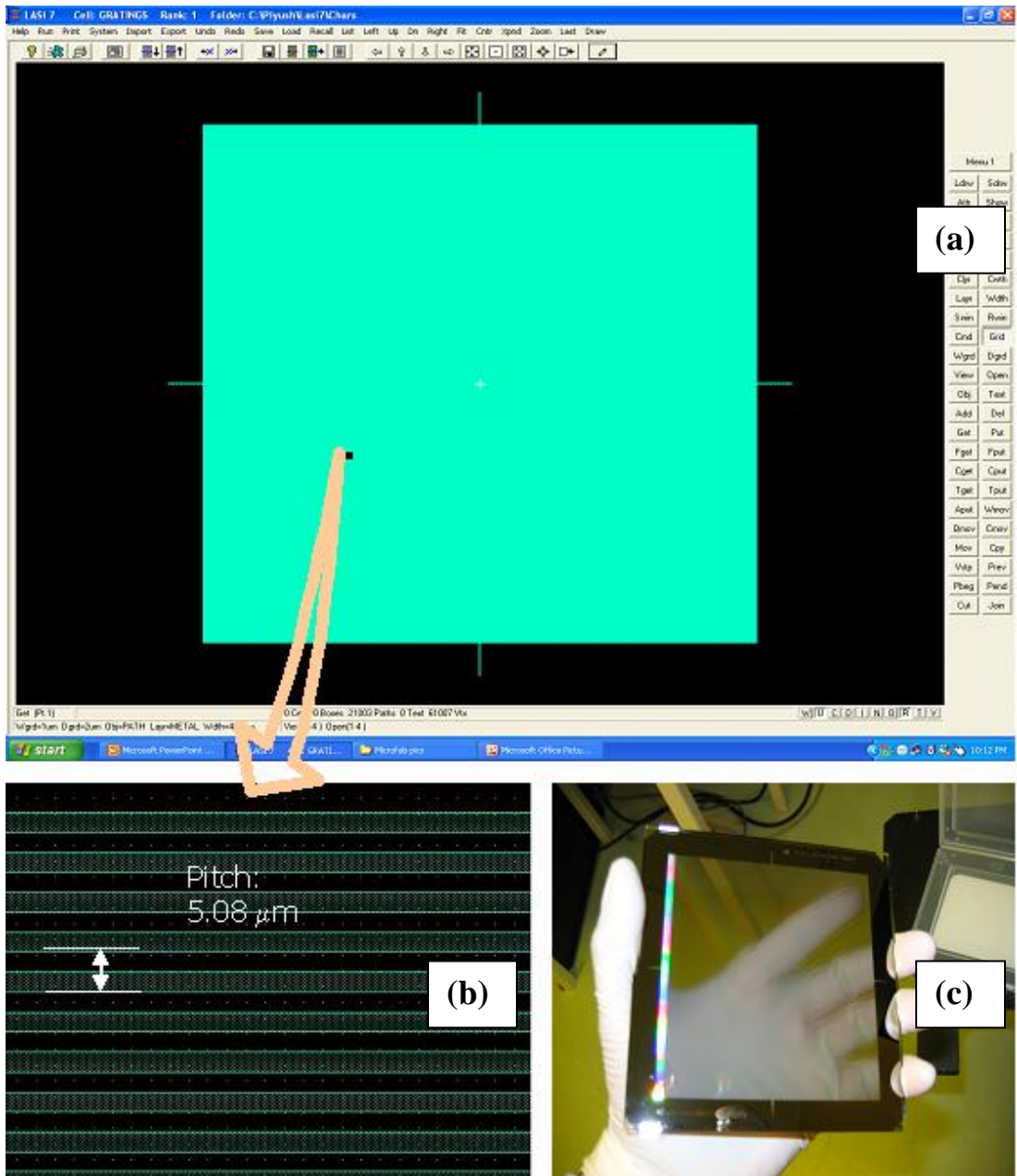


Figure 2.1: (a) LASI window showing mask design. (b) Enlarged view of the gratings design in LASI. (c) Mask (Ronchi gratings) made according to the design.

2.1 Master gratings fabrication

Considering the availability of in-house microfabrication facilities, a spatial frequency of 5000 lines/inch (5.08 μm pitch) was adopted. A mask was first designed using LASI (LAYout System for Individuals), a general purpose IC layout freeware and design system. A chrome-on-glass mask (essentially a Ronchi grating) with equally spaced opaque chrome bars and transparent glass spaces was procured from a commercial source based on the supplied design. Figure 2.1(a) shows the LASI design window used for the mask design. In Fig. 2.1(b) an enlarged view of the grating pattern to be produced on the mask is shown. Figure 2.1(c) shows the actual mask thus procured. The active area of the mask has dimensions of 4 inch x 4 inch and it can be used to process a 4 inch diameter silicon wafer utilizing the full wafer area.

A single side polished, P-type <100> silicon wafer (diameter = 100 mm, thickness = 1 mm) was used for producing master gratings. (The crystallographic orientation and



Figure 2.2: (a) Wafer cleaning. (b) Dehydration bake.

doping are not critical for the present work and were simply based on the availability.) The polished surface of the wafer was used for all processes described in the following. The wafer surface was rinsed with Acetone (Dimethyl Ketone $\text{CH}_3\text{-CO-CH}_3$) generously followed by a quick rinse with Methanol (Methyl alcohol $\text{CH}_3\text{-OH}$) and then dried using pressurized nitrogen (see Fig. 2.2(a)). Next the wafer was baked at $120\text{ }^\circ\text{C}$ for 20 min, to remove any moisture (Fig. 2.2(b)). Then HMDS (Hexamethyl-Disilazane) - a primer that enhances adhesion between silicon and photoresist - was vaporized onto the wafer surface in a closed container for about 20 minutes (Fig. 2.3(a)). After centering the wafer on a vacuum chuck a positive photosensitive polymer (photoresist-AZ5214) was spin coated on the prepared wafer surface at 3500 RPM for 30 seconds as shown in Fig 2.3(b). This results in a ($\sim 1.5\text{ }\mu\text{m}$ thick) layer of photoresist over the wafer surface. To let the photoresist cure quickly the wafer was then soft baked on a hot plate at $105\text{ }^\circ\text{C}$ for 60 seconds with the rough side of the wafer in contact with the hot plate surface (Fig. 2.4(a)).

Next the photoresist was exposed using the mask in a mask aligner (Karl Suss Model # MA6) with an exposure time of 6-8 seconds. UV radiation is used in the mask aligner (Fig. 2.4(b)) for exposing the photoresist. A hard contact was used between the mask and the wafer during exposure.

The exposed wafer was then developed (Fig. 2.5(a)) in a 1:2 solution of developer AZ 400K and water for approximately 20 seconds. Then the wafer was quickly rinsed deionized water (Fig. 2.5(b)) for 2 minutes, dried using pressurized nitrogen (Fig. 2.5(c)) and inspected under an optical microscope (Fig. 2.5(d)). The development of the photoresist results in a regularly spaced photoresist bars with bare silicon spaces in

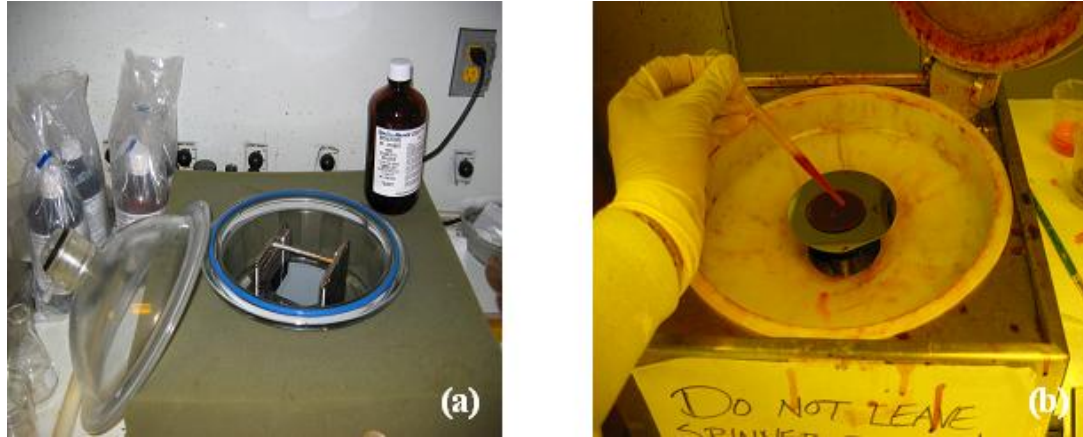


Figure 2.3: (a) HMDS application. (b) Photoresist application.

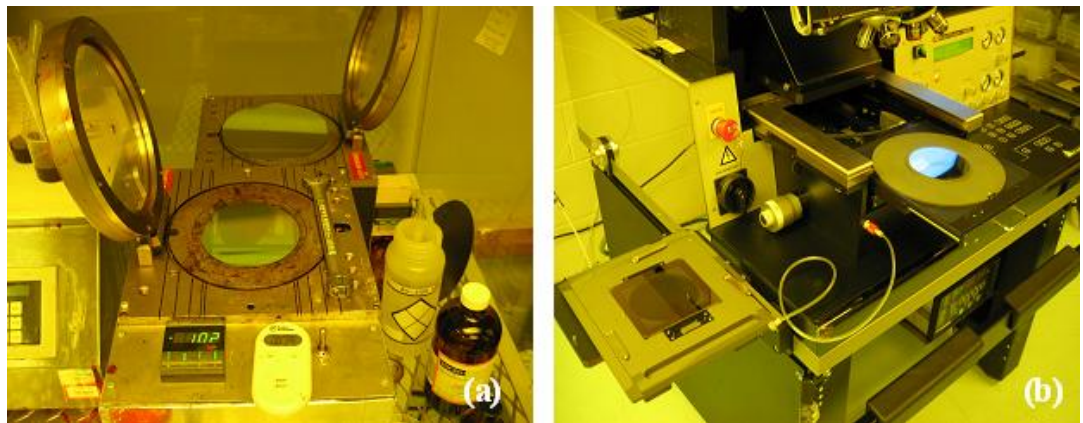


Figure 2.4: (a) Soft baking of the wafer. (b) The mask aligner showing the mask and the wafer. (Mask is held in the frame by vacuum.)

between them. The developed wafer was then anisotropically etched in those bare silicon spaces using Inductively Coupled Plasma (ICP) (STS Multiplex ICP). An in-built program 'MORGANSOI' was used for this purpose for 4 cycles of alternative passivation and etching. Each consecutive etching cycle affects the passivation layer on horizontal surfaces but the vertical walls are almost unaffected during etching. This results in a very

high quality anisotropic etching with almost square wave profile gratings on silicon wafer. Approximately $2\ \mu\text{m}$ etching depth was achieved. The photoresist bars were then stripped off from the wafer using oxygen plasma using a photo-stripping machine (MATRIX). An in-built program 'Photo-Str' was used and the process time used was approximately 4 minutes. At the end of this step a high quality square-wave grating

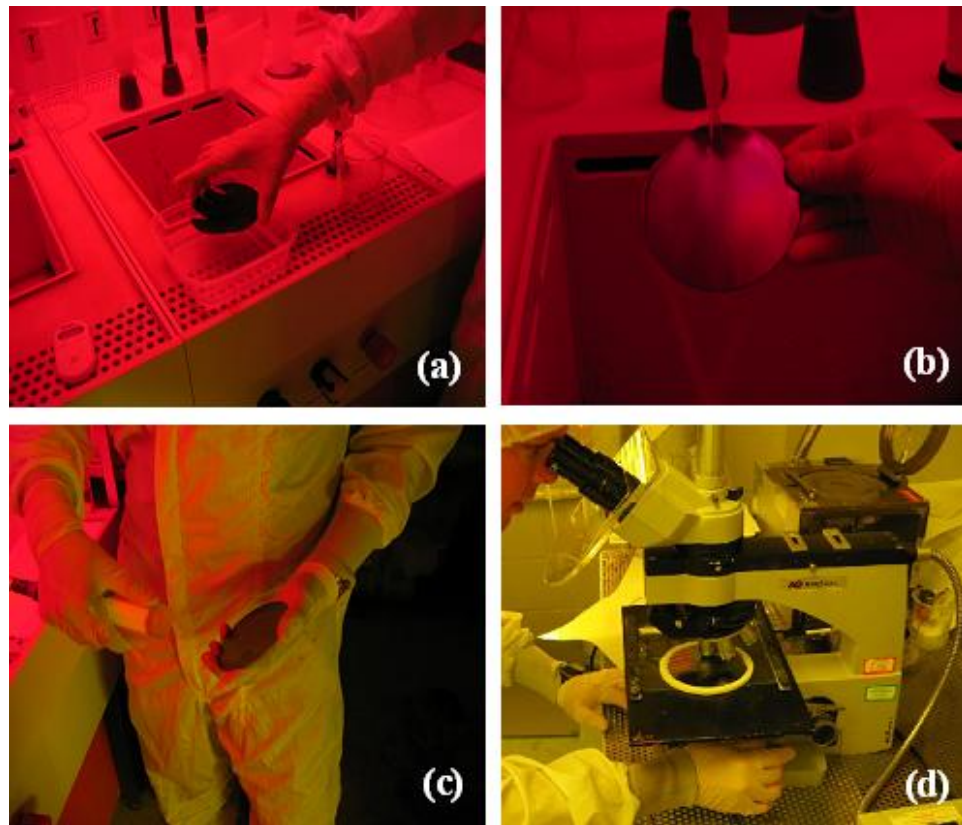


Figure 2.5: (a) Photoresist development (b) Rinsing (c) Drying (d) Inspection under microscope.

was generated on the wafer surface with the desired pitch of $5.08\ \mu\text{m}$. Then using the same ICP machine a very thin passivation layer (C_4F_8) was deposited on the gratings using a program 'PASSIVAT' for 6 minutes. The silicon wafer gratings were then examined under a microscope and critical dimensions were measured using an in-built



Figure 2.6: STS Multiplex ICP used to etch silicon.

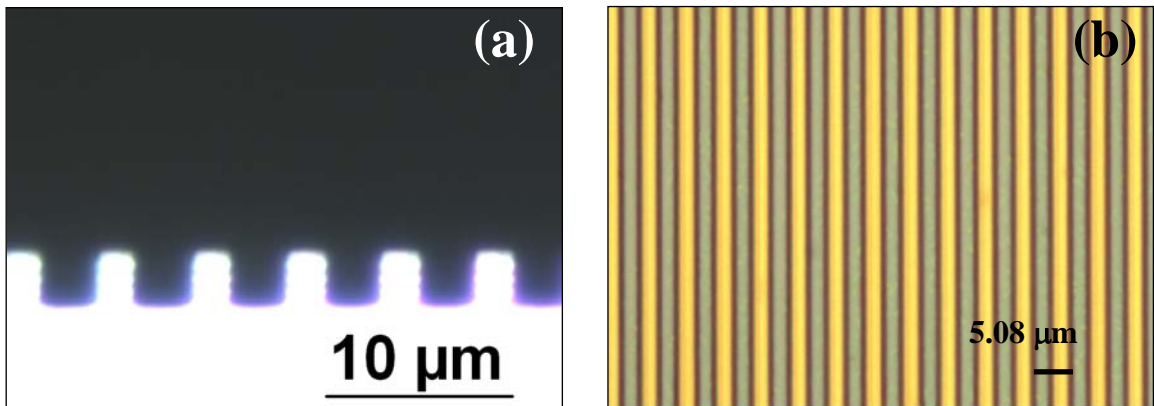


Figure 2.7: Micrographs of silicon wafer gratings (a) Cross section. (b) Front view.

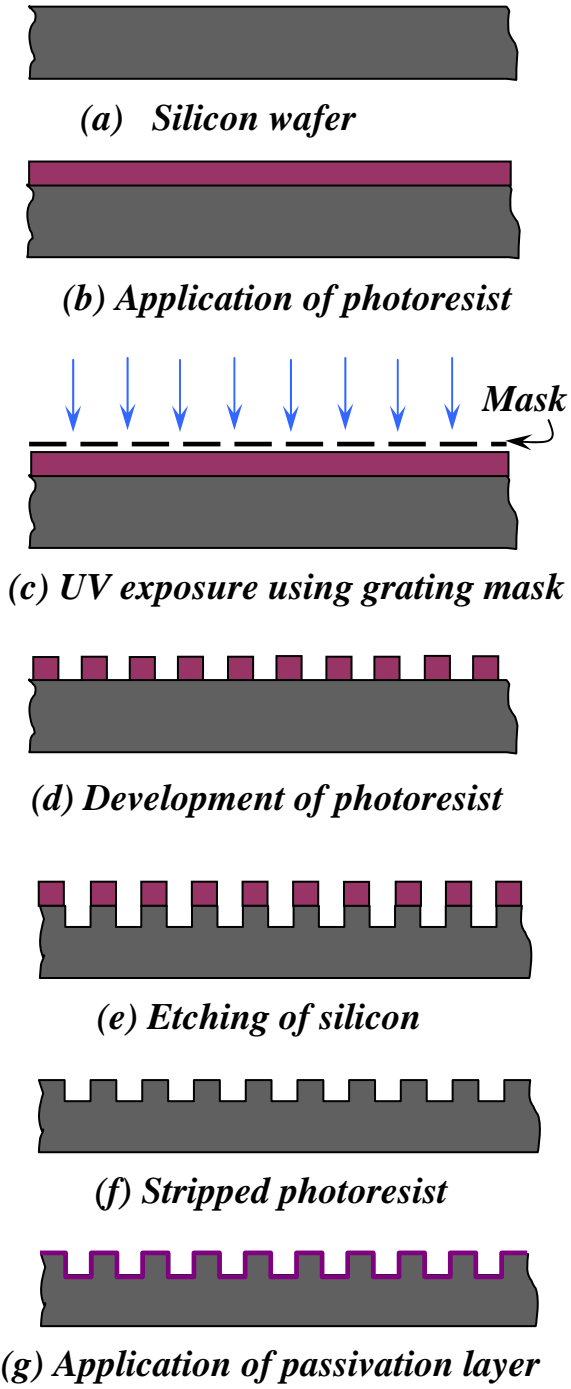


Figure 2.8: Schematic of steps involved in fabrication of silicon wafer gratings.

digital camera. The micrographs of silicon wafer gratings are shown in Fig. 2.7. Figure 2.8 shows a schematic of all the processes discussed so far.

2.2 Grating transfer methods

To prepare specimen gratings from master gratings two different techniques were developed in this work. Both the techniques were tested successfully and are described in detail next.

2.2.1 Direct grating transfer from a silicon master

In this method a thin aluminum layer was vacuum deposited on the silicon wafer after the gratings were prepared as described earlier. This was done using a Denton Vacuum Deposition machine under high vacuum of (2×10^{-5} torr). A photograph of a silicon wafer grating with aluminum film deposited over it is shown in Fig. 2.9. The rest of the steps involved in grating transfer are depicted schematically in Fig. 2.10.

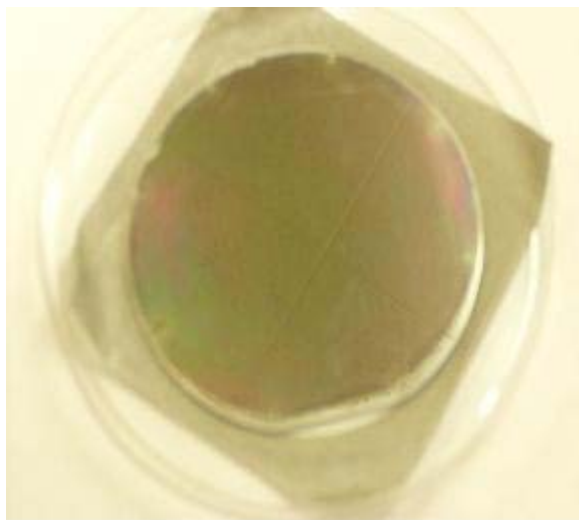
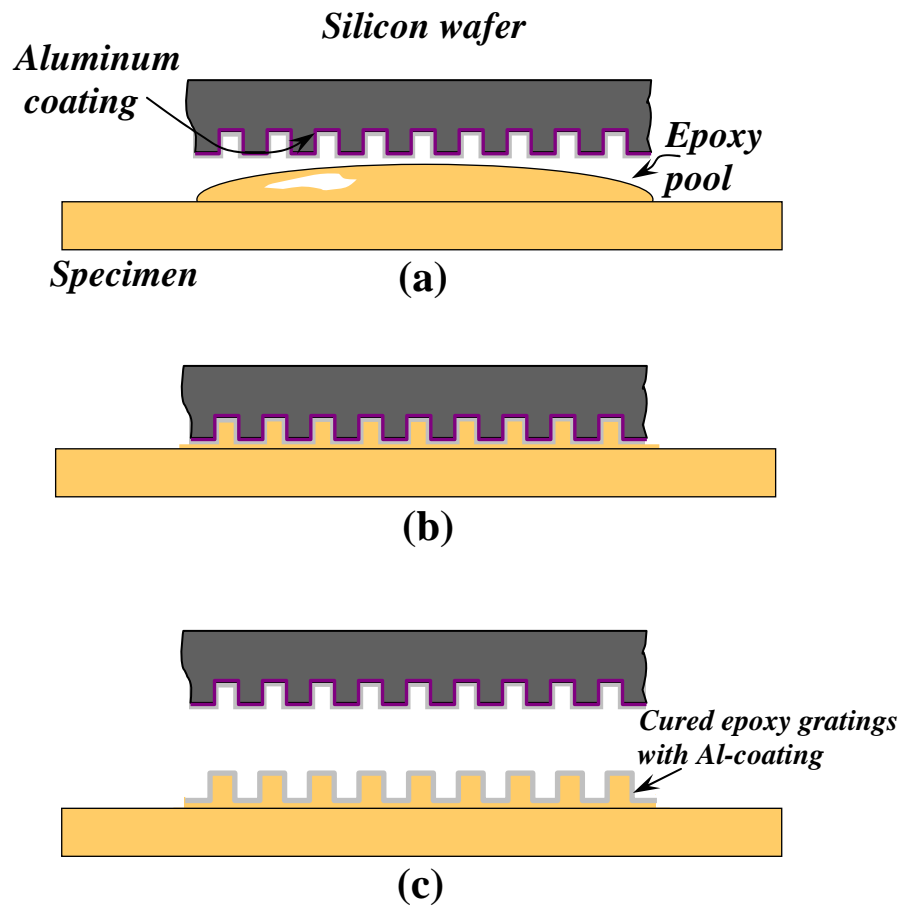


Figure 2.9: Aluminum coated silicon wafer gratings.



(d)

Figure 2.10: Direct transfer of gratings from silicon wafer with aluminum coating. (Note: In the schematic the specimen and the wafer are shown in thickness dimensions.)

The fluorocarbon passivation layer (C_4F_8) (see, section 2.1) acts as a parting layer between aluminum and silicon by reducing the adhesion strength between the two. The specimen surfaces on which gratings were being transferred were prepared using #220 and then #320 grit sand papers. A pool of liquid epoxy was applied to the specimen surface in the region of interest as shown in Fig. 2.10(a). The silicon master with the desired orientation of the gratings with respect to the specimen was pressed against the epoxy pool. Excess epoxy was removed and the pair was allowed to cure at room temperature for about 72 hours. After the epoxy was cured silicon wafer was carefully pried off without much effort. This resulted in gratings along with aluminum coating transferred to the specimen surface with a high degree of fidelity (Fig. 2.10(c)) and good reflectivity. (The use of thick (1 mm) wafer was helpful in handling of the wafer when being pried off the specimen surface.) The silicon wafer was re-used to print gratings on other specimens after redepositing the passivation layer and aluminum over it. A specimen prepared in this manner is shown in Fig. 2.10(d) with high quality grating structure in the region of interest.

2.2.2 Grating transfer using silicone rubber submasters

In the second method, silicone rubber was used to make submasters or replicas of the master grating pattern on silicon wafer. A cardboard mold with its sides parallel and perpendicular to the grating lines was prepared to create a stamp to replicate the gratings from silicon wafer to the specimen. A photograph of the mold on silicon wafer and prepared silicone rubber stamp (or submaster) with gratings on them is shown in Fig. 2.11. The steps involved in transferring gratings from the silicon wafer to a specimen is

shown schematically in Fig. 2.12. After preparing a card-board mold, 2 part silicone rubber* was mixed thoroughly and liquid rubber was deaerated in a vacuum chamber at ~ 25 inches of mercury until the rubber pool rises initially and trapped air bubbles collapse eventually. Deaeration was continued for an additional 3-4 minutes. The liquid rubber was then transferred into the mold and cured at room temperature for over 16 hours (Fig. 2.12(a)). The cured rubber submaster was then detached from the silicon wafer with ease. A glob of liquid epoxy† was then deposited on a pre-fabricated epoxy specimen surface (prepared with #220 and #320 grit sand papers) in the region of interest (Fig.

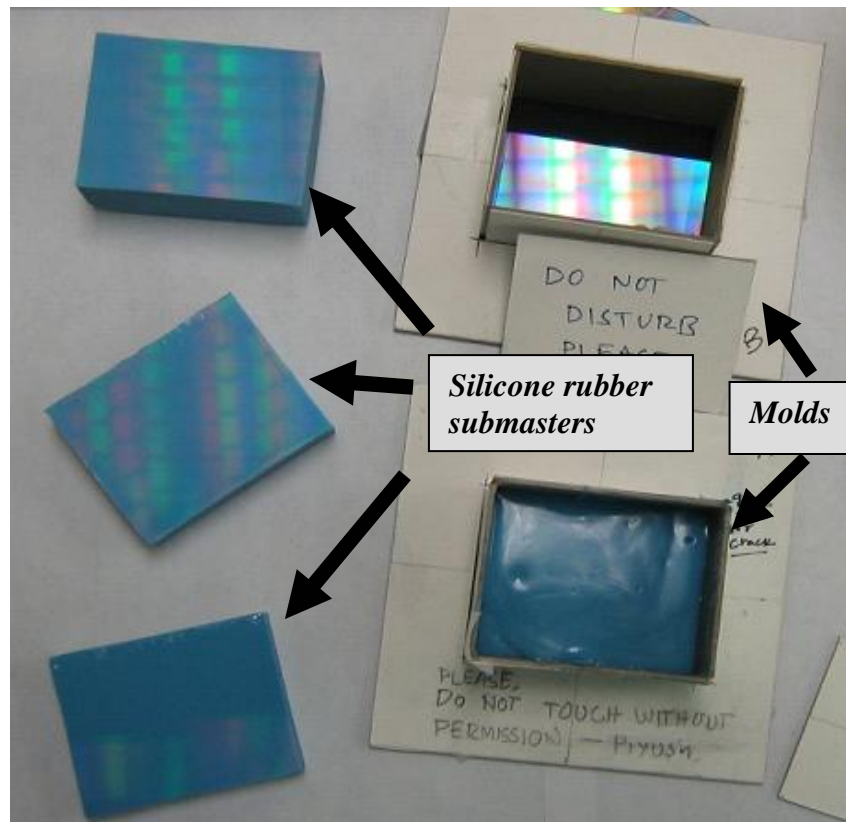


Figure 2.11: Silicone rubber casting molds and submasters.

*Two-part silicone rubber (Plastisil 73-60 RTV) manufactured by Polytek Inc., PA.

†Two-part epoxy (Epo-Thin™ (Product # 20-1840, 1842,)) 100 parts resin : 39 parts hardener) from Beuhler Inc., PA.

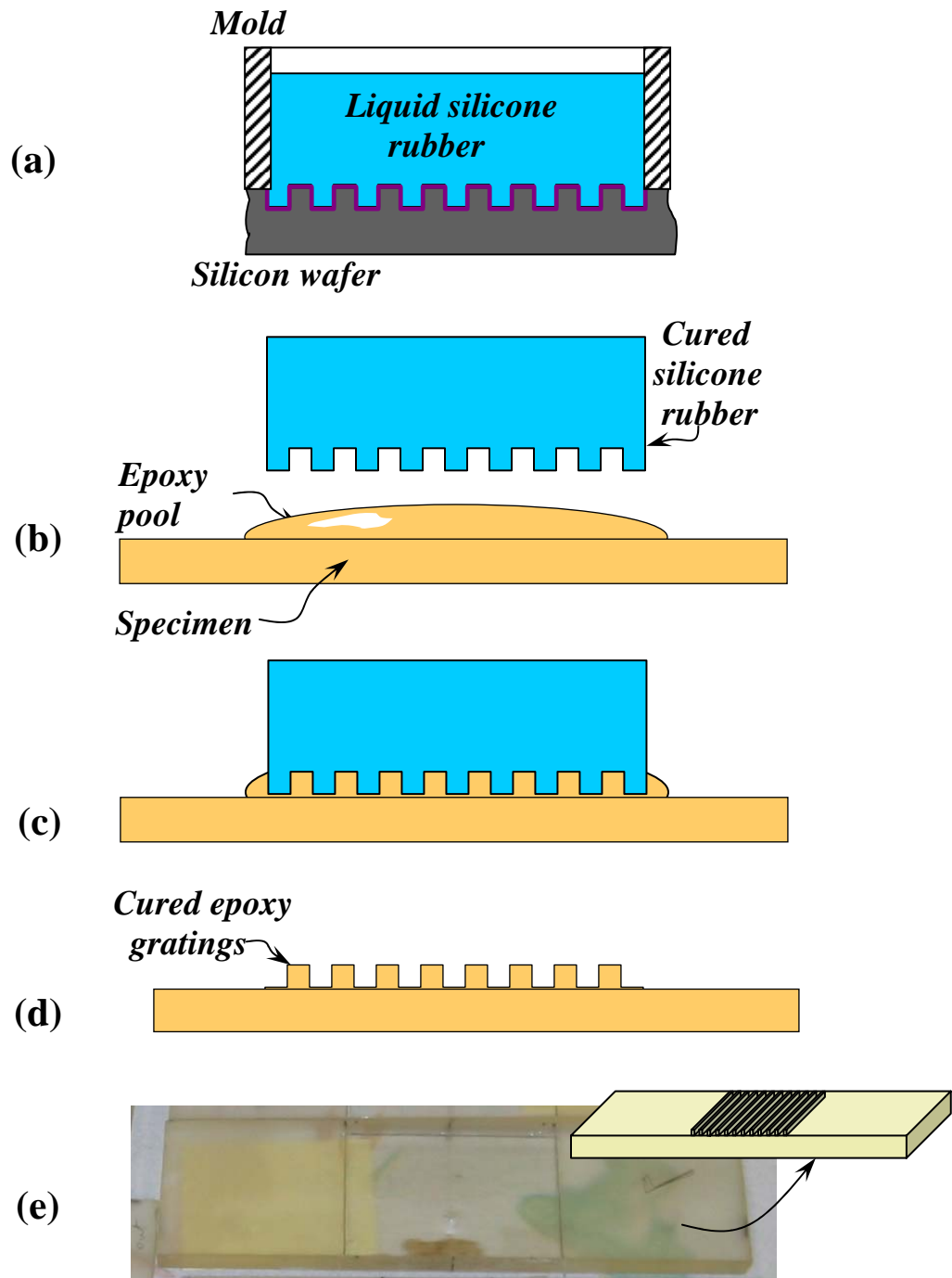


Figure 2.12: Steps involved in fabrication of silicone rubber submaster grating and transferring grating pattern onto specimen surface. (Note: specimen and grating are shown in the thickness dimension)

2.12(b)). The silicone rubber submaster, with its edges aligned with the machined specimen edges, was pressed against the specimen surface and excess epoxy was squeezed out (Fig 2.12(c)) and removed using cotton swabs. Finally after epoxy was cured the rubber mold was detached from the specimen with little effort (Fig 2.12(d)). This resulted in high quality amplitude gratings on the specimen surface.

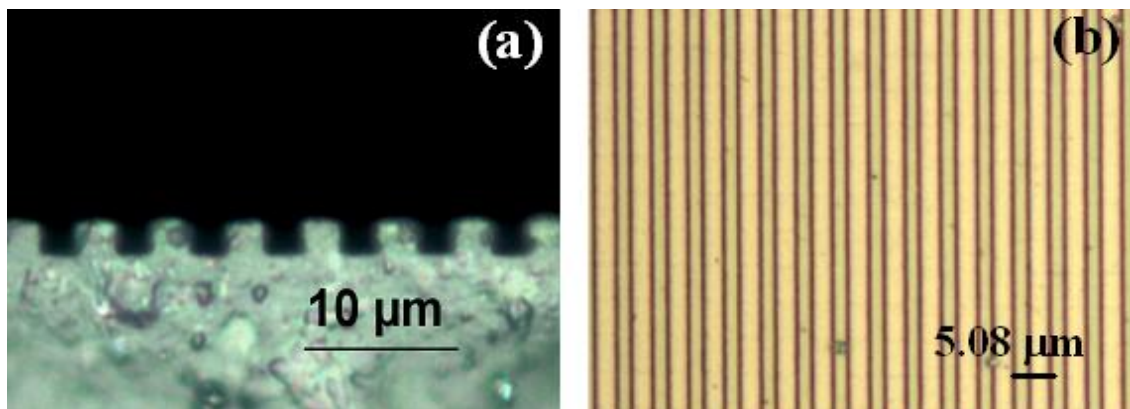


Figure 2.13: Micrographs of (a) Cross-section of a silicone rubber submaster (b) Front view of epoxy gratings transferred using a silicone rubber submaster.

Relatively high diffraction efficiency was obtained from these gratings as evident from high quality moiré interferograms to be discussed. (Depositing a reflective metallic film (aluminum, gold, etc.) is optional for studying dynamic events where high reflectivity is needed.) This method allowed fabrication of virtually unlimited numbers of submasters and was also tested successfully on both metallic and polymeric substrates. A specimen with epoxy gratings transferred using this method is shown in Fig. 2.12(e). The cross-section of a silicone rubber stamp as viewed under an optical microscope is shown in Fig. 2.13(b).

2.3 Crack-inclusion specimen fabrication

Next, specimen preparation for crack-inclusion interaction studies is described. To simulate this problem in a two dimensional setting, epoxy was used as the matrix material and laboratory grade glass was used as the inclusion. The elastic properties of the matrix and the inclusion phases are listed in Table – 2.1. Pyrex glass rods of diameter 3.8 mm

	Young's modulus E (GPa)	Poisson's ratio ν
Epoxy	3.5	0.35
Glass	68	0.19

Table 2.1: Elastic properties of matrix and inclusion.

were cut into cylindrical pieces of length 7.1 mm. To enhance bond strength between glass and epoxy, glass cylinders were treated with gamma-aminopropyltrimethoxysilane[‡] according to manufacturer's instructions. This bonding agent is used widely in the fabrication of glass-filled polymeric composites to improve matrix-filler bonding strength. The glass cylinder was then held in a mold of cavity thickness equal to its length so that the axis of the cylinder was perpendicular to the major dimensions of the mold (see, Fig. 2.14(a)). Two part epoxy mixture was then poured into the mold around the inclusion and cured at room temperature for about 72 hours. The cured sample was then machined to the required dimensions and epoxy gratings were printed using one of the methods described previously. (It should be noted that, gratings and specimen materials being same, shear lag effects are minimum.) Figure 2.14(b) depicts specimen geometry, dimensions and loading configuration with an illustration of grating lines and orientation on them. Here L is the distance between the crack tip and the center of the

[‡] Silquest A-1110 Silane manufactured by GE Silicones, WV.

inclusion of diameter d . Thus L/d ratio is a nondimensional measure of inclusion proximity to the crack tip and it was 1.31 in this work. A notch was then cut into the edge of the specimen using a circular diamond impregnated saw blade (thickness

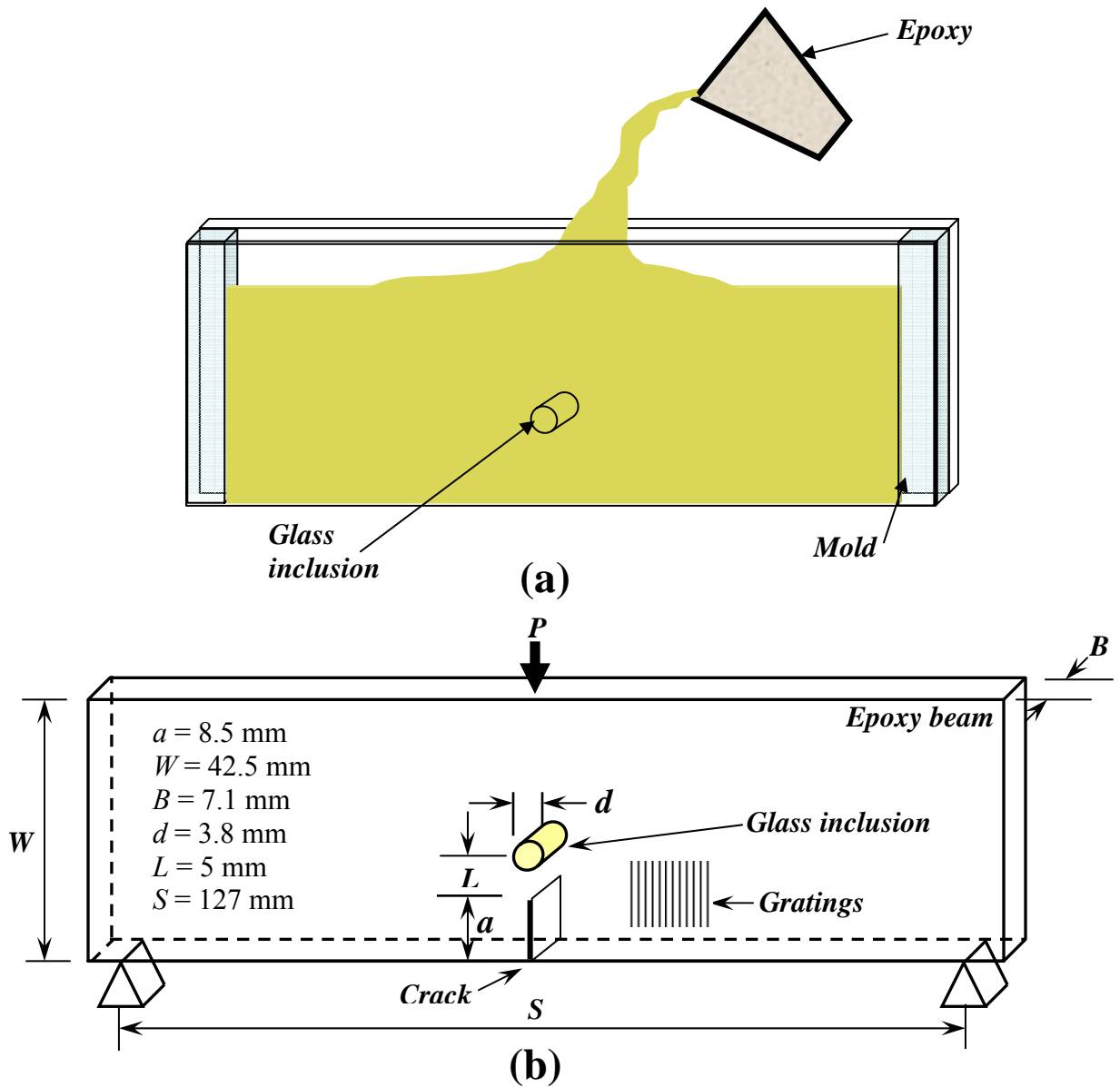


Figure 2.14: (a) Specimen preparation, (b) Specimen geometry and loading configuration.

~300 μm). To sharpen the notch-tip a set-up was developed and is shown in Fig. 2.15(a). The set-up includes a translation stage with micrometers mounted on an angle bracket with a sharp razor blade fixed vertically, as shown. The specimen was rested on a fixed stage with horizontal and vertical support surfaces. The thickness of the blade being less than the notch width, it was driven freely into the notch. The sharp edge of the blade was then pressed into the notch tip in a controlled manner for approximately 200 μm depth. The blade was then retracted while holding the specimen against the supports resulting in a sharpened notch tip shown in the micrographs in Figs. 2.15(b) and (c). By careful alignment of the blade with respect to the translation stage the length difference of the sharp crack on the front and back sides at the notch tip was controlled to within ± 30 μm .

2.4 Materials characteristics

Epoxy used in this work as the matrix material was initially characterized by performing a uniaxial tension test on a ‘dog-bone’ specimen. The test was performed in a INSTRON 4465 testing machine and the results are shown in Fig. 2.16. The strain was measured using an extensometer (Epsilon Inc., model # 3542-0050-010-ST). The initial response shows that epoxy used here is essentially a linear elastic material with a modest nonlinearity seen before failure. The elastic modulus determined from the graph by drawing a tangent to the initial part of the curve is 3.4 ± 0.1 GPa. Evidently, the strength of epoxy is approximately 63 ± 2 MPa and failure strain is 0.02 ± 0.002 .

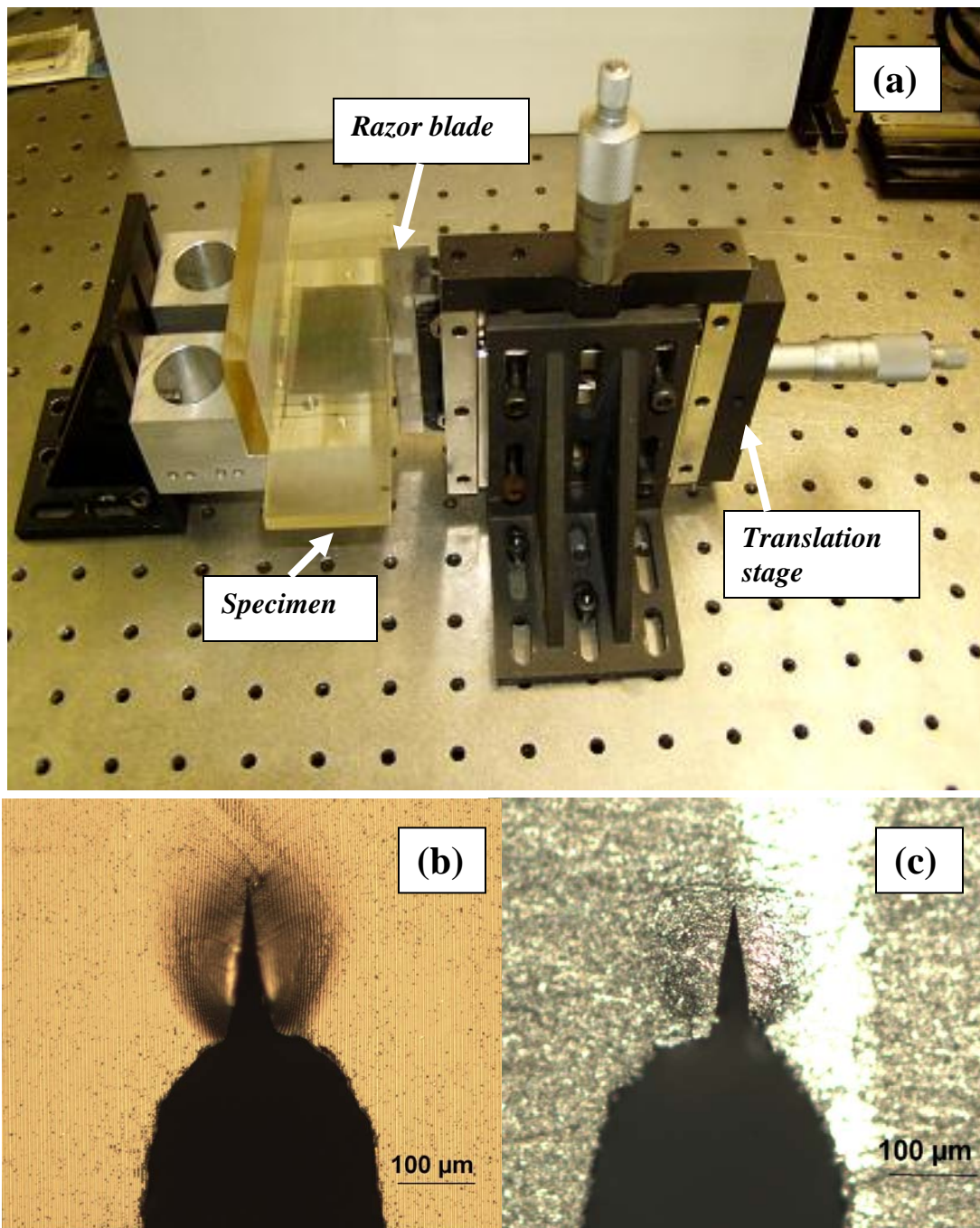


Figure 2.15: (a) Notch-sharpening setup. (b) Sharp-crack: front-side view of the specimen. (c) Sharp-crack: back-side view of the specimen.

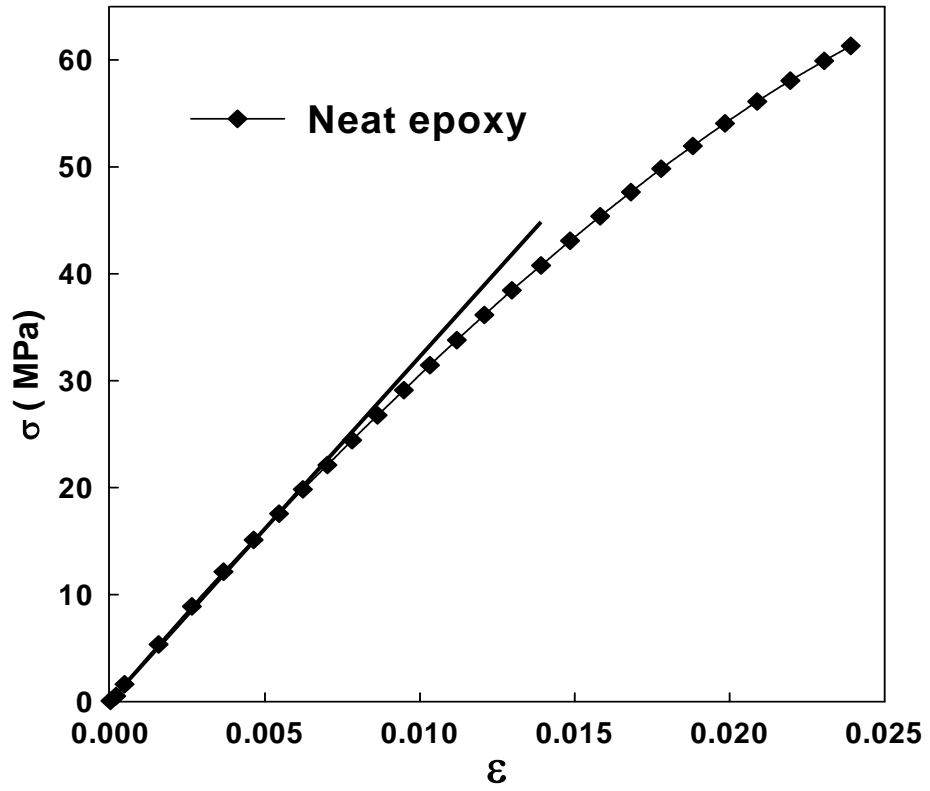


Figure 2.16: Stress-strain response of neat epoxy.

CHAPTER 3

MOIRÉ INTERFEROMETRY

Moiré fringes are interference patterns generated when two geometric patterns of nearly same spatial frequency are superimposed. Though considered optical noise in many instances moiré patterns are used in the field of solid mechanics to measure in-plane and out-of-plane deformations. An interferometric version of this method called moiré interferometry is used in the current research to map in-plane displacement components in real-time. This method has been used successfully to study macro- and micro-mechanics problems in engineering. These encompass fracture mechanics, mechanics of microelectronic packages, composite materials, bi-material joints and for calibrating strain measuring devices, to name a few.

In the current work moiré interferometry is utilized to map evolution of dominant displacement fields in the vicinity of a crack-inclusion pair. Moiré interferometry depends on both interference and diffraction of coherent light. Two coherent light beams with plane wave fronts interfere to produce periodic constructive and destructive intensity patterns or the so-called virtual gratings. The working principle, implementation issues and various applications of moiré interferometry are detailed in a monograph by Post [27, 28]. This chapter explains the optical setup developed for the current investigation, the

associated mathematical analysis of moiré interferometry [29, 30], validation experiments and results.

3.1 Experimental Setup

Figure 3.1 shows a schematic of the optical setup developed during this research. It includes a 8 mW He-Ne laser, Ronchi grating (R), mirrors (M1, M2, M3 and M4), collimators (C1 and C2), lens (L1) and a CCD camera. The Ronchi grating R is of the same pitch as the specimen gratings to easily achieve the required angles of incidence on the specimen. The unexpanded laser beam was made to pass through the Ronchi gratings (with its principal axis in the horizontal plane, in this case) using mirror M1. Upon transmission laser beam undergoes diffraction and several odd diffraction orders in the horizontal plane are generated. The angle α between diffraction orders is given by the diffraction equation,

$$\sin \alpha \approx \frac{\lambda}{p} , \quad (3.1)$$

where λ is the wave length of light and p is the pitch of the Ronchi gratings. For He-Ne laser ($\lambda = 633$ nm) and a grating pitch of $5.08 \mu\text{m}$, the value of α is $\sim 7.15^\circ$. All but ± 1 diffraction orders were blocked by an aperture and the first order diffractions were directed towards mirrors M2 and M3. The reflected laser beams were then directed into two separate beam expanders coupled to collimators C1 and C2 as shown. The collimators were mounted on x - y - z translation stages for fine adjustment. The expanded and collimated laser beams (with plane wave fronts) were directed towards the specimen as shown and made to interfere with each other producing a standing wave of pitch

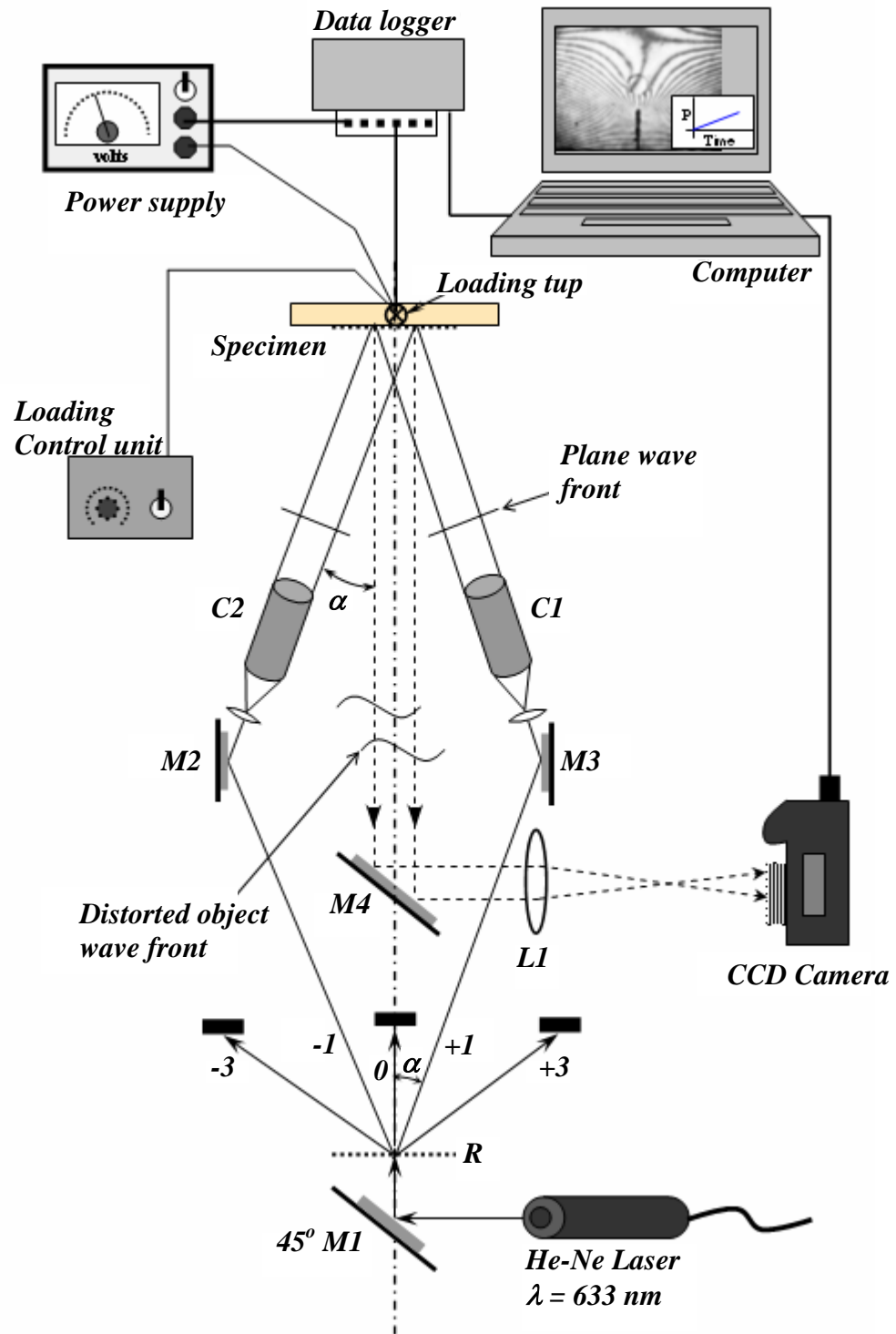


Figure 3.1: Schematic of moiré interferometer.

$p_v = 2.54 \mu\text{m}$ (10000 cycles/inch) on the specimen surface. These two incident beams are diffracted by the specimen grating and produce ± 1 diffractions propagating along the optical axis (dotted line) towards mirror M4 and the camera carrying information about in-plane deformations shown by warped wave fronts in Fig. 3.1. They are directed into the camera back by the mirror M4 and imaging lens L1. The recording system consisting of the lens and the camera back is kept focused on the specimen plane. For further clarity a three dimensional sketch of the setup is shown in Fig 3.2 and an actual photograph of the setup is shown in Fig. 3.3.

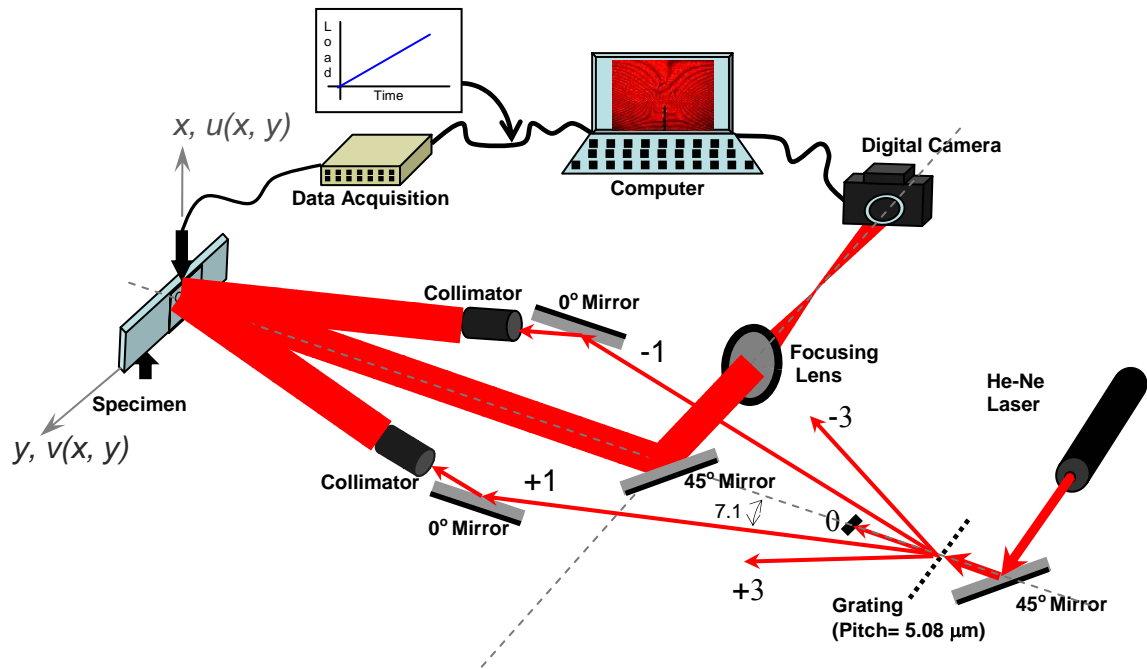


Figure 3.2: 3-D representation of the moiré interferometry setup.

A null field was achieved in no-load condition by making fine adjustments to the collimators. The +1 and -1 orders emerging from the specimen grating and propagating along the optical axis interfere and produce moiré fringes. The details of the optical

analysis are presented in the next section. These fringes represent contours of in-plane displacement component in the principal direction of the specimen grating. In the current

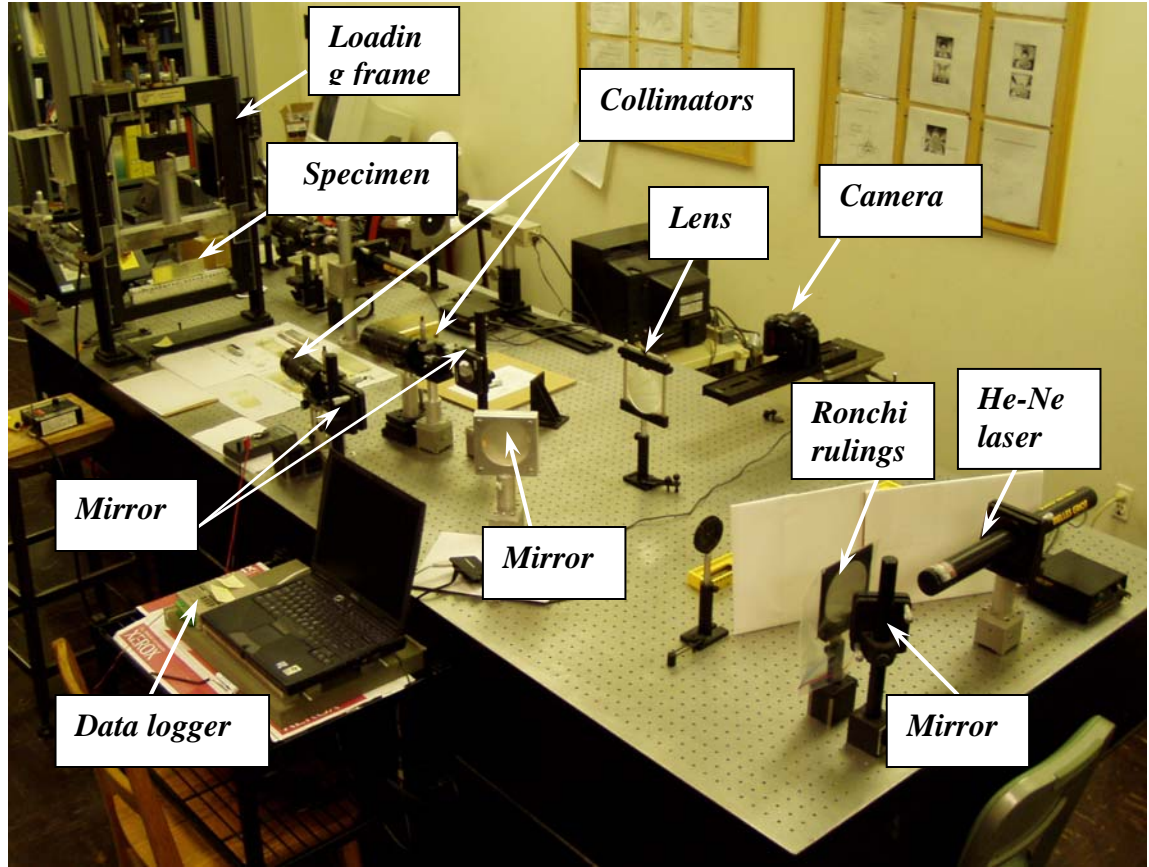


Figure 3.3: Photograph of moiré interferometry setup.

investigation crack opening displacements (displacements in the y -direction) were mapped. The opening displacements are governed by the equation,

$$v(x, y) = N_y(x, y)p_v, \quad N_y = 0, \pm 1, \pm 2, \pm 3, \dots \quad (3.2)$$

where N_y represents fringe orders and $p_v (= 2.54 \mu\text{m})$ is the pitch of the virtual gratings

3.2 Deformation field mapping

The specimen was placed in a loading frame and a null light field was achieved under no-load conditions. A digital CCD camera interfaced with a computer was set to time-lapse photography mode to record interferograms at 2 seconds intervals during the loading phase. A load cell connected to a data logger was also interfaced with the same computer and was configured to log the load history at a rate of 5 samples/sec during the event. Both the camera and the data logger were triggered from the computer at the same time as the loading phase was initiated. The specimen was loaded quasi-statically in three-point bending configuration in a displacement control mode with a cross-head speed of ~ 0.04 mm/sec. The recording camera was configured in a manner that each image was tagged with temporal information of the computer clock as images were dumped into the computer memory. The data logger clock was also synchronized with the computer clock such that loading data and the corresponding time for each data point was recorded. This facilitated establishing load levels at which each image was recorded.

3.3 Interference of plane waves

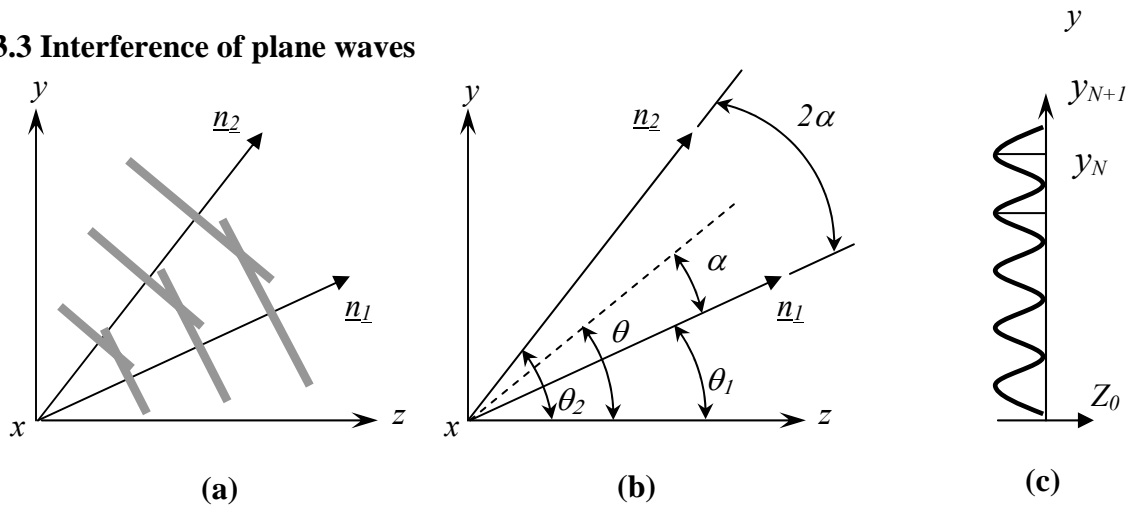


Figure 3.4: Interference of plane waves. (a) Plane wave propagation. (b) Geometry and (c) Intensity on the image plane.

Let us consider two plane waves with propagation vector represented by \underline{n}_1 and \underline{n}_2 shown in Fig 3.4 and their respective angles with the z -axis as θ_1 and θ_2 . These plane waves can be represented in vectorial forms as,

$$\left. \begin{aligned} \psi_1 &= A_1 e^{ik\underline{n}_1 \cdot \underline{s}} \\ \psi_2 &= A_2 e^{ik\underline{n}_2 \cdot \underline{s}} \end{aligned} \right\} \quad (3.3)$$

where ψ_1 and ψ_2 denote complex amplitude distributions and \underline{s} is the position vector. Considering propagation in the y - z plane, $\underline{s} = y\underline{e}_y + z\underline{e}_z$ where \underline{e}_y and \underline{e}_z are unit vectors in y and z - directions, respectively and $k = 2\pi/\lambda$ is the wave number. Here, A_1 and A_2 represent strength of the field and λ is the wave length. Using the angular parameters shown in Fig. 3.4(b), complex amplitudes can be expressed as,

$$\left. \begin{aligned} \psi_1 &= A_1 \exp[ik(y \sin \theta_1 + z \cos \theta_1)] = A_1 e^{i\phi_1} \\ \psi_2 &= A_2 \exp[ik(y \sin \theta_2 + z \cos \theta_2)] = A_2 e^{i\phi_2} \end{aligned} \right\} \quad (3.4)$$

where $\phi_1 = (y \sin \theta_1 + z \cos \theta_1)$ and $\phi_2 = (y \sin \theta_2 + z \cos \theta_2)$. If the field strengths of the above two wave fronts are same, then $A_1 = A_2 = A$. Then,

$\psi_{total} = \psi_1 + \psi_2 = A(e^{i\phi_1} + e^{i\phi_2})$ and the resulting intensity is given by the scalar product,

$$I = \psi_{total} \cdot \psi_{total}^*$$

where ψ_{total}^* denotes complex conjugate of ψ_{total} . Hence,

$$\begin{aligned} I &= A^2 (e^{i\phi_1} + e^{i\phi_2})(e^{-i\phi_1} + e^{-i\phi_2}) \\ &= 2A^2 (1 + \cos \Delta\phi) \end{aligned} \quad (3.5)$$

where,

$$\Delta\phi = \phi_1 - \phi_2 = k[y(\sin\theta_1 - \sin\theta_2) + (\cos\theta_1 - \cos\theta_2)] \quad (3.6)$$

is the phase difference.

From Fig. 3.4(b), $\theta_1 = \theta - \alpha$, $\theta_2 = \theta + \alpha$. Substituting these in eq. (3.6),

$$\begin{aligned} \Delta\phi &= k \left[y \{ \sin(\theta - \alpha) - \sin(\theta + \alpha) \} + z \{ \cos(\theta - \alpha) - \cos(\theta + \alpha) \} \right] \\ &= 2k \sin\alpha (-y \cos\theta + z \sin\theta) \end{aligned} \quad (3.7)$$

By installing the origin on the specimen surface ($z = 0$ on the specimen), we get,

$$\Delta\phi|_{z=0} = -2ky \sin\alpha \cos\theta. \quad (3.8)$$

By combining eq. (3.7) with eq. (3.4), it can be said that intensity attains maximum value ($= 4A^2$) when $\Delta\phi = 2N\pi$, where $N=0, \pm 1, \pm 2, \dots$

Hence, $y_N = \frac{N\lambda}{2\sin\alpha \cos\theta}$ and $y_{N+1} = \frac{(N+1)\lambda}{2\sin\alpha \cos\theta}$ are locations of two consecutive bright

fringes and the associated fringe spacing is,

$$y_N - y_{N+1} = p_v = \frac{\lambda}{2\sin\alpha \cos\theta}, \quad (3.9)$$

where p_v is fringe spacing or the pitch of virtual gratings in case of two beam moiré interferometry in this study. For $\theta = 0$,

$$p_v = \frac{\lambda}{2\sin\alpha}. \quad (3.10)$$

Thus in moiré interferometry setup of the current work the virtual grating (reference) pitch is half of the initial pitch of the specimen gratings.

3.4 In-plane moiré interferometry

Single beam incidence

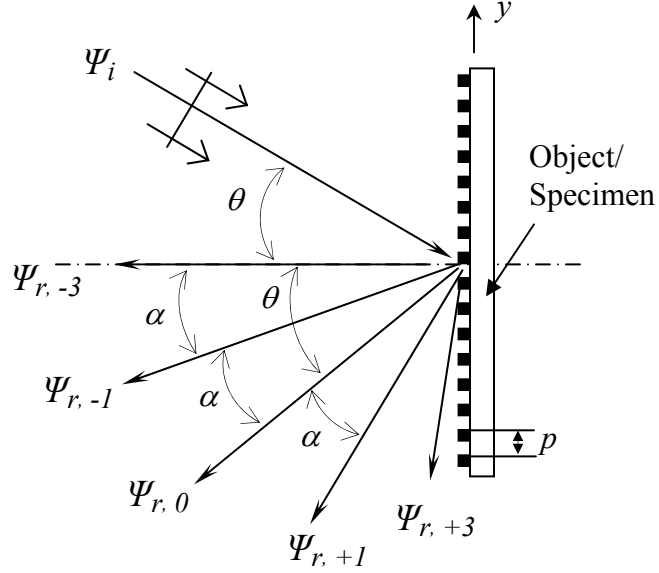


Figure 3.5: Diffraction from a grating.

The aperture function of a square wave (amplitude) gratings can be represented as,

$$t(x, y) = A + B \cos\left(\frac{2\pi y}{p}\right) - C \cos 3\left(\frac{2\pi y}{p}\right) + D \cos 5\left(\frac{2\pi y}{p}\right) - \dots$$

As it is evident from the following analysis, truncating the series after the two terms is sufficient to develop the necessary expressions for moiré interferometry. That is,

$$\begin{aligned} t(x, y) &\approx A + B \cos\left(\frac{2\pi y}{p}\right) \\ &= A + \frac{B}{2} \left(e^{-i2\pi y/p} + e^{i2\pi y/p} \right) \end{aligned} \quad (3.11)$$

Undeformed specimen

As shown in Fig. 3.5, if the gratings are illuminated by a plane wave represented by,

$$\psi_i = Re^{ik(y \sin \theta + z \cos \theta)} \quad \text{where } R \text{ is constant.}$$

$$\psi_i \Big|_{z=0} = Re^{iky \sin \theta} \quad (3.12)$$

After reflection,

$$\begin{aligned} t\psi_i &= \psi_r \Big|_{z=0} \\ &= Re^{iky \sin \theta} \left(A + Be^{i2\pi y/p} + Be^{-i2\pi y/p} \right). \end{aligned}$$

Expressing wave number as $k = \frac{2\pi}{\lambda}$,

$$\begin{aligned} \psi_r \Big|_{z=0} &= ARe^{i2\pi y \sin \theta / \lambda} + BRe^{i2\pi y \left(\frac{\sin \theta}{\lambda} + \frac{1}{p} \right)} + BRe^{i2\pi y \left(\frac{\sin \theta}{\lambda} - \frac{1}{p} \right)} \\ &= \psi_{(r,0)} + \psi_{(r,+1)} + \psi_{(r,-1)} \end{aligned} \quad (3.13)$$

where the second subscript in each term denotes the diffraction order of the wave. But, it is known that for a grating with pitch p and wave length λ , diffraction angle α can be

represented as, $\sin \alpha = \frac{\lambda}{p}$. Therefore,

$$\psi_r \Big|_{z=0} = \left[ARe^{i2\pi y \sin \theta / \lambda} + BRe^{i2\pi y (\sin \theta + \sin \alpha) / \lambda} + BRe^{i2\pi y (\sin \theta - \sin \alpha) / \lambda} \right] \quad (3.14)$$

Each term in eq. (3.14) represents diffracted waves propagating in distinctly different directions given by multiples of the diffraction angle α . If the illumination angle θ , is adjusted such that $\theta = \alpha$,

$$\psi_r \Big|_{z=0} = \left[ARe^{i2\pi y \sin \theta / \lambda} + BRe^{i2\pi y (2 \sin \alpha) / \lambda} + BR \right] \quad (3.15)$$

where $\psi_{(r,0)} = ARe^{i2\pi y \sin \theta / \lambda}$, $\psi_{(r,+1)} = BRe^{i2\pi y(2\sin \alpha) / \lambda}$ and $\psi_{(r,-1)} = BR$. That is, $\psi_{(r,-1)}$ is a wave propagating in the z -direction towards the imaging device.

Deformed specimen

The specimen grating pitch p changes when the object deforms. Using prime notation for quantities after deformation, deformed pitch $p' = p \pm \Delta p$, where change in the pitch is $\Delta p \equiv \Delta p(x, y)$.

Then, $\frac{1}{p'} = \frac{\sin \alpha'}{\lambda}$ where $\alpha' = \alpha'(x, y)$.

The counterpart of eq. (3.15) upon deformation is,

$$\psi_r' \Big|_{z=0} = \left[ARe^{ik \sin \theta} + BRe^{iky(\sin \theta + \sin \alpha')} + BRe^{iky(\sin \theta + \sin \alpha')} \right] \quad (3.16)$$

where $\psi'_{(r,0)} = ARe^{ik \sin \theta}$, $\psi'_{(r,+1)} = BRe^{iky(\sin \theta + \sin \alpha')}$ and $\psi'_{(r,-1)} = BRe^{iky(\sin \theta + \sin \alpha')}$ are the amplitudes of the diffracted wave fronts.

Dual beam incidence

As shown in Fig. 3.6, when the deformed object is illuminated by two coherent plane waves (or, collimated light beams) at angles $+\theta$ and $-\theta$ (that is $\alpha = \theta$), then,

$$\left. \begin{aligned} \psi_{i1} &= Re^{iky \sin \alpha} \Big|_{z=0} \\ \psi_{i2} &= Re^{-iky \sin \alpha} \Big|_{z=0} \end{aligned} \right\} \quad (3.17)$$

The diffracted wave fronts from the first beam are,

$$\begin{aligned}\psi'_{r1} &= \left[ARe^{ik\sin\theta} + BRE^{iky(\sin\theta+\sin\alpha')} + BRE^{iky(\sin\theta+\sin\alpha')} \right] \\ &= \psi'_{(r1,0)} + \psi'_{(r1,+1)} + \psi'_{(r1,-1)}\end{aligned}$$

Similarly the diffracted wave fronts due to the second incident beam are,

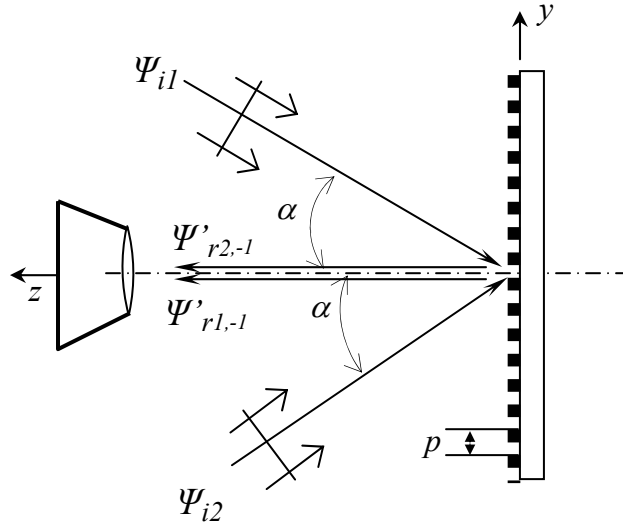


Figure 3.6: Moiré interferometry principle.

$$\begin{aligned}\psi'_{r2} &= \left[ARe^{-ik\sin\theta} + BRE^{-iky(\sin\theta+\sin\alpha')} + BRE^{-iky(\sin\theta+\sin\alpha')} \right] \\ &= \psi'_{(r2,0)} + \psi'_{(r2,+1)} + \psi'_{(r2,-1)}\end{aligned}$$

In Fig. 3.6 only $\psi'_{(r1,-1)}$ and $\psi'_{(r2,-1)}$ orders are shown for clarity. These two waves propagate along the optical axis (z-axis), towards the imaging device (a camera). The total complex amplitude registered on the camera plane is given by,

$$\begin{aligned}\psi_{camera} &= \psi'_{(r1,-1)} + \psi'_{(r2,-1)} \\ &= BR(e^{iky(\sin\theta+\sin\alpha')} + e^{-iky(\sin\theta+\sin\alpha')})\end{aligned}$$

The corresponding intensity distribution on the image plane is given by,

$$I_{camera} = \psi_{camera} \cdot \psi_{camera}^*$$

$$= 2(BR)^2 [1 + \cos 2ky(\sin \theta - \sin \alpha')] \quad (3.18)$$

Here, α and θ being equal to each other eq. (3.18) represents low frequency intensity variation representing moiré fringes as,

$$I_{camera} = 2(BR)^2 \left[1 + \cos 2\pi y \left\{ 2 \left(\frac{1}{p} - \frac{1}{p'} \right) \right\} \right] \quad (3.19)$$

Equation (3.19) is similar to the one obtained for describing interference patterns when

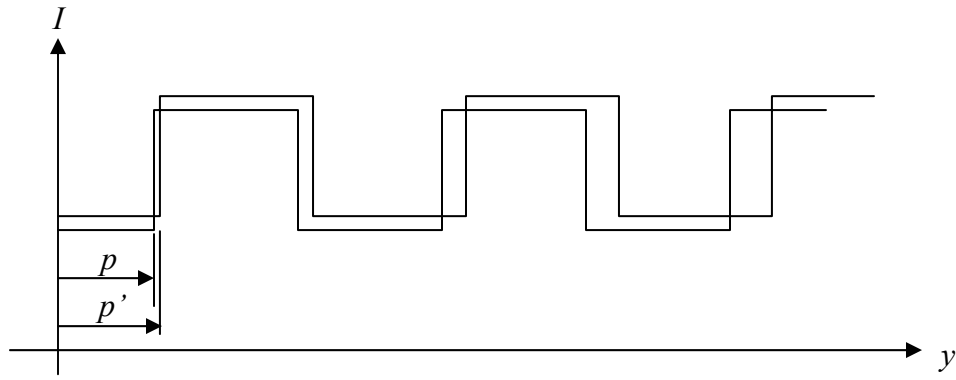


Figure 3.7: Double exposure moiré interferometry principle.

two linear geometric patterns (gratings) of pitch p and p' are physically superimposed or doubly exposed on a single film or sensor [31]. For example, a square wave grating affixed to the object (Fig. 3.7) and exposed on a film can be represented in terms of the

fundamental harmonic as, $I_1 = A \left(1 + \cos \frac{2\pi y}{p} \right)$ after truncating the higher order terms

where p is the grating pitch and grating lines are along the x direction (y -direction is the principal direction). In Fig. 2.7 the waveforms are shown spatially separated in the vertical direction for clarity.

If the grating upon loading changes its pitch locally to p' the changed profile can be expressed as $I_2 = A \left(1 + \cos \frac{2\pi y}{p'} \right)$. If a single film records both unchanged and changed profile the resulting intensity is expressed as,

$$\begin{aligned}
 I_{total} &= I_1 + I_2 = A \left(2 + \cos \frac{2\pi y}{p} + \cos \frac{2\pi y}{p'} \right) \\
 &= 2A \left(\underbrace{1 + \cos 2\pi y \left(\frac{1}{p} + \frac{1}{p'} \right)}_{\text{Carrier fringes}} \underbrace{\cos 2\pi y \left(\frac{1}{p} - \frac{1}{p'} \right)}_{\text{Moiré fringes}} \right) \tag{3.20}
 \end{aligned}$$

In eq. (3.20) $\cos 2\pi y \left(\frac{1}{p} + \frac{1}{p'} \right)$ represents ‘high frequency’ carrier fringes and

$\cos 2\pi y \left(\frac{1}{p} - \frac{1}{p'} \right)$ represents ‘low frequency’ moiré fringes. Since the high frequency

information is ordinarily invisible the low frequency moiré signal can be isolated. The corresponding displacement represented by the geometric interference is given by,

$$v = Np, \quad N = 0, \pm 1, \pm 2, \dots \tag{3.21}$$

In the current work, for specimen gratings pitch $p = 5.08 \mu\text{m}$ ($\frac{1}{p} = 5000$ cycles/inch) corresponding virtual gratings pitch $p_v = 2.54 \mu\text{m}$ ($\frac{1}{p_v} = 10000$ cycles/inch).

Therefore, the governing equation of moiré interferometry for the current work is given by,

$$v = N \frac{p}{2}, \quad N = 0, \pm 1, \pm 2, \dots \tag{3.22}$$

Thus eqs. (3.22) and (3.2) are the same equations where pitch of the virtual gratings is $p_v = \frac{P}{2}$. This is also evident if the cosine terms representing moiré fringes in eqs. (3.19) and (3.20) are compared. Thus the sensitivity of moiré interferometry is twice than the geometric moiré.

3.5 Benchmark experiment

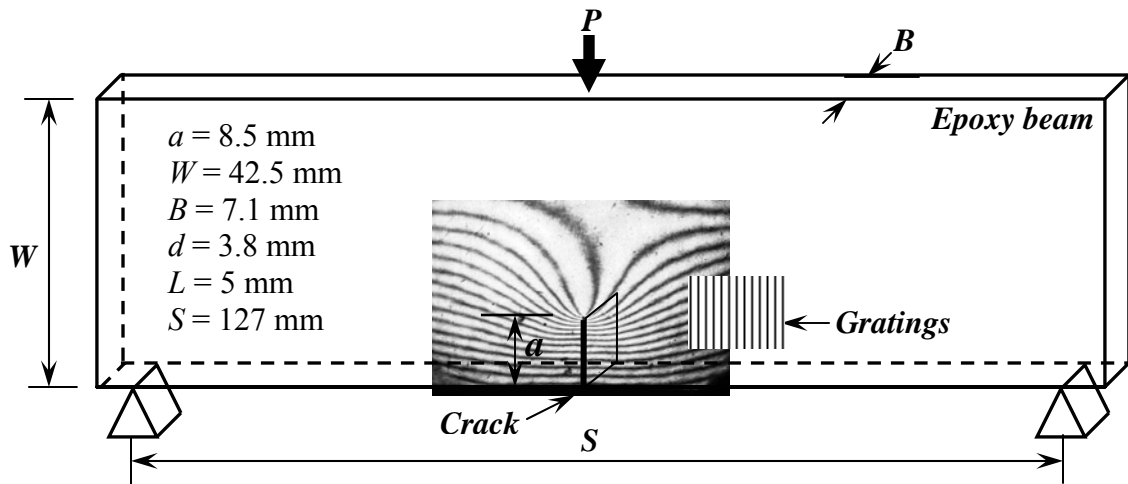


Figure 3.8: Neat epoxy three-point bend sample

Neat epoxy beam samples were fabricated as described in the previous chapter and gratings were printed in the area of interest. An edge notch was cut and sharpened using the method described previously. The resulting specimen geometry is shown in Fig 3.8 with an interferogram of moiré fringes representing crack opening displacement around the crack-tip. Experiments were performed in three-point bending configuration and interferograms were recorded at different load levels (P). Several selected interferograms from a test are shown in Fig. 3.9 and the fringe sensitivity is $1.25 \mu\text{m}/\text{half-}$

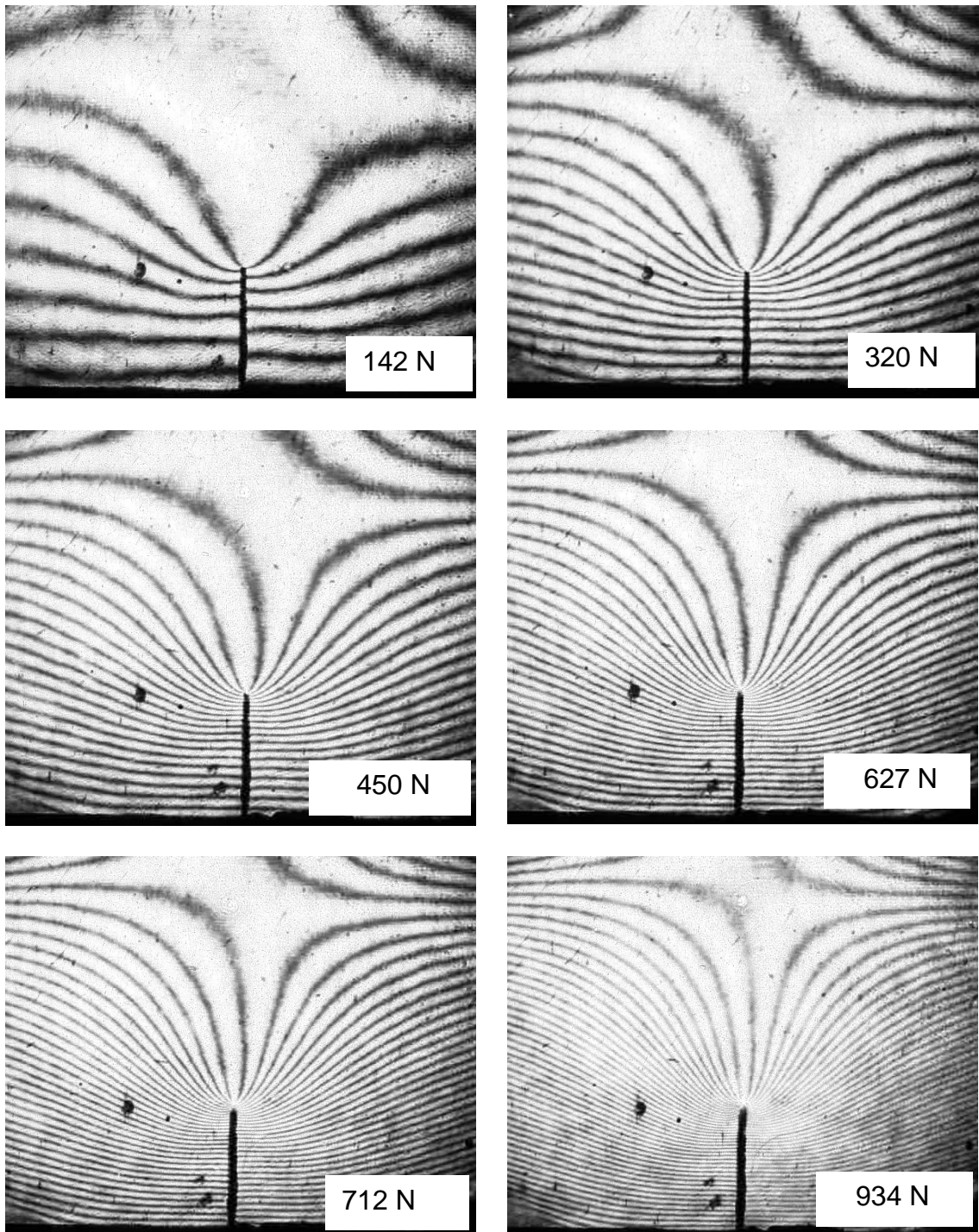


Figure 3.9: Interferograms showing evolution of opening displacement field around the crack-tip in neat epoxy sample. (Sensitivity = $1.25 \mu\text{m}/\text{half-fringe}$)

fringe. The pattern shows nearly symmetric crack opening displacement contours indicative of mode-I loading of the crack tip. An interactive MATLABTM code was developed to digitize fringes and record fringe location relative to the crack tip. From the digitized data crack opening displacements and hence crack mouth opening displacements (CMOD) at the specimen edge for various load levels were determined using governing equation (eq. (3.22)) of moiré interferometry.

Displacements along $(r, \theta=180^\circ)$ were also extracted from different interferograms to determine mode-I stress intensity factors (K_I) as a function of the applied load. The displacement regression method was used for evaluating values of K_I from each interferogram. Using Williams' asymptotic expansion [32] for mode-I crack opening displacements for plane stress assumption is given by,

$$Ev = 2A_1 r^{1/2} \left[2 \sin \frac{\theta}{2} - (1 + \nu) \sin \frac{\theta}{2} \cos \frac{\theta}{2} \right] - 2\nu A_2 r^1 \sin \theta \\ + \frac{2}{3} A_3 r^{3/2} \left[2 \sin \frac{3\theta}{2} - (1 + \nu) \frac{3}{2} \sin \theta \cos \frac{\theta}{2} \right] - \nu A_4 r^2 \sin 2\theta + \dots \quad (3.23)$$

In the above A_i ($i=1, 2, 3\dots$) are coefficients of each term and A_1 is related to mode-I stress intensity factor (SIF) as $K_I = A_1 / \sqrt{2\pi}$. Also, E is the Young's modulus, ν is crack opening displacement, ν is the Poisson's ratio, r is radial distance measured from the crack tip and θ is angular coordinate. By truncating the series in eq. (3.23) after the first term,

$$Ev = 2 \frac{(K_I)_{app}}{\sqrt{2\pi}} r^{1/2} \left[2 \sin \frac{\theta}{2} - (1 + \nu) \sin \frac{\theta}{2} \cos \frac{\theta}{2} \right], \quad (3.24)$$

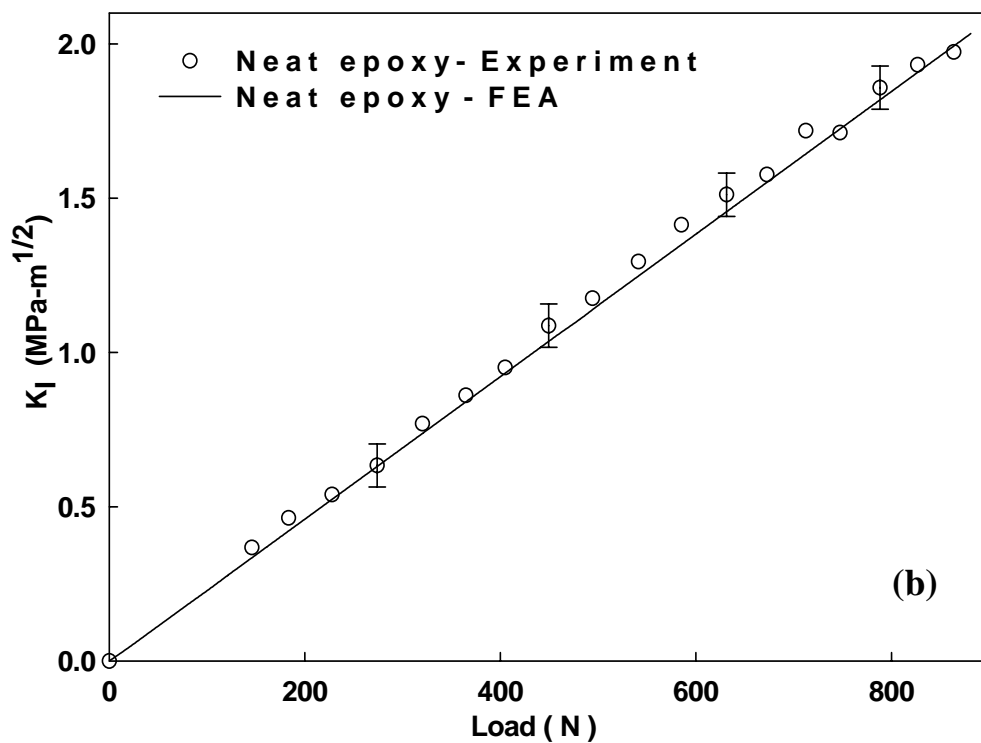
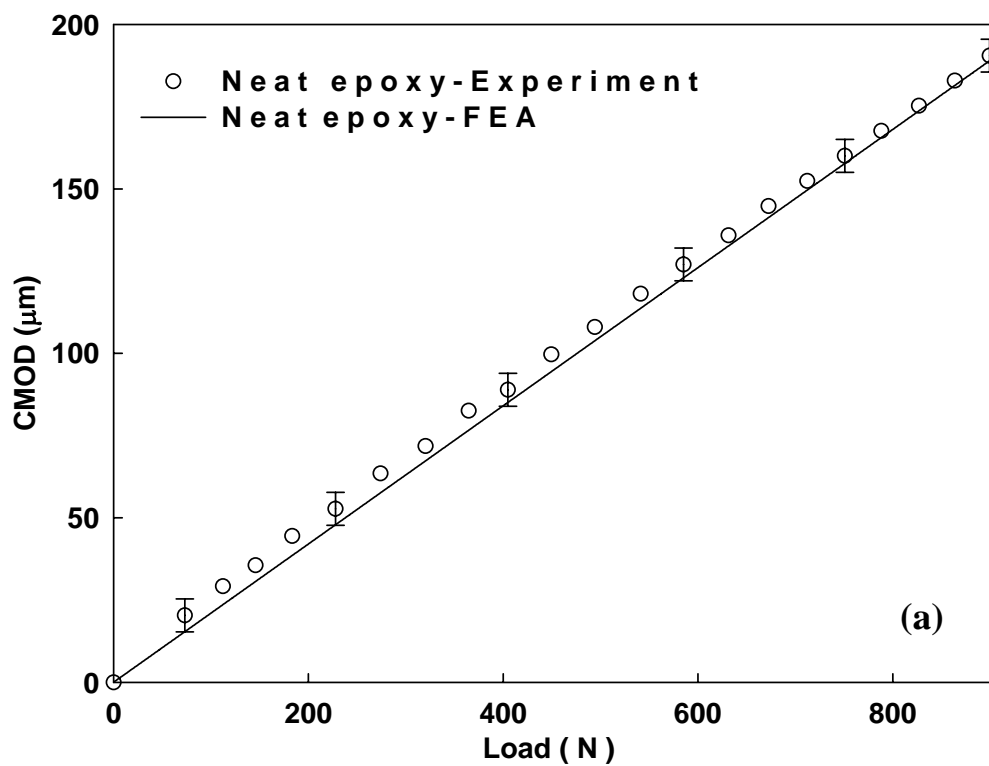


Figure 3.10: Results from benchmark study: (a) Variation for CMOD with load. (b) Variation of mode -I SIF with load.

where $(K_I)_{app}$ denotes the apparent stress intensity factor. Along $\theta = \pm\pi$, say $\theta = +\pi$ apparent stress intensity factor can be written as,

$$(K_I)_{app} = \frac{Ev\sqrt{2\pi}}{4\sqrt{r}}. \quad (3.25)$$

Using eq. (3.25), by plotting K_I as a function of r , one can perform linear regression of $(K_I)_{app}$ values to find K_I as [33, 34],

$$K_I = \lim_{r \rightarrow 0} (K_I)_{app}. \quad (3.26)$$

The experimental results of CMOD and K_I thus obtained as a function of applied load are shown in Figs. 3.9(a) and (b), respectively. Both variations are essentially linear, as expected for a nominally elastic material such as epoxy used in the current investigation.

A finite element model of the same problem was also developed using structural analysis software ANSYSTM (Version 10.0). Isoparametric quadrilateral elements with midside nodes were used to model the problem in two dimensions under plane stress conditions. The region around the crack-tip was meshed with fine elements to ensure accuracy of the solution. Smallest element size near the crack-tip was approximately $0.005a$ where a is the crack length. No special elements were used to enforce singularity at the crack-tip. Fracture parameters such as CMOD and mode-I stress intensity factors were extracted from the numerical solution. The finite element results for CMOD and mode-I SIF are also shown in Figs. 3.10(a) and (b), respectively, as solid lines. Finite element results are in very good agreement with experimental data.

Strain data were also extracted from interferograms along a line $(x/L \approx 0.6, y/L)$ (x and y is normalized by L , the distance between the crack tip and the

inclusion in a crack-inclusion specimen, to be described in the next chapter) ahead of the crack tip. A central difference scheme without any data smoothing was used to extract strain values from interferograms. The strains were calculated as engineering strains using the following relationship,

$$\varepsilon_y = \frac{\partial v}{\partial y} = p_v \left[\frac{\partial N_y}{\partial y} \right] \quad (3.27)$$

where p_v pitch of the virtual gratings and N_y is fringe order in the y -direction. Thus obtained strain data was normalized by the maximum tensile strain in an uncracked homogeneous epoxy beam strain,

$$(\varepsilon_y)_{beam} = \frac{3PS}{2EBW^2}, \quad (3.28)$$

where P is the applied load, S , W , B are specimen dimensions (See Fig. 3.8) and E is the Young's modulus. The corresponding strain plot is shown in Fig. 3.11(a) as a function of normalized y for various load levels. As expected, the strain data is relatively noisy due to numerical differentiation and potential digitization errors, particularly close to ($y/L=0$) where optical data tends to be sparse for a mode-I crack tip. The strain data from four different load levels are shown in Fig 3.11 and the data sets overlap on each other as expected. Also shown in the same plot is the strain variation obtained from the finite element model along the same line showing good agreement in the overall strain variation trends as well as magnitudes.

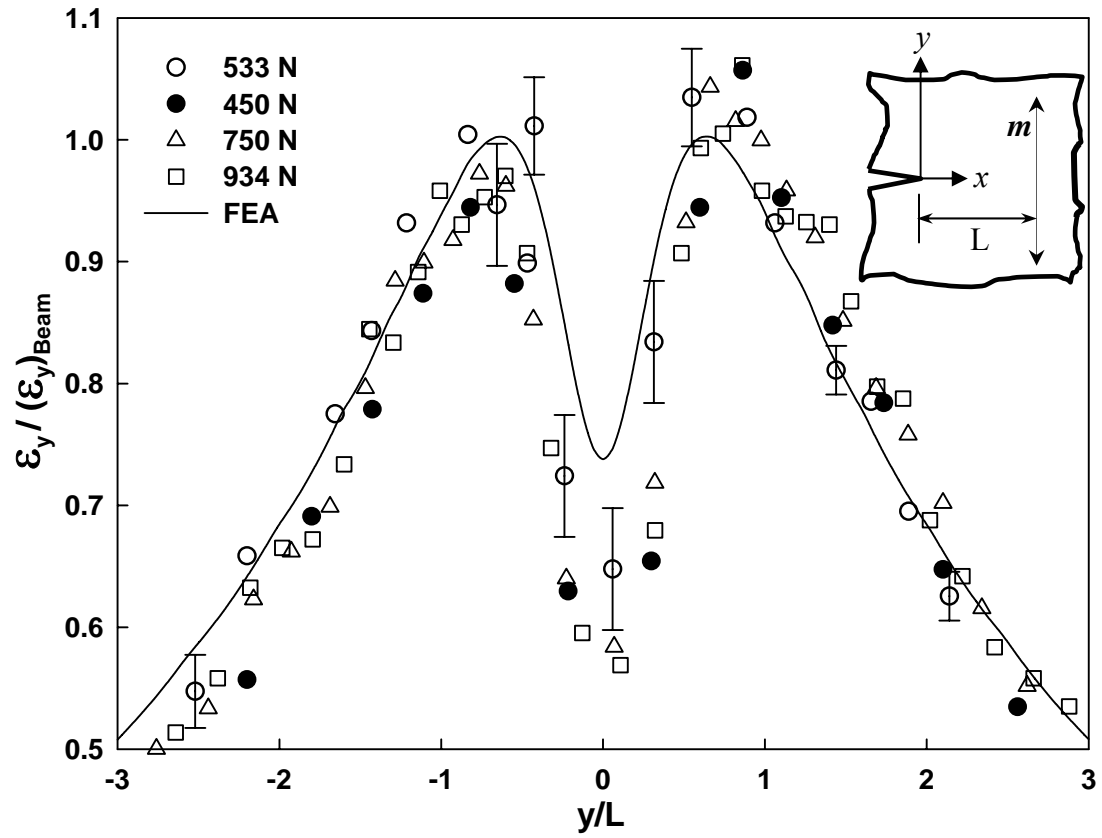


Figure 3.11: Comparison of strain distribution in neat epoxy sample along line $x \sim 3$ mm ($L = 5$ mm, and indicated by 'm') from moiré data and finite element analysis.

CHAPTER 4

CRACK-INCLUSION INTERACTION

In this chapter experimental results from crack-inclusion interaction studies are described. The specimens previously discussed are studied using moiré interferometry and dominant crack opening displacements in the crack-inclusion vicinity are obtained. Details of fracture parameters such as crack mouth opening displacements (CMOD) and hence stress intensity factors are assessed as a function of applied load. Using measured displacements, strains are estimated at strategic locations near the inclusion. Experimentally obtained data will be compared to numerical results in the next chapter.

4.1 Interaction between crack and inclusion

Edge notched crack-inclusion specimens were fabricated using the method described in Chapter 2. The notch was sharpened by razor blade insertion apparatus discussed earlier. A schematic of a crack-inclusion specimen with an illustration of the crack-tip coordinate system, gratings direction and loading configuration is shown in Fig. 4.1. A typical moiré fringe pattern is also shown in the region of interest. The experimental procedure adopted is the same as the one described in Chapter 3. The contours of crack opening displacement field (displacements along the y-direction) were recorded as moiré interferograms (sensitivity $1.25 \mu\text{m}/\text{half-fringe}$). Figure 4.2 shows a

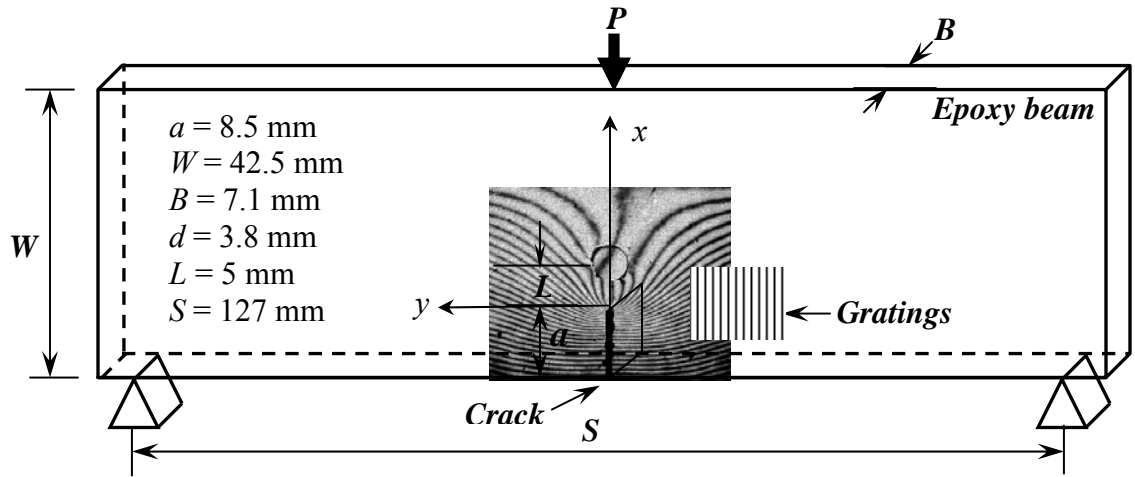


Figure 4.1: Crack-inclusion specimen geometry loading configuration and crack-tip coordinate system.

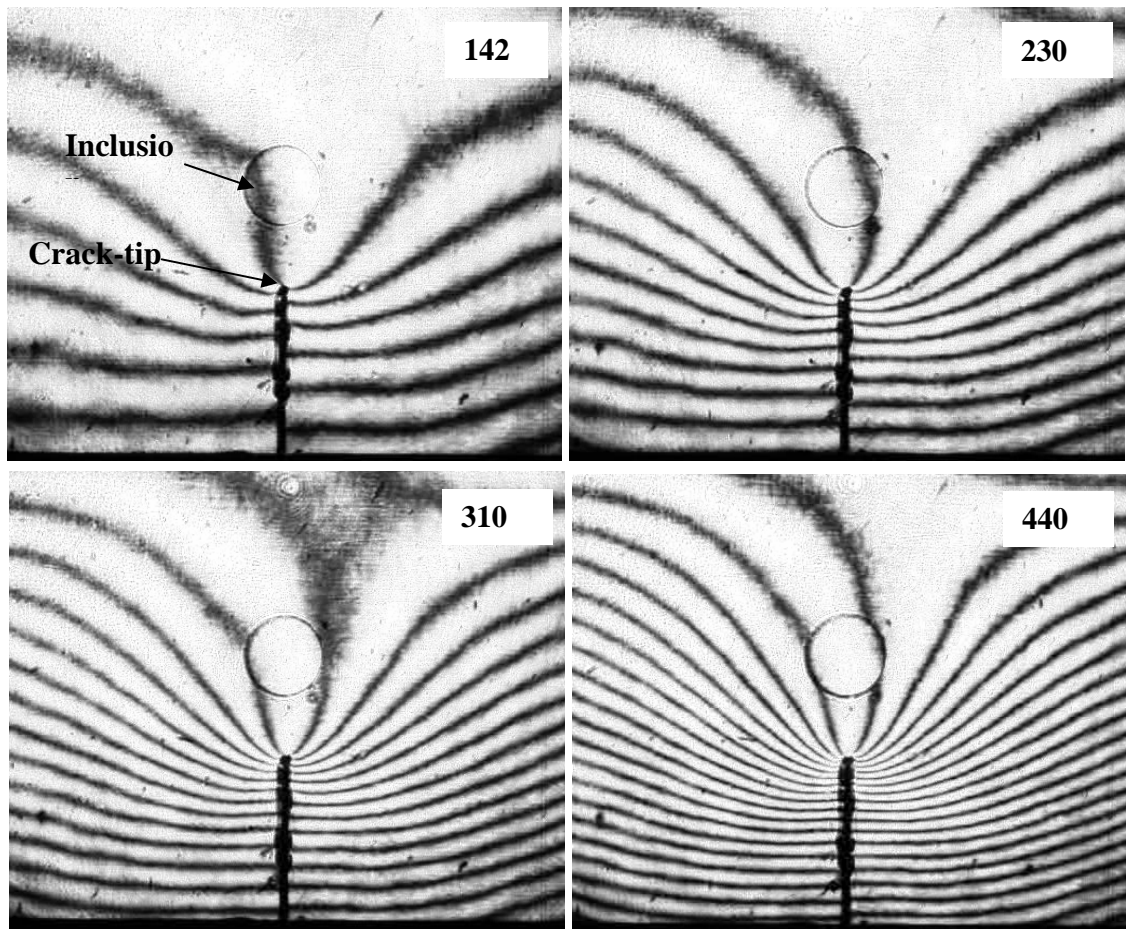


Figure 4.2: Selected moiré interferograms of crack-inclusion specimen before debonding occurs between inclusion and matrix.

few moiré fringe patterns form a crack-inclusion interaction experiment at selected load levels in the vicinity of a crack-inclusion pair. In this case, the inclusion diameter d is 3.8 mm and the distance between the crack tip and the inclusion center L is 5 mm which corresponds to a L/d ratio of 1.31. The fringes show typical mode – I crack-tip opening displacement field with reasonably good symmetry relative to the crack plane. It can be readily observed from these fringes that displacement contours around the crack-tip and near to the inclusion are continuous during this part of the loading phase. As the applied load is increased, occurrence of debonding between the inclusion and the matrix was

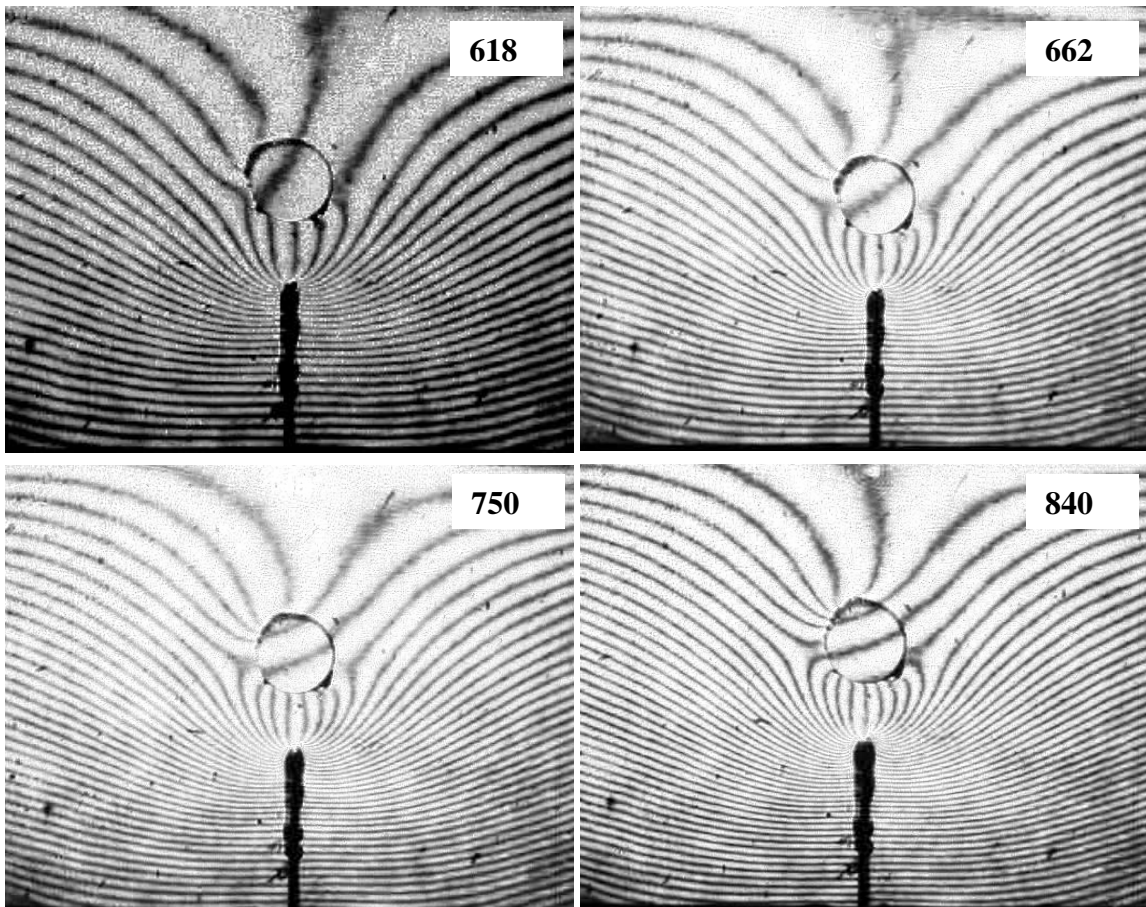


Figure 4.3: Selected moiré interferograms of crack-inclusion specimen after debonding between inclusion and matrix.

observed and the resulting moiré interferograms from the same experiment are shown in Fig. 4.3 for a few selected load levels. Onset of debonding can easily be detected from successive interferograms by visual inspection of fringe pattern near the matrix-inclusion interface. Debonding results in discontinuous fringes around the inclusion. The fringes observed within the inclusion are parallel to each other and are equally spaced indicating rigid rotation of the inclusion after debonding, possibly due to friction and/or incomplete debonding between the inclusion and the matrix. A jump in the number of fringes (4-6) around the crack was generally observed immediately following the onset of debonding.

4.2 Fracture parameters and strains

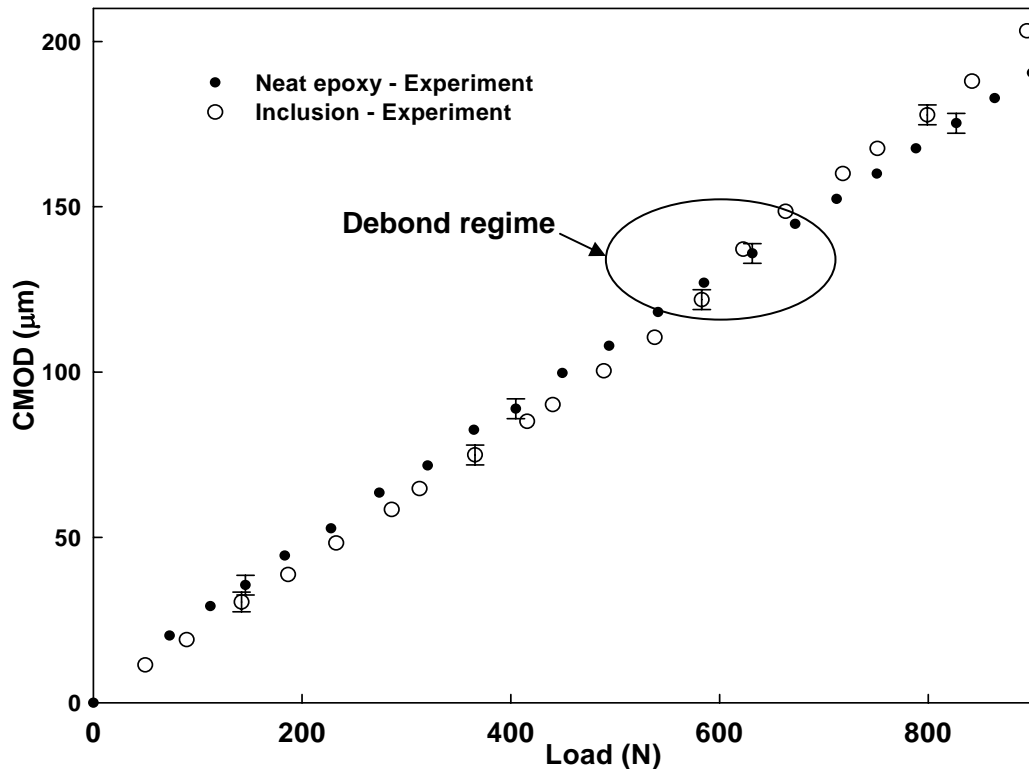


Figure 4.4: Comparison between experimentally obtained crack mouth opening displacements for the crack-inclusion and neat epoxy specimens with load.

CMOD was calculated by counting the number of fringes around the crack to the sample edge and by using characteristic equation of moiré interferometry. The results for the experiment are shown in Fig. 4.4. CMOD data for previously discussed neat epoxy specimen are also shown on the same plot for comparison between the two. Regime during the loading phase when debonding begins can be perceived by visual inspection of interferograms and that region is highlighted in Fig. 4.4. From the graph it can be observed that CMOD values in the crack-inclusion specimen are lower than its neat epoxy (without inclusion) counterpart before the onset of debonding. A noticeable

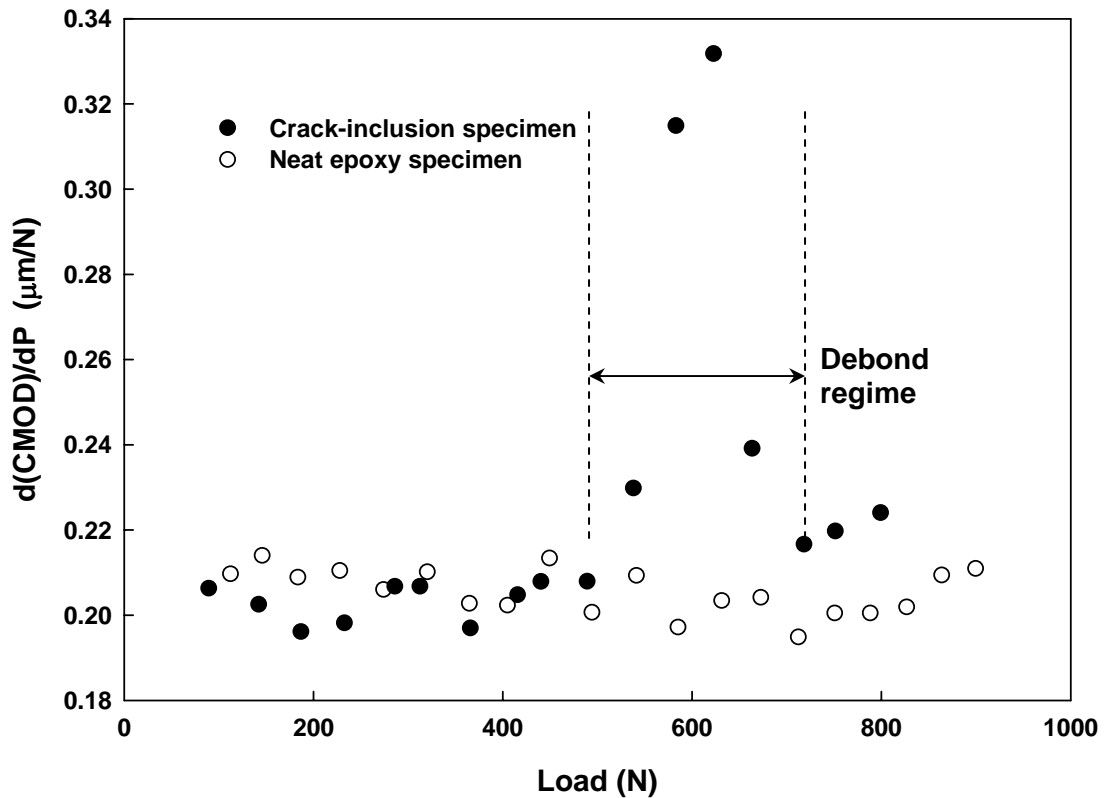


Figure 4.5: Comparison of experimentally obtained variation of crack mouth compliance with applied load for crack-inclusion and neat epoxy specimens.

jump in CMOD as a consequence of debonding is evident and hence in the post-debonding regime where CMOD values for the crack-inclusion specimen is generally greater than its neat epoxy counterpart. This is better evident from crack mouth compliance ($d(CMOD)/dP$) values calculated from CMOD values by using a simple central differencing scheme and are shown in Fig. 4.5. Crack mouth compliance calculated in the same manner for the neat epoxy case is also shown on the same plot for comparison. Evidently, the crack mouth compliance for the neat epoxy case is nearly constant as expected for a homogeneous linear elastic material. The crack-inclusion specimen also shows a similar behavior before the onset of debonding but with compliance values somewhat lower than the neat epoxy case. However, the sharp rise in

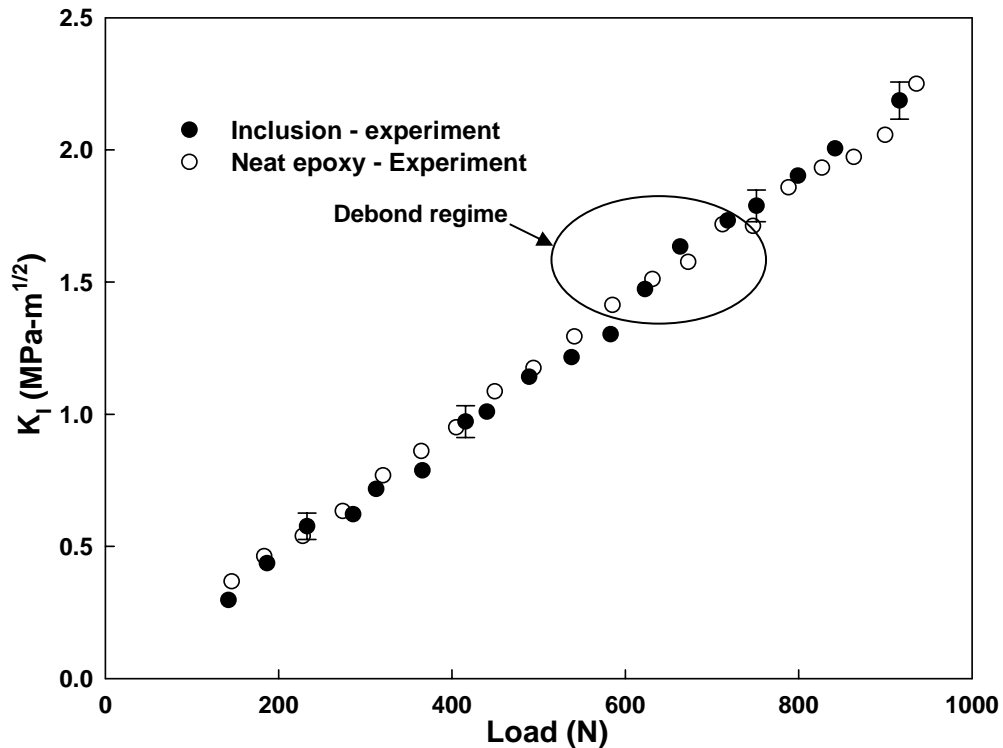


Figure 4.6: Variation of mode-I SIF with load for crack-inclusion specimen.

compliance for the crack-inclusion case is associated with occurrence of debonding which results in a peak as it can be seen from the plot. Further, the crack mouth compliance values are consistently higher than the ones for neat epoxy in the post-debonding regime.

Using linear regression method described in Chapter 3, mode – I stress intensity factors were also calculated from crack opening displacements along crack faces ($\theta = \pm\pi$) and a plot of mode-I SIF (K_I) for crack-inclusion specimen is also shown in Fig. 4.6. Again the response is generally linear as expected with the exception of a noticeable jump in K_I values when debonding occurs.

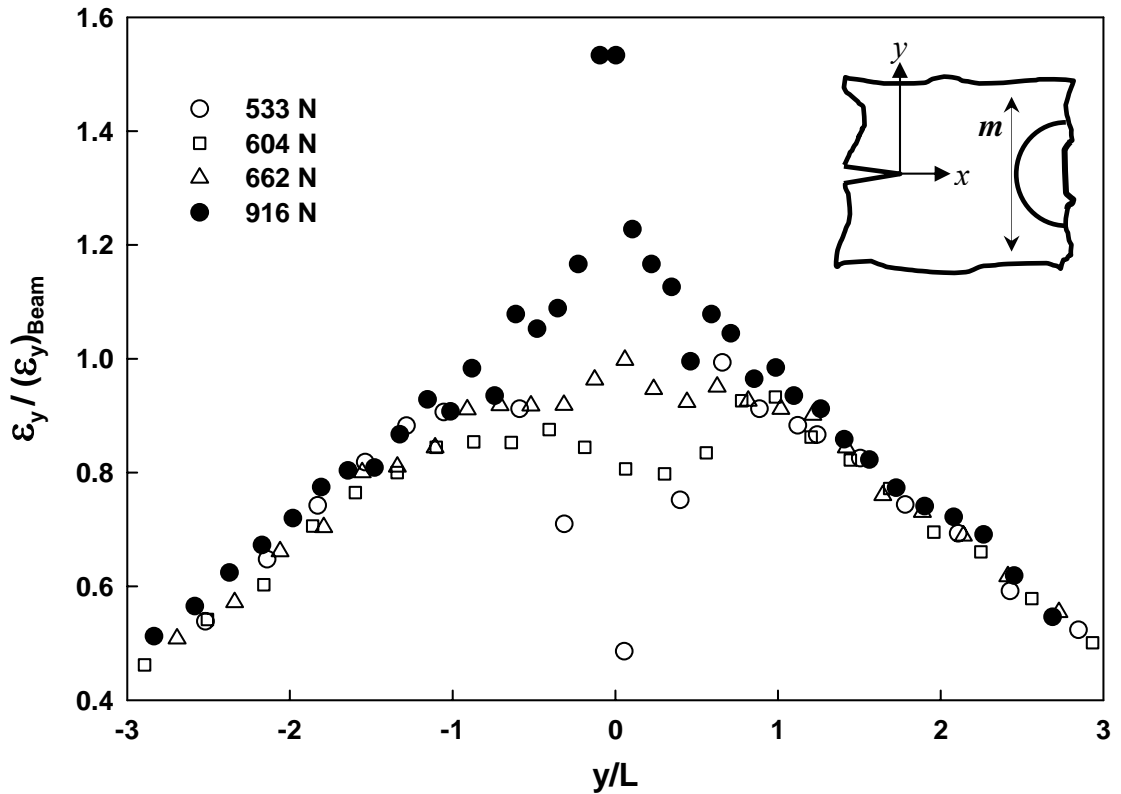


Figure 4.7: Strain field evolution along ($x/L \sim 0.6, y/L$) (shown by line ‘m’) during the loading phase.

Evolution of dominant strain ε_y along a line orthogonal to the crack and at $(x/L \approx 0.6, y/L)$ ahead of the crack tip (between the crack tip and the inclusion and nearly tangential to the inclusion) is shown in Fig. 4.7. The strains are normalized with respect to an uncracked homogeneous beam sample of same loading configuration and geometry as described by eq. (3.20). Load levels 533 N in the strain plot shown in Fig. 4.7 corresponds to the loading phase before debonding. Whereas, load level 604 N and 662 N corresponds to debonding regime and load level 916 N corresponds to an applied load well after debonding. It can be seen from the plot that there is substantial redistribution of strains ahead of the crack tip following the onset of debonding of the inclusion from the matrix. After debonding occurs, strains close to $y/L = 0$ increase drastically and attain a peak value. This can also be observed qualitatively in the decreasing fringe spacing near the inclusion-matrix interface along $y/L = 0$. The contrast between an edge cracked neat epoxy specimen (see Fig. 3.10) and crack-inclusion specimen (see Fig. 4.7) in terms of normalized strain can be readily observed. The strains before debonding occurs are lower in case of the crack-inclusion specimen compared to the neat epoxy specimen due to shielding of the crack tip by the rigid inclusion. Due to occurrence of debonding these shielding effects are compromised and strain values show sharp increase near the inclusion-matrix interface. Noticeably, the strain redistribution is a highly localized phenomena and strains remain unaffected beyond $y/L \sim \pm 1$. It is also evident from Fig. 4.7 that during debonding, the strain distribution in the inclusion vicinity is asymmetric with respect to $y/L=0$. This is attributed to competing debond fronts around the inclusion.

4.3 Experimental repeatability

Results from two crack-inclusion interaction experiments are shown in Fig. 4.8 to address the repeatability of the crack-inclusion interaction behavior. The plot shows variation of CMOD values for two crack-inclusion specimens. The pre-debonding behavior is quite repeatable as can be seen from the graph whereas post-debonding variation is within 10 μm of each other. Both experiments show occurrence of inclusion debonding at approximately same load level and show a jump in the CMOD values. The

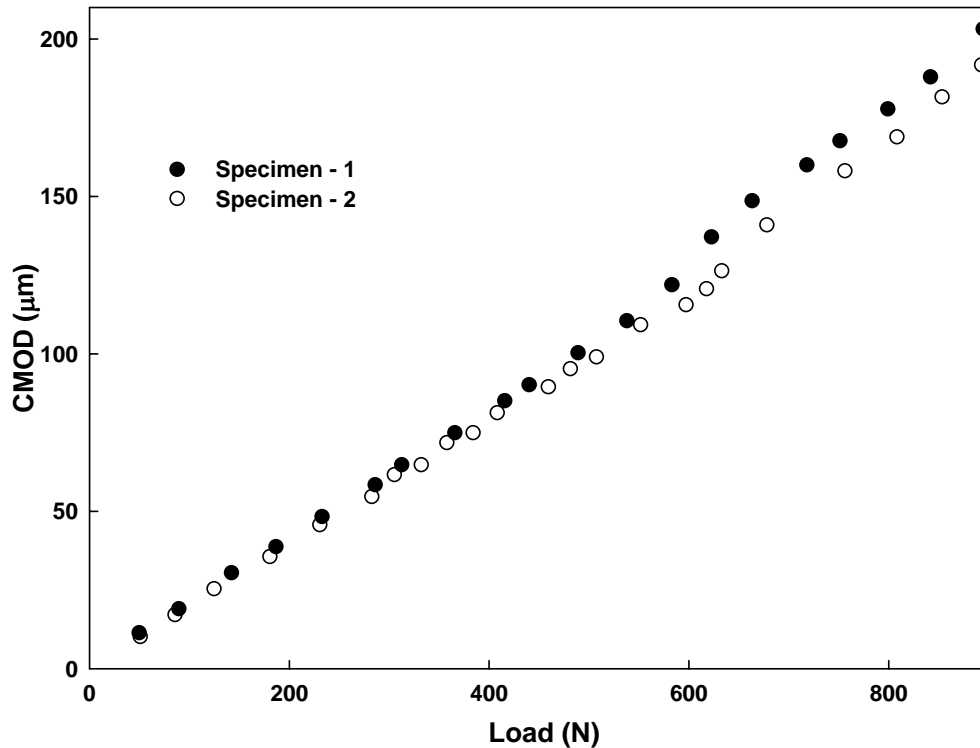


Figure 4.8: CMOD variation with load for two different crack-inclusion specimens.

differences in post-debonding behavior can be attributed to various reasons. The first and the most crucial is homogeneity of bond strength that can be produced between the inclusion and the matrix in different specimens. Due to manual treatment of glass

cylinders with silane some difference is expected in the bond between matrix and inclusion in terms of the bond strength. This coupled with large stress gradient due to the crack tip field may compound any such deviation. Another potential reason is unavoidable errors due to experimental limitation in achievable symmetry and relative

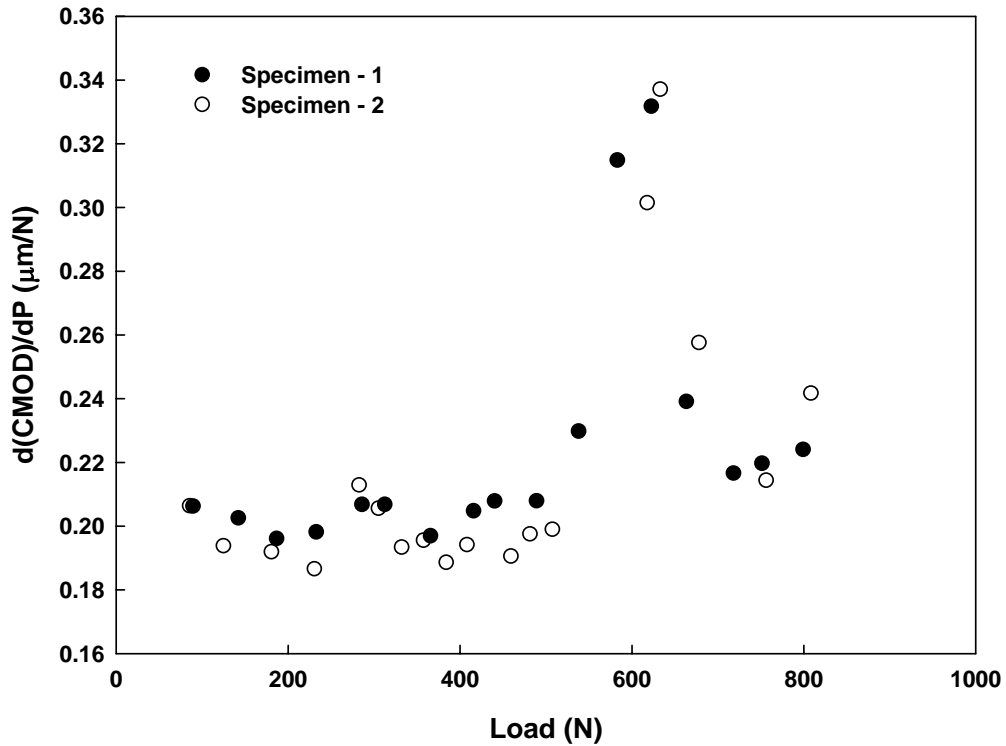


Figure 4.9: Crack compliance variation with load for two different crack-inclusion specimens.

location of crack tip and the inclusion. These result in debond front selecting a dominant path on either side of the inclusion. However, in the post-debonding regime (well after the completion of debonding) the two graphs are basically parallel to each other.

Experimental repeatability is better visualized by the crack mouth compliance plots for the two experiments and are shown in Fig. 4.9. The occurrence of debonding is evident by the steep increase in the compliance values and a distinctly different plateau values before and after debonding.

CHAPTER 5

FINITE ELEMENT MODELING

An approach based on deactivation of stiffness for elements meeting certain specified failure criteria has been used in a few previous works to simulate initiation and progression of fracture in materials. Al-Ostaz and Jasiuk [35] simulated crack growth and propagation in porous materials under uniaxial tension. They investigated crack trajectories in perforated epoxy sheets by considering elastic strain energy and maximum in-plane normal principal stress based failure criteria for simulating progressive failure. Ko *et. al.* [36] used this method to simulate fracture in a punch problem dominated by shear failure with a ductile-fracture criterion based on effective strain. They compared numerical results to the ones from experiments and showed that an improved solution can be obtained if fracture strain of the material is determined experimentally and then used as an input in the numerical model.

This chapter describes modeling and simulation of the crack-inclusion interaction including debonding of inclusion-matrix interface. Element stiffness deactivation method is used in the current work to simulate onset and evolution of debonding. A finite element model was developed in ANSYSTM [37] structural analysis environment for static analysis of crack-inclusion interaction. ANSYS APDL (ANSYS Parametric Design Language) macros were used for pre- and post-processing of numerical data. A

parametric study was performed with respect to some of the geometrical parameters of the model.

5.1 FEA model description

Under plane stress assumptions the finite element model was defined by specifying keypoints, joining them by lines and then creating areas in 2-D space. The three-point-bend geometry (152mm x 42.5mm x 7.1mm), same as the one used in experiments, was created in this manner. A symmetrically located sharp crack was modeled by creating unmerged areas having common sides forming the two crack faces. Isoparametric quadrilateral elements with mid-side nodes were used to create a controlled mesh for the whole model. A representative finite element mesh used in the simulation performed to complement experiments is shown in Fig. 5.1(a). Figure 5.2(b) shows an enlarged view of the mesh in vicinity of the crack tip and inclusion pair. A very fine mesh was used in the region of interest namely, in the vicinities of the crack-inclusion pair and the inclusion-matrix interface to capture steep gradients of mechanical field quantities. A distinct set of elements forming the interface between the inclusion and the matrix was generated as shown in Fig. 5.1(b). This interfacial layer was modeled to have a thickness of $\sim d/100$, d being the inclusion diameter. The geometrical parameters and the coordinate systems involved are shown schematically in Fig. 5.2. In addition to the crack tip coordinate system with origin at O , a cylindrical coordinate system with origin O' was also considered. In Fig. 5.2, L is the distance between the crack tip and the center of the inclusion, d is inclusion diameter and a is crack length. Next, the

methodology to simulate debonding between the inclusion and the matrix during the loading phase is discussed.

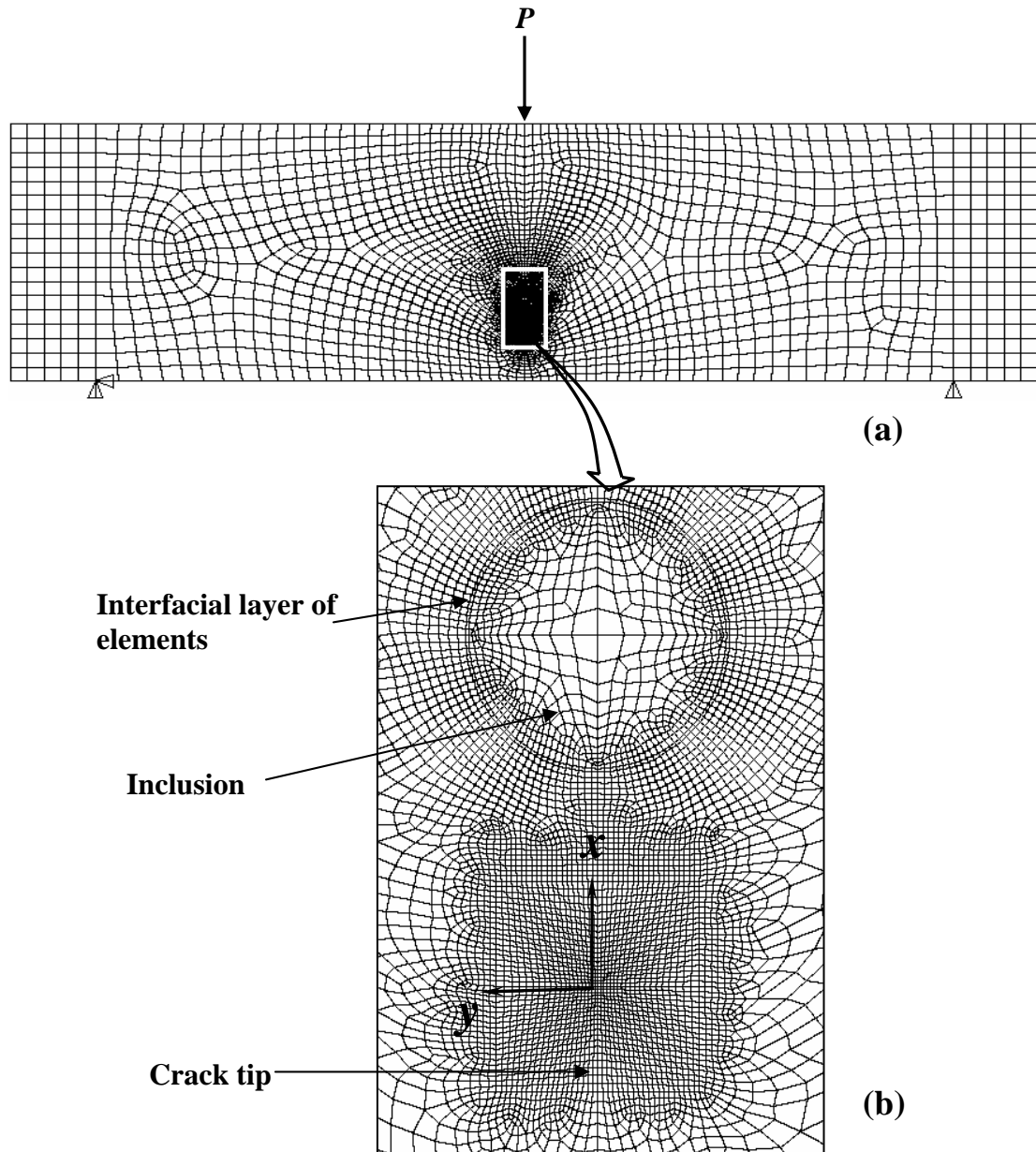


Figure 5.1: (a) Finite element mesh used for simulating crack-inclusion interaction in a three-point bend specimen (b) Enlarged view of the mesh in the vicinity of crack-tip and inclusion.

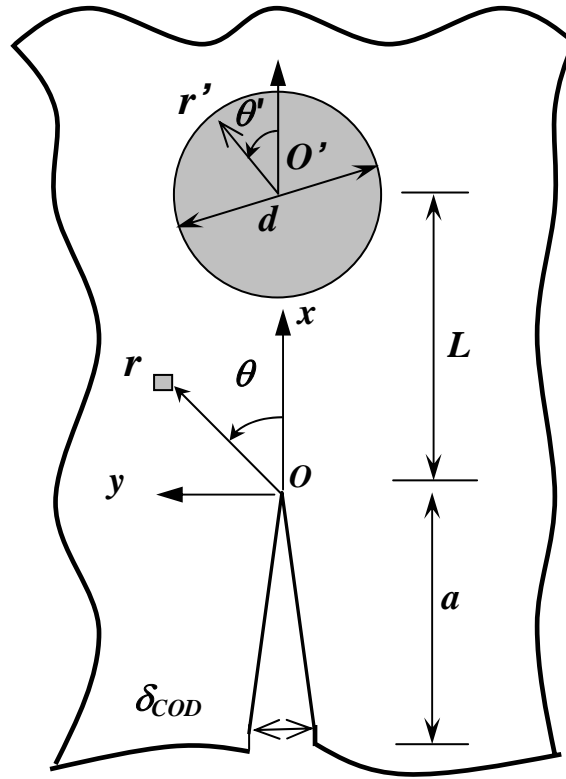


Figure 5.2: Crack tip and inclusion coordinate systems.

5.2 Inclusion-matrix debonding

A criteria based on the ultimate strength of epoxy was hypothesized to simulate debonding of the inclusion from matrix. The aforementioned interfacial elements that constitute the bond layer were useful for this. Failure due to radial stress (relative to the origin (O') defined at the inclusion center) was considered for debonding of inclusion-matrix interface. It was hypothesized that debonding occurs when radial stress attains a fraction of the ultimate stress of the matrix material in these elements. Quasi-static symmetric loading (P) was applied to the model with an increment of 20 N per step to

achieve mode – I conditions. During the loading phase, elements in this bonding layer were monitored for radial stress with respect to the cylindrical coordinate system with origin at the inclusion center. Post-processing was carried out at the end of each load step and beyond a predefined value of positive radial stress to ‘kill’ (or deactivate) the bond layer elements using ‘element death’ (EKILL) option available in ANSYS. A user defined macro using ANSYS APDL was developed for this purpose (see, Appendix A). To achieve the desired effect the program does not actually remove the ‘killed’ elements in the model. Instead, elements meeting a stipulated criterion are deactivated by multiplying their elemental stiffness by a severe reduction factor. In this work a reduction factor of 1×10^{-8} was used. This prevents those deactivated elements from contributing to the overall stiffness of the structure. That is, the respective rows and columns of the stiffness matrix are made negligibly small without replacing them by zeros. Respective loads in the load vector are also zeroed out but not removed from the vector. Strain and stress values of all ‘killed’ elements are set to zero as soon as the elements are deactivated. At the same time, large deformation effects are invoked for these elements to achieve meaningful results. As mentioned earlier, the criteria proposed for deactivation of an element in the bond layer is,

$$(\sigma_{rr})_{cr} = \beta \sigma_o, \quad (5.1)$$

where $(\sigma_{rr})_{cr}$ is the critical radial stress relative to the cylindrical coordinate system with its axis centered at O' , σ_o is the strength of matrix material and β is a scalar ($0 \leq \beta \leq 1$). The value of σ_o was used as 63 MPa for epoxy based on tensile test data shown in Fig. 4.16. A flow chart in Fig. 5.3 shows the analysis methodology described above.

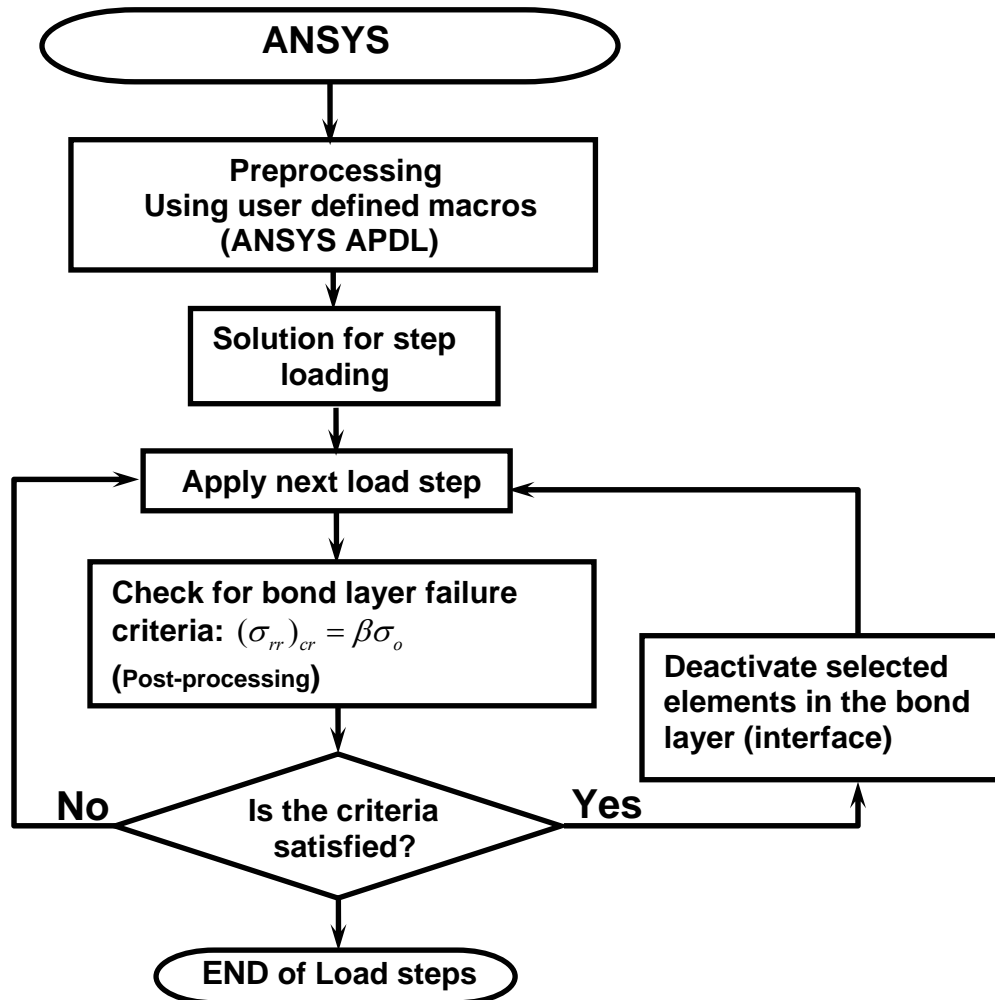


Figure 5.3: Analysis methodology for debond simulation using ANSYS APDL.

As expected the radial stress around the inclusion is continuous before the onset of debonding. The σ_r values are maximum on the interface directly ahead of the crack tip. Once debonding occurs, σ_r values vanish over the debonded interface which terminate where stress discontinuity is seen. That is the debond tips are at $\theta' = 0^\circ$ and $\sim 100^\circ$ in Fig. 5.2.

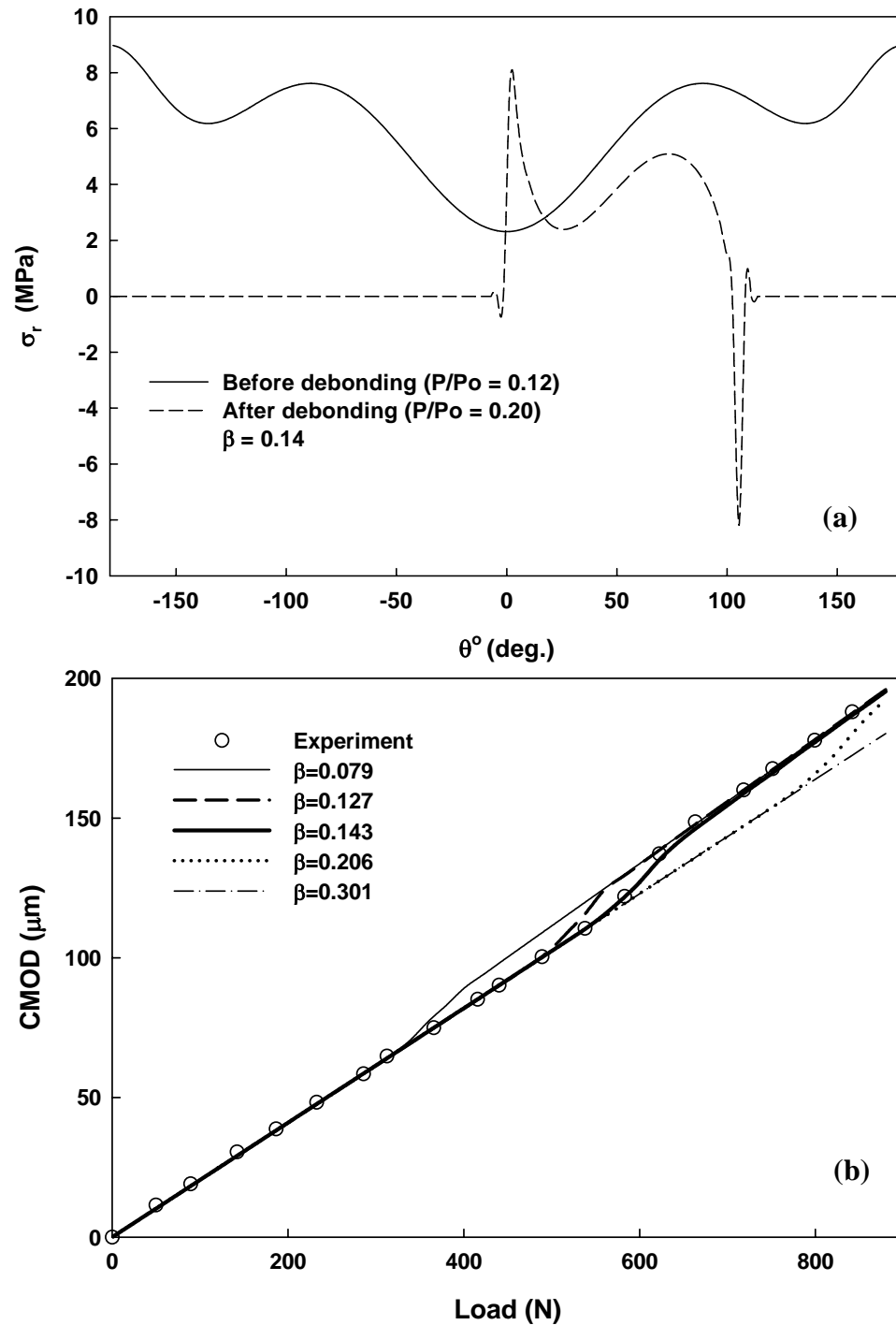


Figure 5.4: (a) Variation of radial stress variation around the inclusion for $b = 0.12$ (applied load P is normalized by P_o , the load corresponding to tensile failure of an uncracked neat epoxy beam). (b) CMOD variation for various β values (eq. (5.1)) used in finite element simulations and comparison with experimental results. ($L/d = 1.31$, $d = 4$ mm)

5.3 Effect of β on debonding

Figure 5.4(a) shows the variation of radial stress along the bond layer before and well after the occurrence of debonding. After an element meets the debond criteria its strain and hence stress are set to zero. Various values of β were considered for simulating debonding. A plot of CMOD as a function of applied load for various values of β in eq. (5.1) is shown in Fig. 5.4(b). Each plot shows a linear variation of CMOD with load until the onset of debonding. Post-debonding regimes have noticeably different slopes when compared to pre-debonding ones. A transition zone in between the two can also be identified. On the same plot, experimentally obtained CMOD values from moiré interferometry are also shown. A value of $\beta = 0.14$ in eq. (5.1) resulted in a good agreement with experimental observations. A lower or a higher value of β relative to this

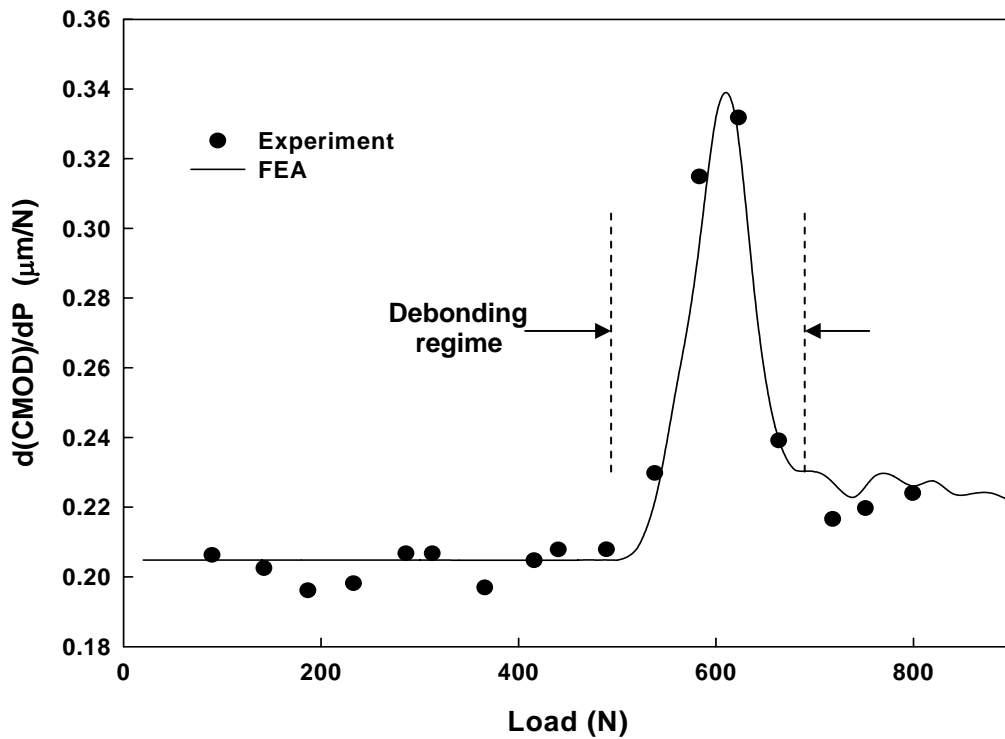


Figure 5.5: Crack mouth compliance comparison between experimental and FEA data.

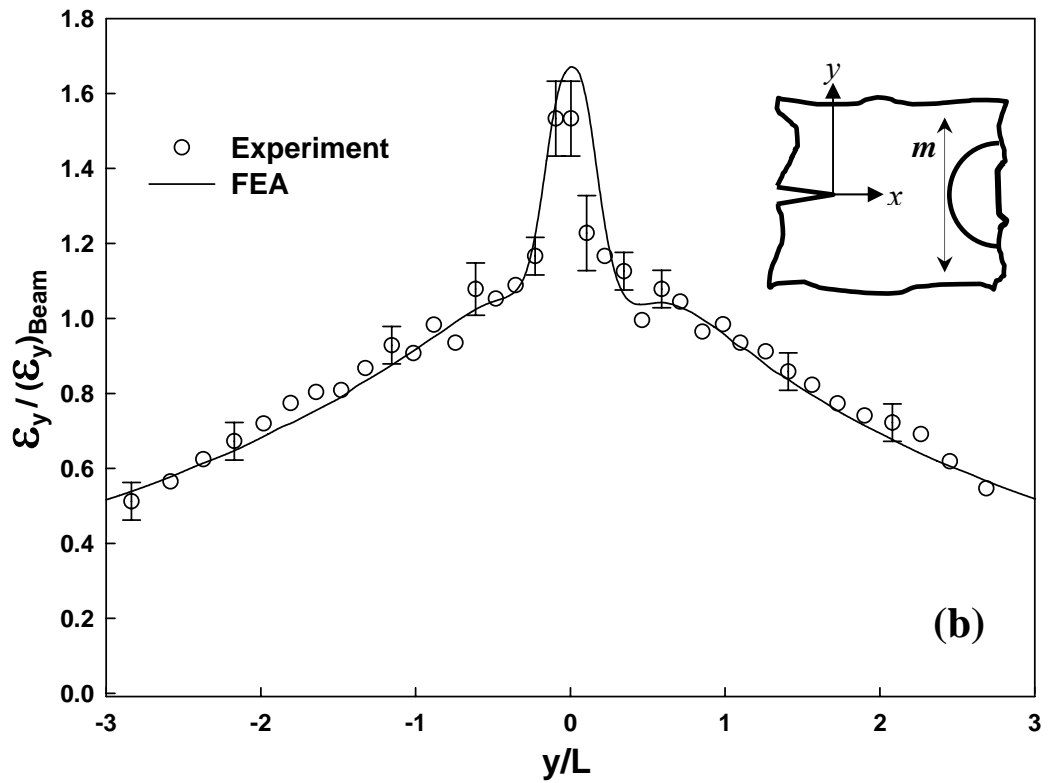
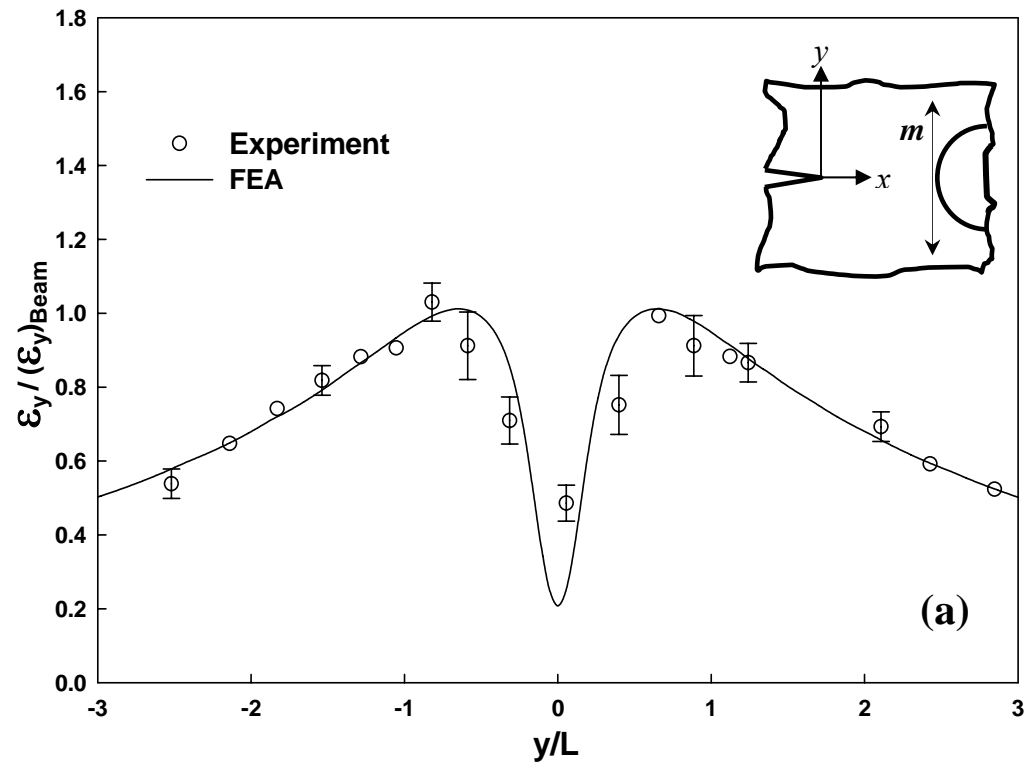


Figure 5.6: Strain field evolution along ($x \sim 3$ mm, y) (shown by line 'm') for (a) pre-debonding and (b) post-debonding stages.

value results in initiation of debonding at lower or higher loads, respectively, as expected. Evidently, following debonding, all graphs coincide with each other.

Next crack mouth compliance ($d(CMOD)/dP$) was calculated by differentiating CMOD data obtained from FE simulation. A central difference scheme was used to compute compliance and the result is shown in Fig. 5.5 indicated by a solid line. On the same plot the experimentally observed crack mouth compliance values are also shown. An excellent agreement between the finite element model and experimental data is readily evident from this graph. A sudden increase in compliance occurs following the onset of debonding. A relatively higher plateau in compliance values in the post-debonding regime compared to the ones from pre-debonding regime can be readily observed.

Next strain evolution along a line ($x/L \sim 0.6, y/L$) (shown by 'm' in Fig. 5.6) near the inclusion-matrix interface from the finite element model are discussed. The strains in Fig. 5.6 are normalized with respect to maximum beam strains, as described in Chapter 3 and the plots are shown for pre- and post-debonding regimes in Figs. 5.6(a) and (b) respectively. The experimental data (from Chapter 4 (Fig. 4.7)) is also shown on the same plot for comparison. The strain values from FEA model are in good agreement with experimental data and these strain plots show a behavior similar to the one observed in experiments. The difference between experimental and finite element strain values closer to the inclusion-matrix interface is not completely unexpected considering the asymmetries entering the model (see Fig. 5.4(a)) after the occurrence of inclusion-matrix

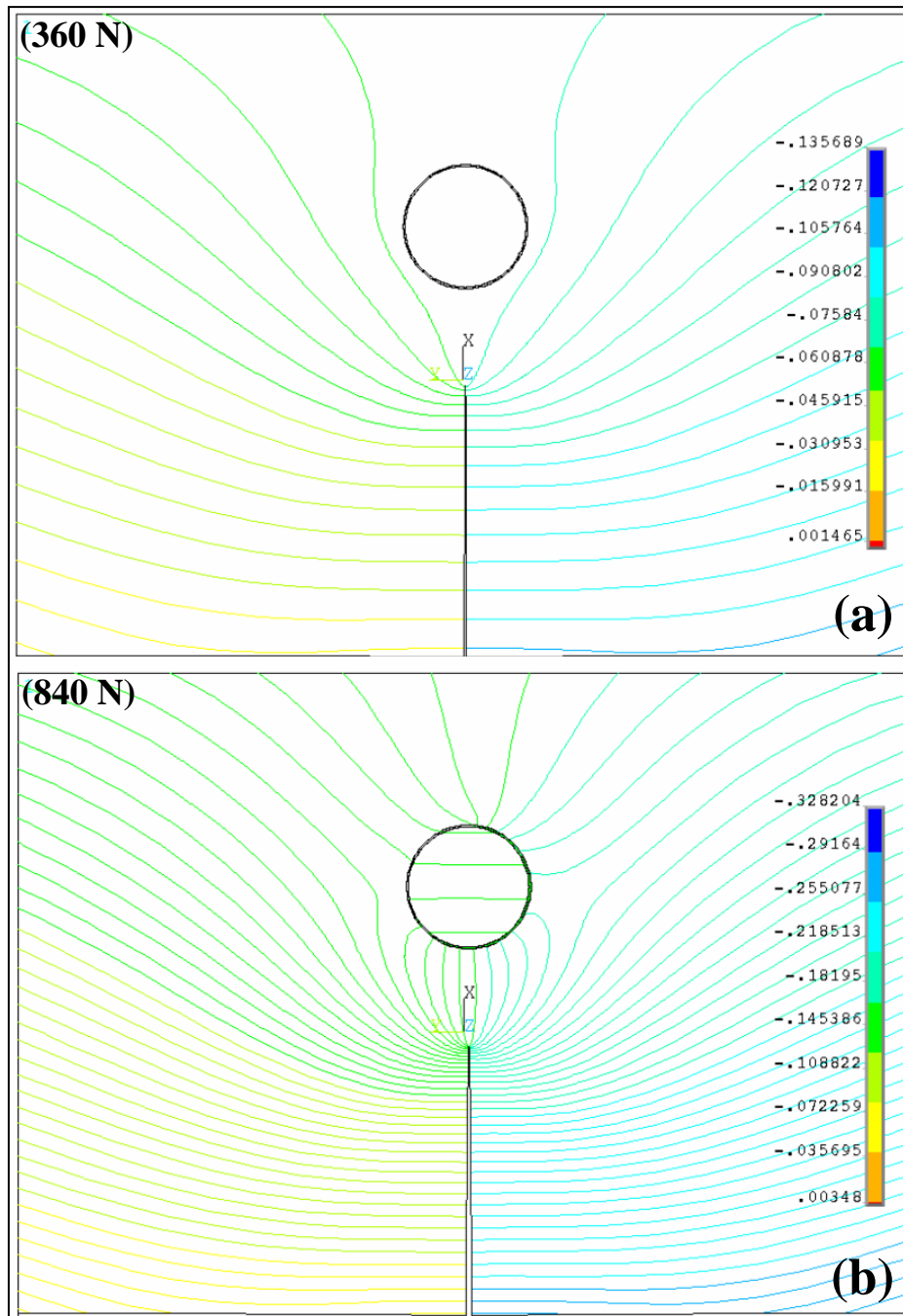


Figure 5.7: Crack opening displacement field from finite element analysis showing perturbed displacement contours in the crack-inclusion vicinity. (a) Before debonding (b) After debonding. Contours levels are approximately same as the experimental ones. ($a = 8.5$ mm, $d = 4$ mm, $L/d = 1.31$, $\beta = 0.14$).

debonding. Further, strain differences are due to possible digitization and differentiation errors as noted earlier.

After the onset of debonding a qualitatively similar progression of the debond front as in experiments was observed in finite element simulations. Also the fringe spacing in the vicinity of crack-inclusion was observed to decrease in post-debonding regime which is evident from the strain plot as a steep increase in Fig. 5.6(b). Representative plots of opening displacement fields from the finite element analysis in

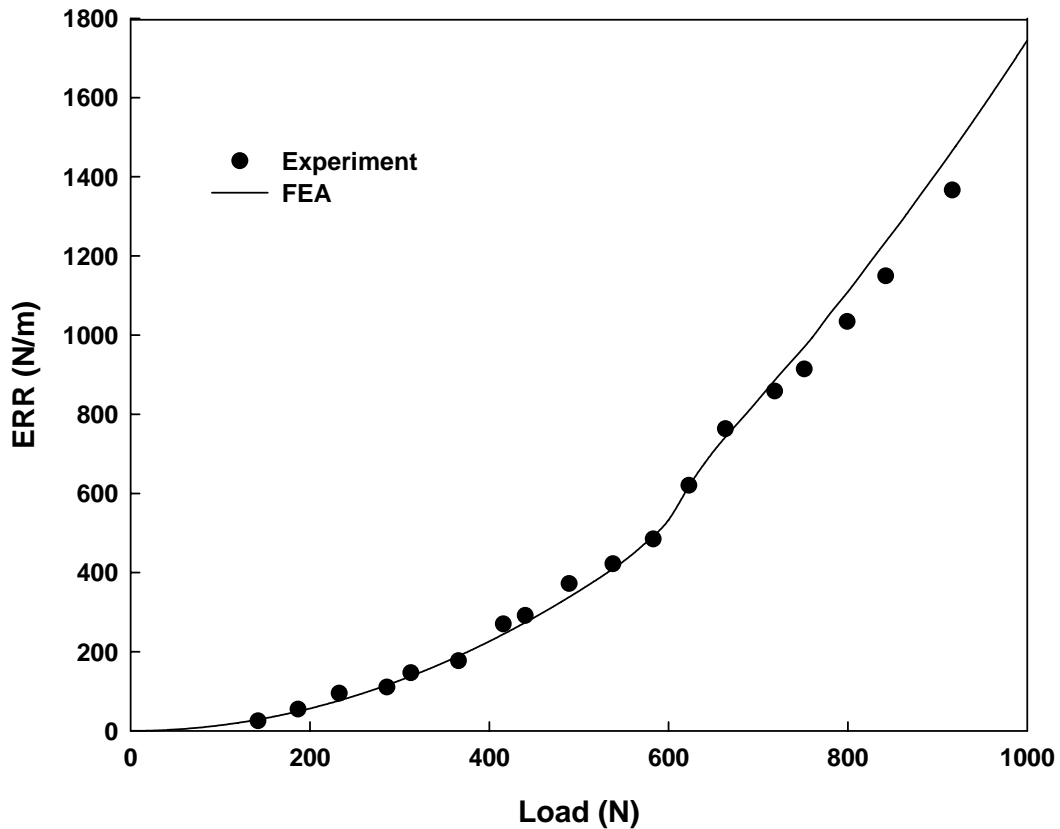


Figure 5.8: Energy release rate variation with applied load.

vicinity the of crack-inclusion pair, before and after debonding, are shown in Fig. 5.7. Here the contour levels are same as the one in moiré interferometry. Qualitative agreement between experimentally recorded opening displacements fields (Figs. 4.2 and

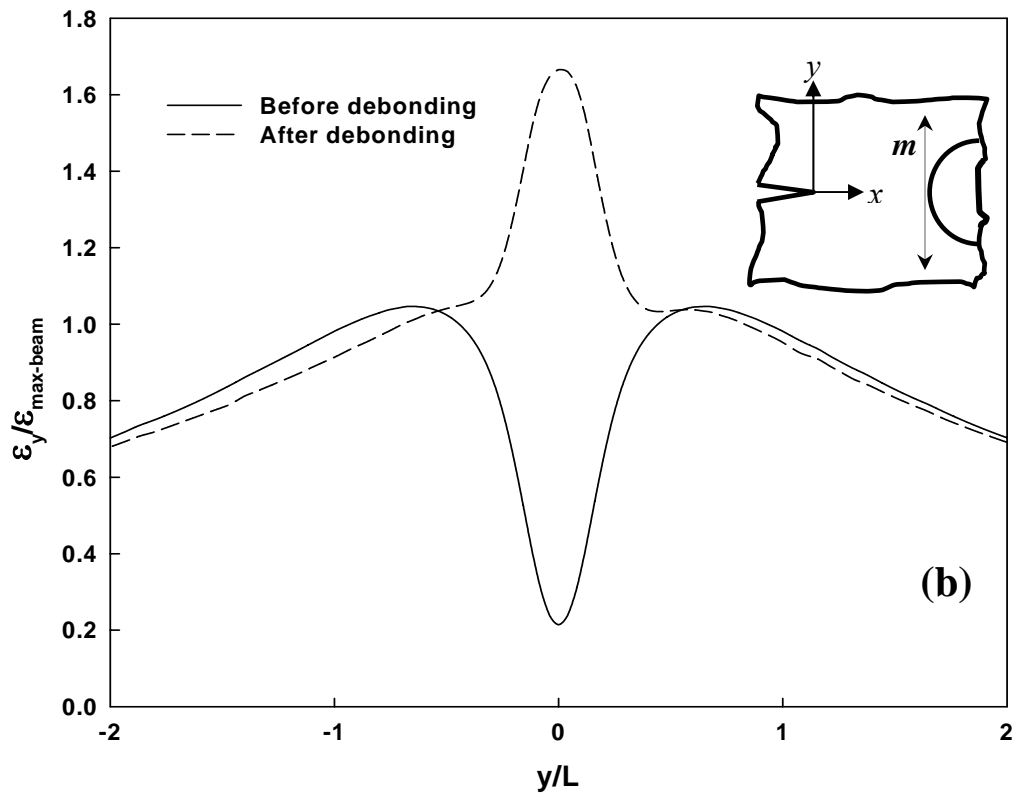
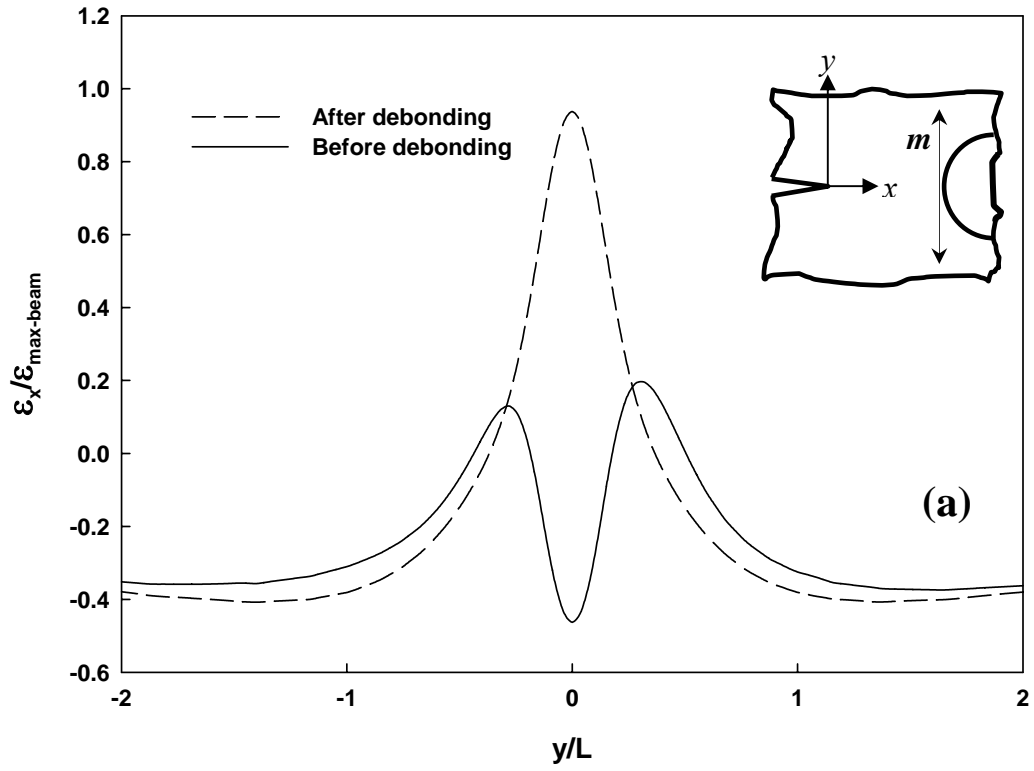


Figure 5.9: Normal Strain evolution along line 'm' (a) ϵ_x (b) ϵ_y .

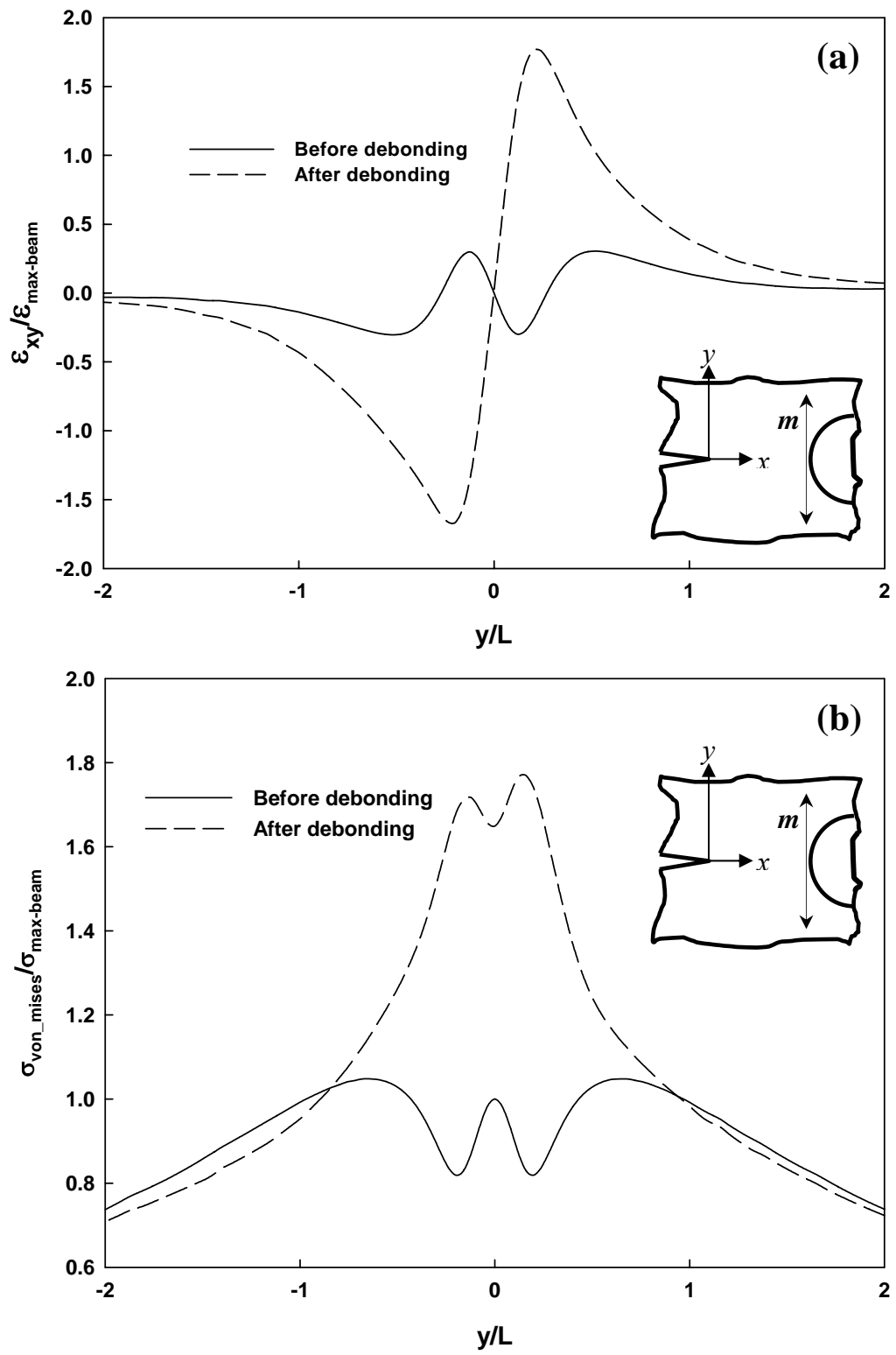


Figure 5.10: Evolution of (a) Shear strain ϵ_{xy} (b) Von-Mises stress along line 'm'.

4.3) and the ones from finite element analysis is readily evident. Discontinuous fringes around the inclusion periphery in the interferograms shown in Figs. 4.2 and 4.3 are also evident in Fig. 5.7. Thus the overall crack tip behavior in terms of crack opening displacements is preserved in these simulations.

A user-defined macro was used to extract mode – I stress intensity factors (K_I) from the finite element model. Linear regression methods using crack opening displacement along $\theta = \pm\pi$, as described in Chapter 3 was used and subsequently Energy Release Rates (ERR) were calculated as,

$$ERR = G = \frac{K_I^2}{E} \quad \text{for plane stress} \quad (5.2)$$

where E is the Young's modulus of the matrix material. A good agreement can be seen between experiments and simulations from the results plotted in Fig. 5.8.

Normal strains (ε_x) and (ε_y) shear strains (ε_{xy}) were also extracted along ($x/L \sim 0.6$, y/L) (shown by line 'm') from the finite element model and are shown in Figs. 5.9 and 5.10(a). (For completeness a plot of normal strain (ε_y) along 'm' is reproduced in Fig. 5.9(b)). All strain components also shows drastic increase in the vicinity of the inclusion after debonding whereas beyond $y/L = \pm 1$ the values are almost unaffected suggesting a highly localized phenomena. Figure 5.10(b) shows a plot of von-Mises stresses along the same line for the pre- and post-debonding regimes.

5.4 Convergence study

To ensure the accuracy of the results a convergence study was performed. As described earlier the model is comprised of a distinct set of elements along the interface

between the matrix and the inclusion and these elements are used for simulating debonding. Numbers of elements in the whole model as well as in the circular interfacial bond layer were varied and simulations were carried out. The number of elements in the bond layer was doubled in subsequent simulations in steps of 32, 64 and 128. CMOD values were extracted from these simulations and the results are shown in Fig. 5.11. It

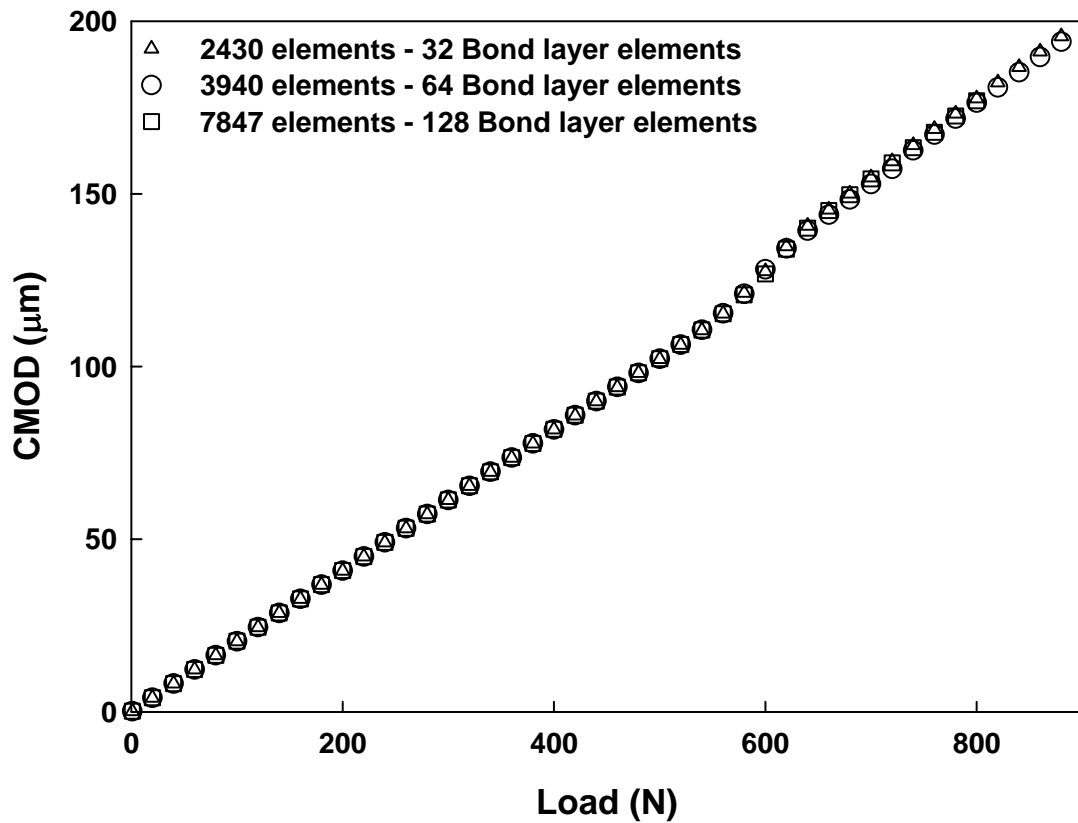


Figure 5.11: Validation of CMOD with load for different bond layer element sizes.

can be seen from the plot that a good convergence is achieved and mesh is sufficiently refined. Thus the numerical model seems to capture the overall behavior of the crack-inclusion interaction problem including evolution of inclusion-matrix debonding.

5.5 Parametric study

5.5.1 Constant L/d ratio: Effect of inclusion size

A parametric study was carried out for different L/d ratios using the finite element model for the edge cracked geometry loaded in symmetric three-point bend configuration. In all simulations $\beta = 0.14$ for which good agreement between experiments and simulations were observed is used. The effect of inclusion size was studied for a constant L/d ratio with respective L and d values shown in Table 5.1. Here L is the distance between the crack tip and inclusion center and d is the diameter of the inclusion. A bonding layer thickness (t_b) of $d/100$ was used in each of these simulations. The model parameters used for these are listed in Table 5.1.

The plot of variation of CMOD with applied load is shown in Fig. 5.12 for a constant L/d ratio of 1.31 with different diameters of inclusions. The applied load in these plots is normalized by P_o , the load at which a neat epoxy beam would fail in tension based on ultimate strength of epoxy (σ_o). P_o is calculated by using equation,

$$P_o = \frac{2\sigma_o BW^2}{3S} \quad (5.3)$$

where B is the thickness, W is the height of the beam and S is span. The value of P_o was thus calculated as (4241 N) as failure load of an uncracked neat epoxy beam. For these simulations parameter L was varied with respect to the inclusion diameter d to achieve a constant L/d ratio. A delayed debonding was observed for larger inclusions whereas smaller inclusions get debonded from the matrix at much lower loads, as seen from plot in Fig 5.12. This can be visualized better from the crack mouth compliance ($d(CMOD)/dP$) calculated by differencing CMOD values with respect to the applied load,

#	L (mm)	d (mm)	L/d	t_b (mm)
1	0.655	0.5	1.31	0.006
2	1.31	1	1.31	0.01
3	2.62	2	1.31	0.02
4	5	3.8	1.31	0.05
5	6.55	5	1.31	0.05
6	7.86	6	1.31	0.06
7	9.17	7	1.31	0.07
8	10.48	8	1.31	0.08

Table 5.1: Geometric parameters used for study with a constant L/d ratio.

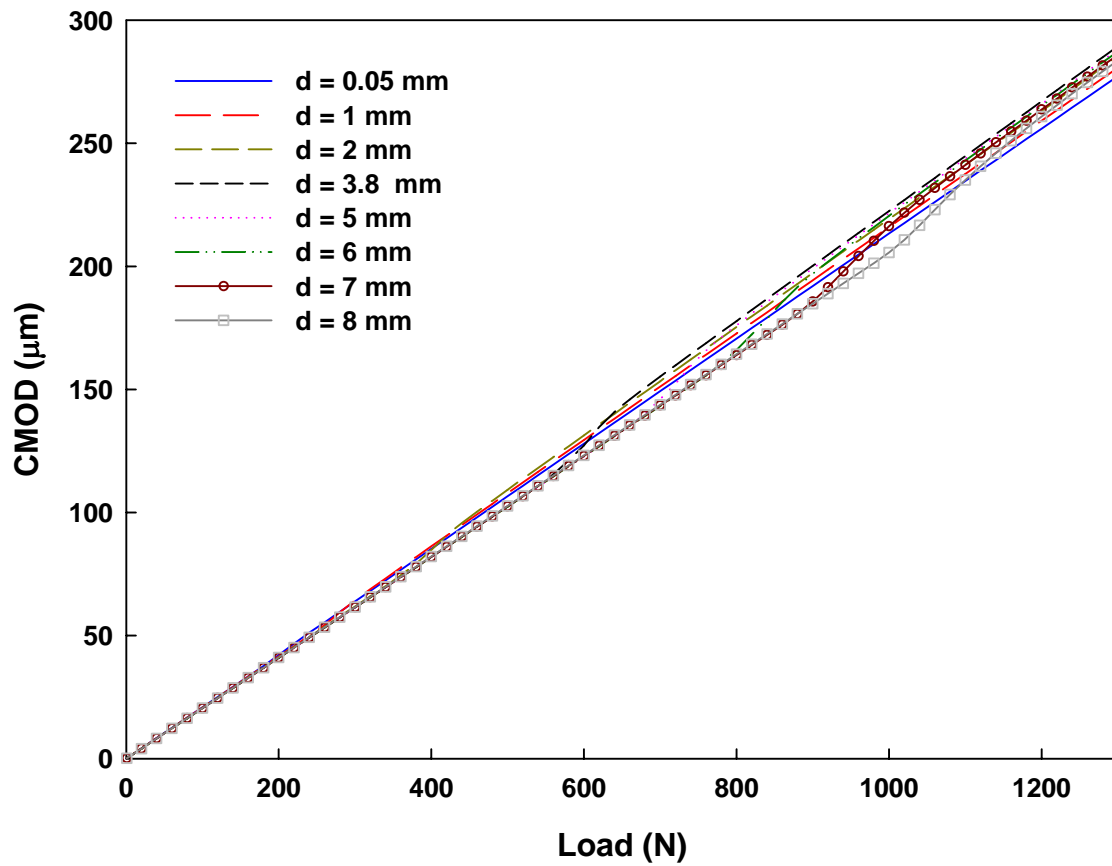


Figure 5.12: CMOD variation with load for L/d ratio of 1.31.

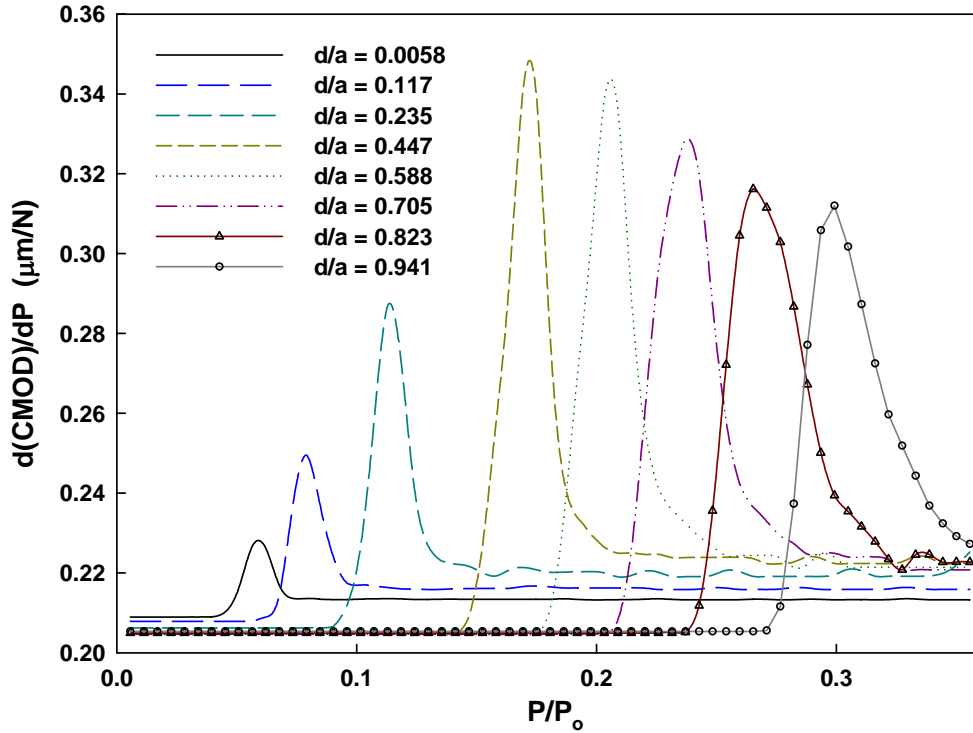


Figure 5.13: Variation of crack mouth compliance with respect to applied load. ($L/d=1.31$)

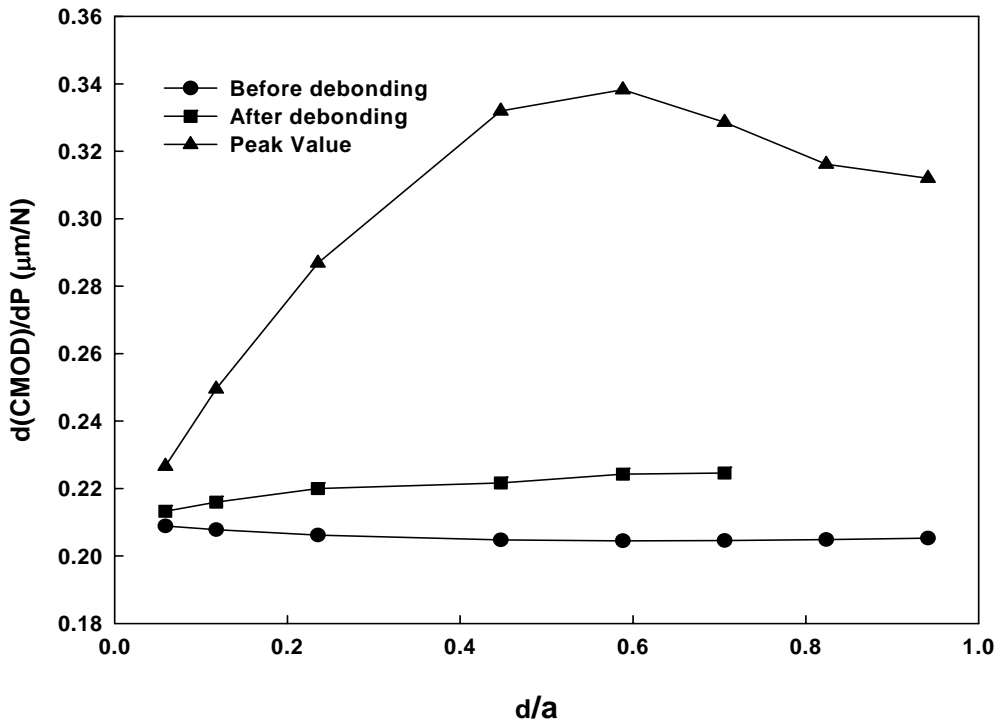


Figure 5.14: Crack mouth compliance values for different inclusion diameters ($L/d = 1.31$).

and are shown in Figure 5.13. Each compliance plot shows different steady state values before and after debonding. In this context it is worth noting that crack mouth compliance for a cracked neat (without any inclusion) epoxy beam is $0.21 \mu\text{m}/\text{N}$. At the onset of debonding compliance shows a jump and attains distinctly different maximum value in each case. The compliance values before debonding, after debonding as well as the maxima during the loading phase are shown in Fig. 5.14. Maximum values increase until a d/a value of 0.6 but drop with further increase in d/a . Though the physical

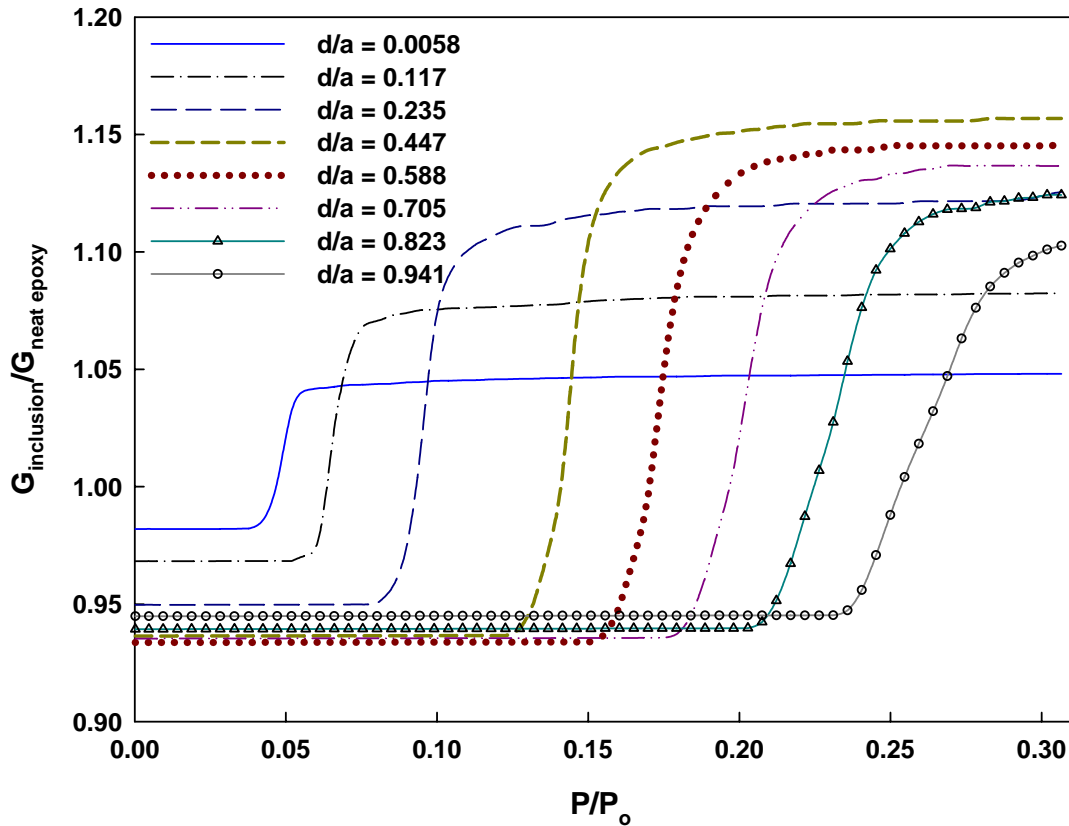


Figure 5.15: Energy release rates for different diameter inclusions ($L/d = 1.31$).

significance of these maximum values is unclear at the moment, further investigation would likely shed more light on the issue.

Normalized energy release rates (ERR) were also calculated from the simulations as described by eq. 5.2 and corresponding plots of the same is shown in Fig. 5.14. A behavior similar to the one observed from crack mouth compliance values is observed. The normalization was done with respect to the energy release rates associated with a same geometry (edge cracked three-point bend) neat epoxy specimen at the same load level ($G_{neat\ epoxy}$) calculated as,

$$G_{neat\ epoxy} = \frac{(K_I)_{neat\ epoxy}^2}{E} \quad (5.4)$$

Opening strains (ε_y) were extracted from these simulations involving a constant L/d ratio of 1.31. Figures 5.16(a) and (b) show the plots of normalized ε_y in pre- and post-debonding regimes respectively. A normalized load of $P/P_o = 0.023$ is considered for the pre-debonding regime plots which corresponds to a load level well before debonding. For post-debonding regime the normalized load value is $P/P_o = 0.30$ which corresponds to a load level after debonding. Here P_o (= 4241 N) is the load value corresponding to failure of a homogeneous uncracked beam based on failure strength of matrix (epoxy) material. The increasing shielding effect is evident here in the pre-debonding regime (Fig. 5.16(a)) as inclusion size increases from lower values of strains near matrix-inclusion interface for larger size inclusions. In post-debonding regime also the same trend is observed for larger size inclusions as seen from Fig. 5.16(b).

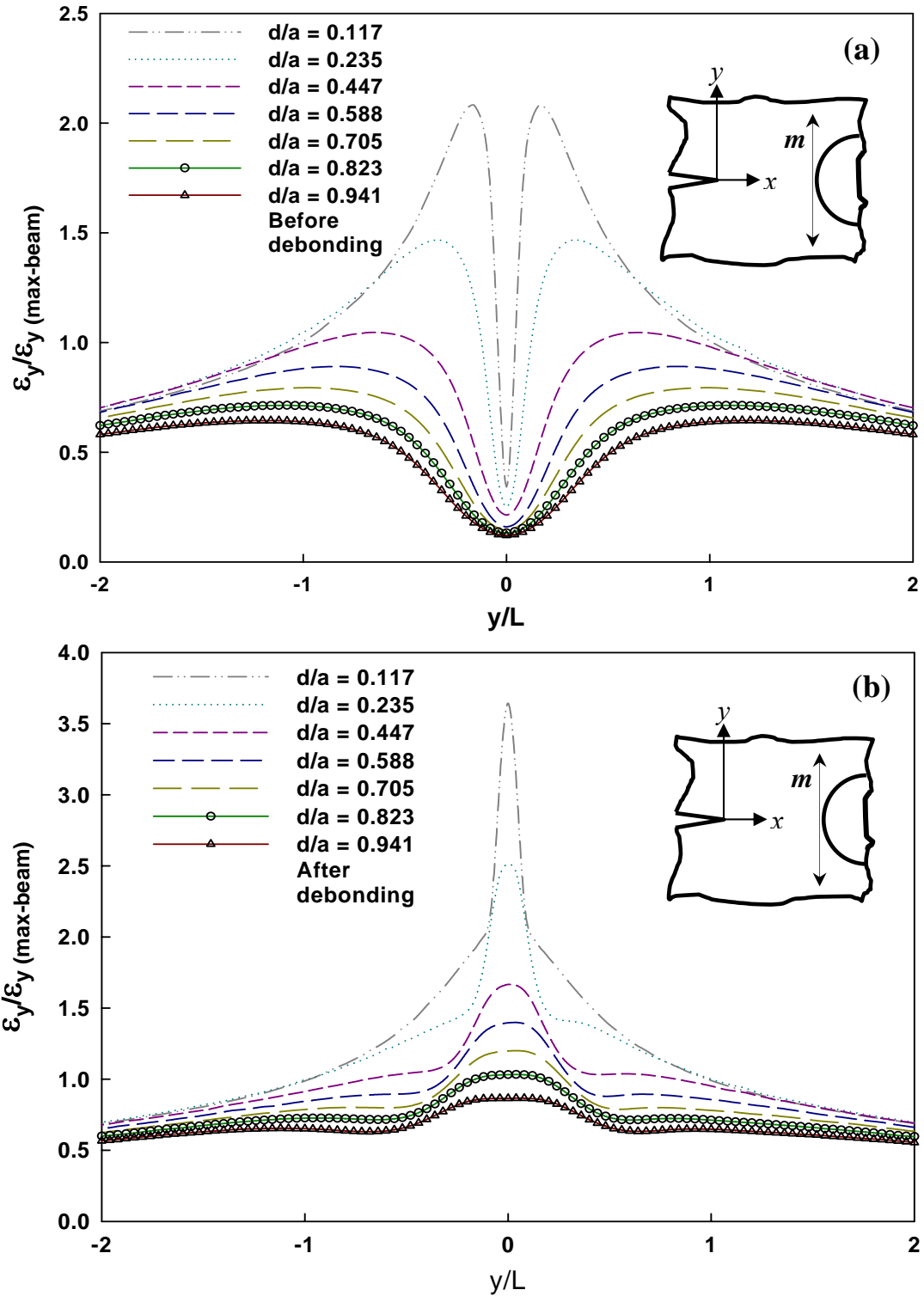


Figure 5.16: Strain (ϵ_y) evolution along line 'm' for $L/d=1.31$ (a) Before debonding ($P/P_0 = 0.023$) (b) After debonding ($P/P_0 = 0.30$). (Note: $a = 8.5$ mm.)

5.5.2 Varying L/d ratio: Crack-inclusion proximity effect

Next, the L/d ratio was varied to examine the effect of inclusion proximity with the crack tip and its impact on overall behavior of the problem. In this case inclusion size (d) was varied whereas the distance between the crack tip and inclusion center L was kept

#	L (mm)	d (mm)	L/d	t_b (mm)
1	5	1	5	0.01
2	5	2	2.5	0.02
3	5	3.8	1.25	0.04
4	5	5	1	0.05
5	5	6	0.83	0.06
6	5	7	0.71	0.07
7	5	8	0.63	0.08

Table 5.2: Geometric parameters used for studying effect of L/d ratio.

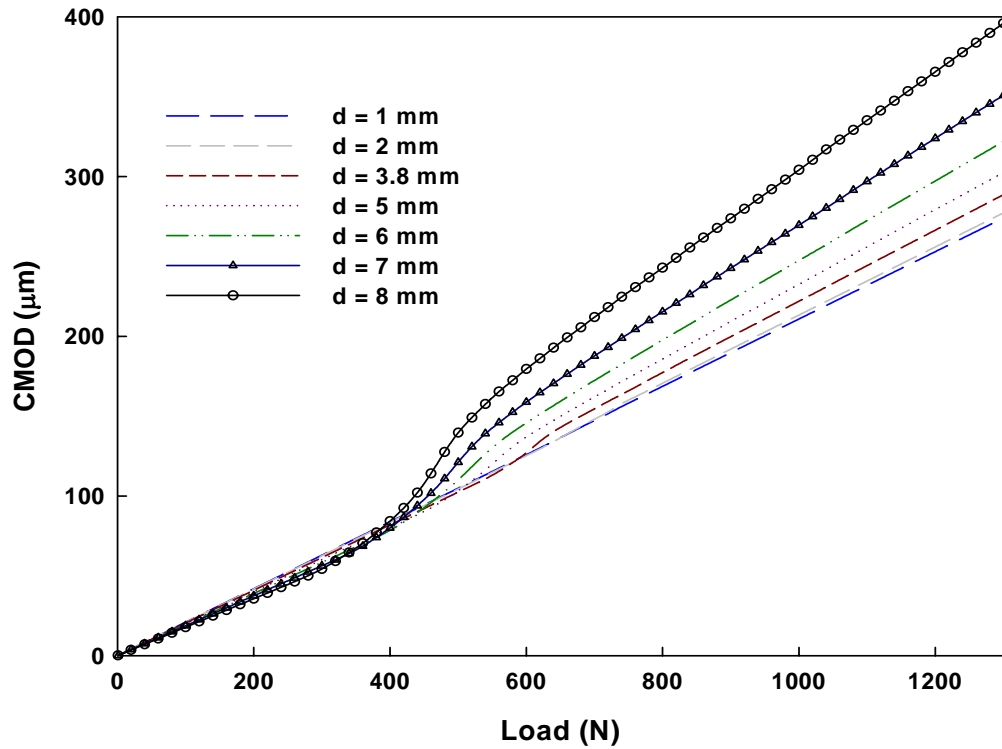


Figure 5.17: Variation of crack mouth opening displacement with the applied load.

constant. The values of parameters L and d used in this set of simulations are tabulated in Table 5.2.

The CMOD values for this study are shown in Fig. 5.17. It can be seen from the plots that as the L/d ratio decreases the debonding occurs much earlier. Also, the CMOD values are lower for higher L/d before debonding whereas after debonding the trend is reversed. The inclusions nearer to the crack-tip show variation of CMOD with noticeably higher slopes. The compliance plots obtained from Fig. 5.17 shown in Fig. 5.18 demonstrate this more distinctly. It can be seen that the compliance values before and after debonding show opposite trends. The peak compliance values attained along with the steady state values before and well after the occurrence of debonding are shown in Fig. 5.19 for various L/d ratios. Peak compliance values show increasing trend as the L/d

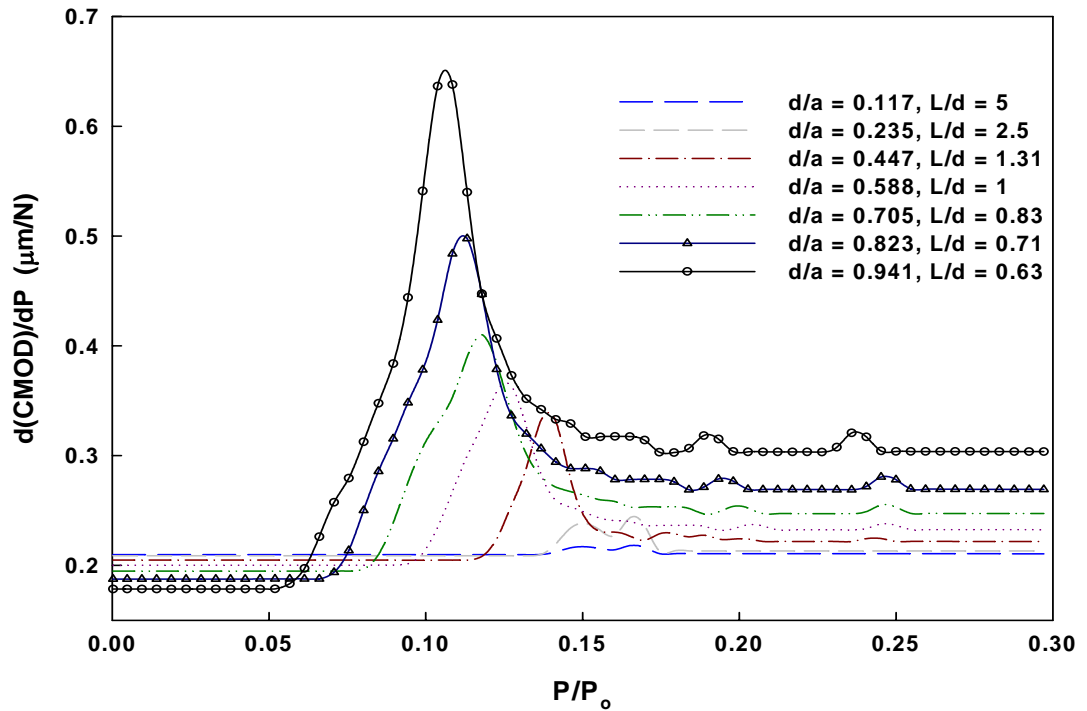


Figure 5.18: Variation of crack mouth compliance with the applied load.

ratio decreases (when the distance between the crack tip and the inclusion center (L) is constant). The values associated pre-debonding regime shows a decreasing trend with decrease in the L/d ratio whereas after debonding the trend is reversed. For this case (L/d varying), normalized energy release rates (or, crack driving force) are shown in Figure 5.20. In each case, shielding effect is evident before the occurrence of debonding as the L/d ratio increases whereas after debonding the energy release rates shows steep increase and settles at a higher value for larger L/d ratios. From $L/d = 5$ to $L/d = 0.625$ the normalized value of energy release rate is increased approximately 2.5 times as evident from the plot. That is, an inclusion which is much closer to the crack tip

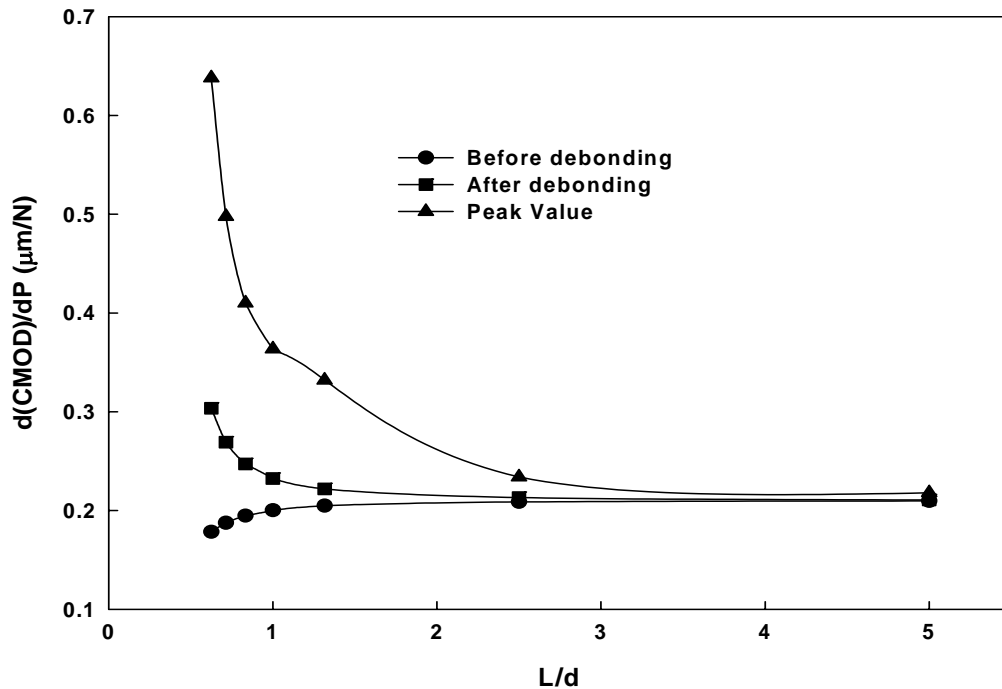


Figure 5.19: Steady state and maximum values of crack mouth compliance with variation of L/d ratio.

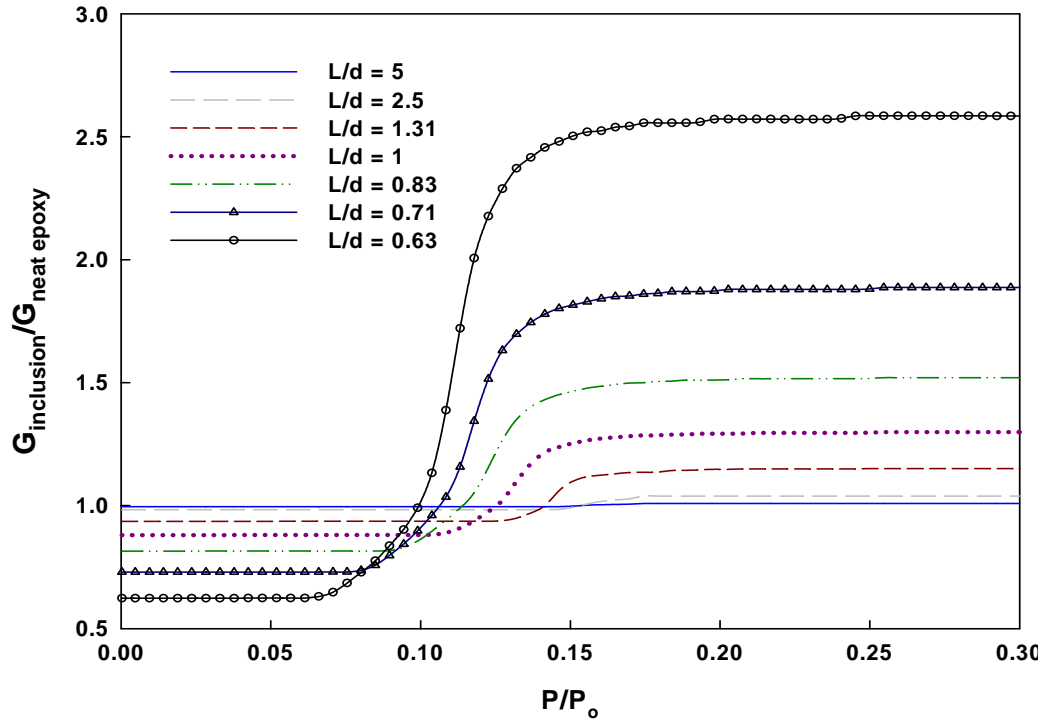


Figure 5.20: Energy release rates for different L/d ratios.

when debonds increases the crack driving force (by a factor of ~ 2.5 in this study) as well as crack mouth compliance when compared to the one farther away.

For the case of varying L/d ratio the opening strains (ε_y) were extracted and the corresponding plots of strains along line ‘ m ’ are shown in Figs. 5.21(a) and 5.21(b). The corresponding load levels for each of these plots are kept same as Figs. 5.16(a) and (b) respectively. As L/d ratio increases ε_y values shows increasing trend in the vicinity of the inclusion-matrix interface in the pre-debonding regime (Fig. 5.21(a)). Figure 5.21(a) shows a slight decrease in ε_y values for L/d ratio larger than 0.71. Whereas ε_y values show a monotonic increase in the post debonding regime with increase in the L/d ratio as seen from Fig. 5.21(b).

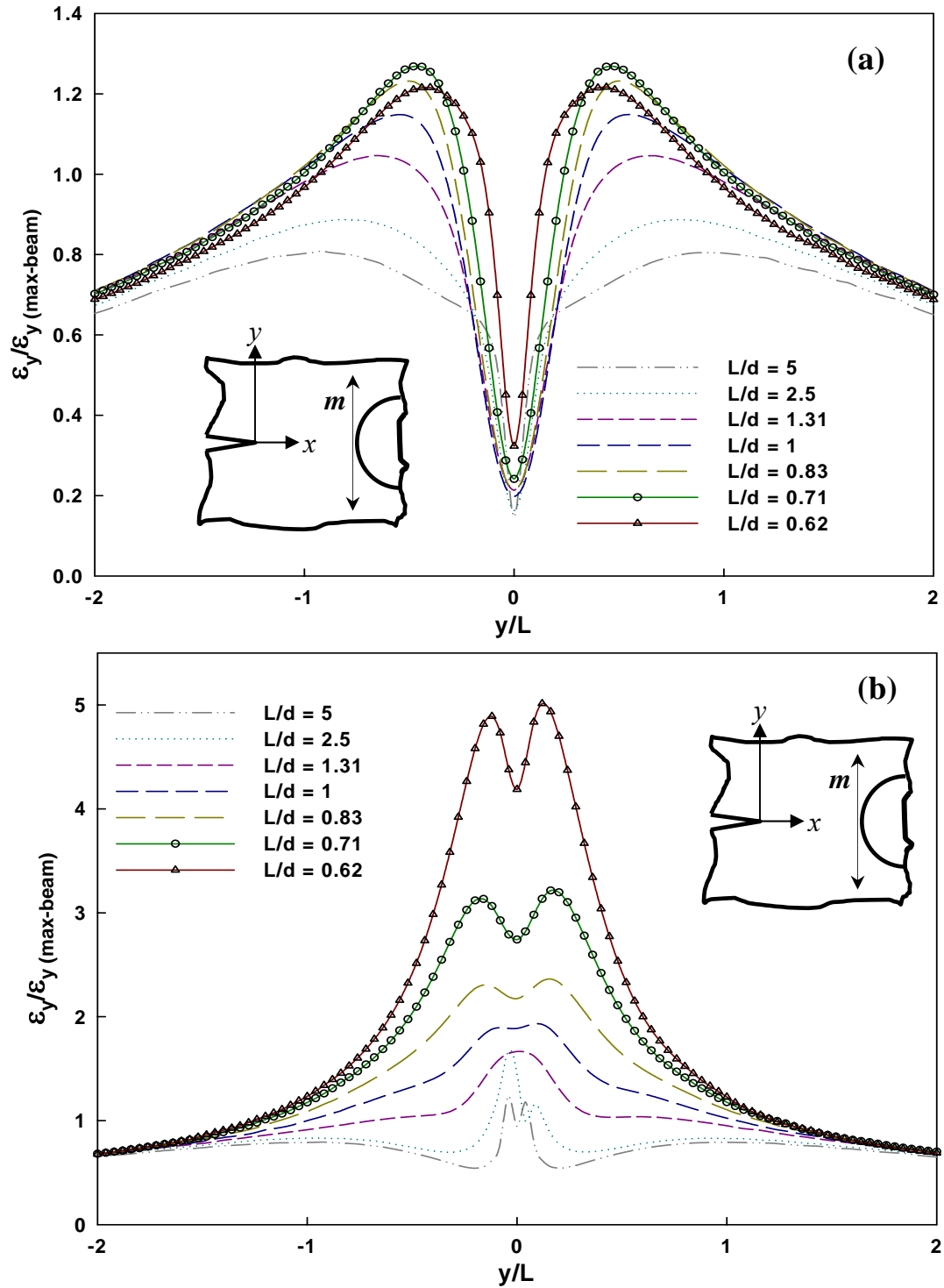


Figure 5.21: Strain (ε_y) evolution along line 'm' for $L = 5$ mm. (a) Before debonding ($P/P_o = 0.023$) (b) After debonding ($P/P_o = 0.30$).

5.6 Estimation of glass-epoxy interface strength

To provide a physical interpretation for the value of $\beta = 0.14$ in eq. (5.1) that provided good agreement with experimental CMOD variation, nominal interfacial strength between epoxy and glass was measured. This was done using T-shaped tension specimens shown schematically in Fig. 5.22. Clean surface of a rectangular glass bar (75mm x 25mm x 6.6mm) that has the surface finish same as that of the glass inclusion was treated with silane and dried at room temperature for 24 hours. Silicone rubber molds were prepared to cast epoxy (70mm x 21mm x 7.1mm) stems on the glass surface. Silicone rubber

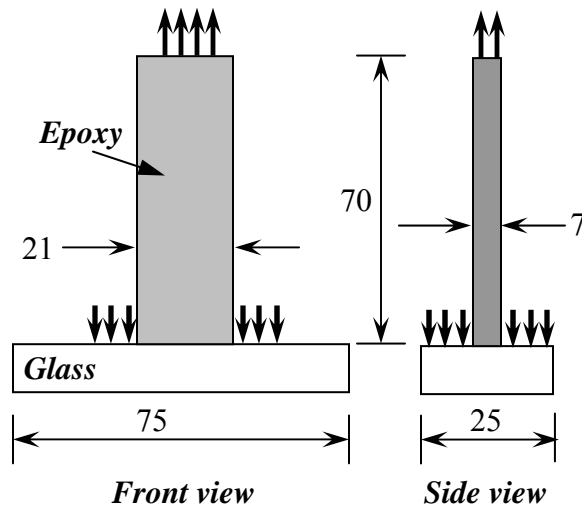


Figure 5.22: Schematic of specimens and loading configuration used for estimating glass-epoxy bond strength. (Note: All dimensions are in mm.)

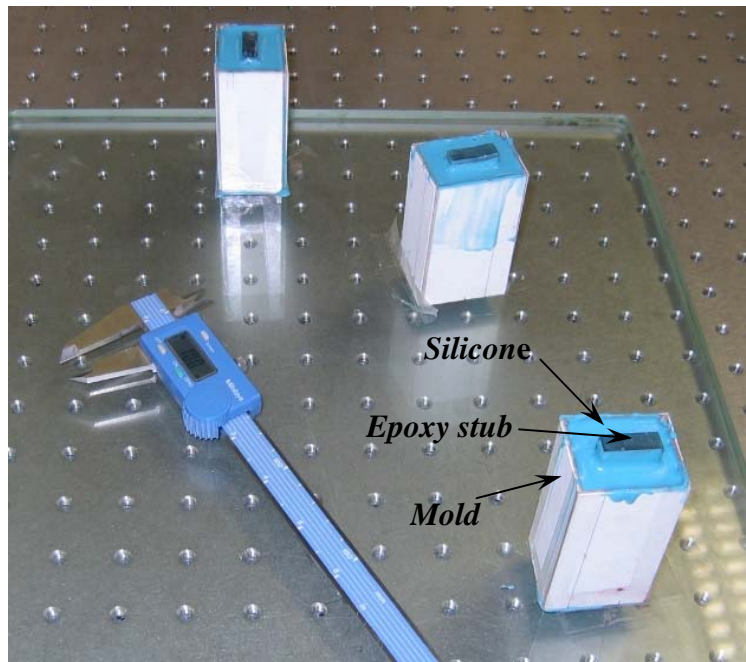


Figure 5.23: Silicone rubber molds cast on a flat surface.

Silicone molds thus prepared are shown in Fig 5.23. These molds were separated from the casting surface after they were cured and the epoxy bar used to cast the mold was pulled out. After proper alignment of the mold over the treated glass surface liquid epoxy was again poured into the mold and allowed to cure for 72 hours at room temperature. Casting epoxy in this way allowed preparing bond between epoxy and glass in a manner similar to the one that exists between the inclusion surface and the matrix in crack-inclusion specimens. The specimens were tested in an INSTRON 4465 testing machine and load data were collected until glass-epoxy interface failed. A photograph of the test setup is shown in Fig. 5.24. Brittle failures of the glass-epoxy interfaces were observed and average failure stresses for several samples tested are reported in Table – 5.3.

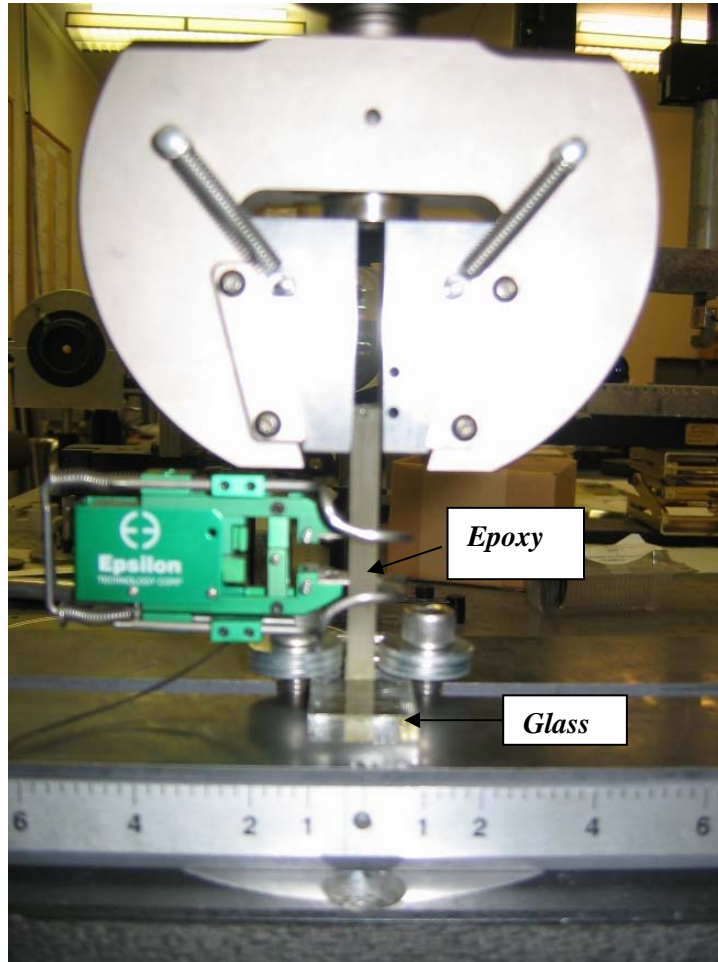


Figure 5.24: Experimental setup for glass-epoxy interfacial strength measurement.

Specimen #	Failure stress (MPa)
1	7.46
2	10.39
3	9.90
Average interfacial failure strength = 9.25 MPa	

Table 5.3: Glass-epoxy interfacial failure strength data.

The average value of the interface strength was estimated as 9 ± 1 MPa. Interestingly, $(\sigma_{rr})_{cr}$ value in eq. (7) that produced good agreement ($=\beta\sigma_o$) with moiré data is within 5% of the interfacial strength between epoxy and glass. This further validates the proposed model used in the FE simulations.

It should also be noted that a few experiments on T-specimens prepared without silane treatment were carried out. The resulting weaker interface showed an average interfacial strength of 3 ± 1 MPa, nearly a third of the one when glass was treated with silane.

CHAPTER 6

CONCLUSIONS

In this work a stationary crack interacting with a relatively stiff inclusion and the resulting debonding of the inclusion from the matrix were studied experimentally and numerically. Three-point bend (TPB) epoxy specimens with edge cracks and solid cylindrical glass inclusion were examined. The full-field technique of moiré interferometry was used to map deformations in the crack-inclusion vicinity. The experimental novelty here includes development of microelectronics fabrication based methods for printing specimen gratings using two approaches namely, (1) Direct transfer of aluminum coated gratings from a silicon wafer master and (2) Indirect transfer of gratings using silicone rubber submasters. High quality grating profiles were achieved using these two methods. A moiré interferometer was developed and used to acquire high quality interferograms. An optical resolution of 1.25 μm /half-fringe was successfully achieved and results were benchmarked using a cracked TPB specimen made of neat epoxy.

Next, crack-inclusion specimens were fabricated and deformations were mapped near crack-inclusion vicinity during monotonically increasing load. The occurrence of debonding between the matrix and the inclusion was successfully identified during the loading phase. Pre- and post-debond deformation fields show localized differences ahead

of the crack tip and near the inclusion. The fringe contours clearly show discontinuity at the matrix-inclusion interface and observable asymmetry in displacements around the inclusion due to selective propagation of the debond front. A change in the crack mouth compliance was clearly evident at the onset of debonding. Substantial differences in terms of dominant strains obtained by differentiating the optical data were also evident when pre- and post-debond stages were compared. Opening strain values showed noticeable increase in the vicinity of the crack tip and the inclusion near to inclusion-matrix interface after debonding whereas far field strains remain relatively unaffected.

A finite element model was developed to capture the major experimental observations. This was achieved by implementing a inclusion-matrix debond criteria based on an interfacial layer of elements attaining a fraction of the ultimate strength of the epoxy matrix. The debonding process was simulated by deactivating stiffness of interfacial layer of elements by a user-defined macro in ANSYS structural analysis environment. Various bond strengths were used as a fraction of the ultimate strength of the matrix material and the finite element model was validated against the experimental data. The displacement and strain fields were compared successfully with experimental results. A follow up experiment to measure apparent interfacial strength of glass-epoxy suggested that inclusion debonded when radial stress at a location on the interface reached the interfacial strength of the interface.

A parametric study was undertaken using the finite element model. Mainly two different scenarios were studied: (1) Inclusion size effect (constant L/d ratio) and (2) Inclusion proximity effect (varying L/d ratio). Fracture parameters such as crack mouth opening displacement (CMOD) and energy release rates were calculated using the finite

element model. At a constant L/d ratio the larger size inclusions show delayed debonding. Also the peak value of crack mouth compliance attained during debonding was observed to increase until a d/a ratio of approximately 0.58 whereas further increase showed a decreasing trend. The study of varying L/d ratio (with constant L) showed that a larger inclusion shields the crack tip more before debonding. However, a larger inclusion debonds at a lower load and results in higher crack mouth compliance than the smaller size inclusion upon debonding. Energy release rate for a larger inclusion ($L/d = 0.63$) showed a higher value (~ 2.5 times) than smaller ($L/d = 5$) inclusion at a fixed value of L ($= 5$ mm) in post-debonding regime in this study.

BIBLIOGRAPHY

1. Jones R. M., Mechanics of composite materials, Second edition, Taylor and Francis, Inc., 1999. (ISBN: 1-56032-712-X)
2. Marple B. S. and Boulanger J., Graded casting of materials with continuous gradients, Journal of American Ceramic Society., **77**(10), pp.2747, 1994.
3. Fukui Y., Takashima K. and Ponton C. B., Measurement of Young's modulus and internal friction of an in-situ Al-Al₃Ni functionally gradient material, Journal of Materials Science, **29**, pp.2281, 1994.
4. Abboud J. H., Rawlings R. D. and West D. R. F., Functionally graded nickel-aluminide and iron-aluminide coatings produced via laser cladding, Material Science and Technology., **10**, pp.414, 1994.
5. Sampath S., Gausert R. and Herman H., Plasma-spray forming ceramics and layered composites, Journal of Metals. **47**, pp.30, 1995.
6. Butcher R. J., Rousseau C. -E., Tippur H. V., A functionally graded particulate composite: Preparation, measurements and failure analysis, Acta Materilia, **47**(1), pp.259-268, 1999.
7. Rousseau C. -E., Tippur H. V., Compositionally graded materials with cracks normal to the elastic gradient. , Acta Materilia, **48**, pp.4021-4033, 2000.
8. Kirugulige M. S., Kitey R., Tippur H. V., Dynamic fracture behavior of model sandwich structures with functionally graded core: a feasibility study, Composite Science and Technology., **65**, pp.1052-1068, 2005.
9. Tamate O., "The effect of a circular Inclusion on the stress around a line crack in a sheet under tension," International Journal of Fracture Mechanics., **4**, pp.275-266, 1968.
10. Atkinson C., "The interaction between a crack and an inclusion," International Journal of Engineering Sciences, **10**, pp.127-136, 1972.

11. Erdogan F., Gupta G. D. and Ratwani M., "Interaction between a circular inclusion and an arbitrarily oriented crack," *Journal of Applied Mechanics*, **41**, pp.1007-1013, 1974.
12. Gduotos E.E., Interaction effects between a crack and a circular inclusion, *Fibre Science and Technology*, **15**(1), pp.27-40, 1981.
13. Gduotos E.E., Stable Crack Growth of a Crack Interacting with a Circular Inclusion, *Theoretical and Applied Fracture Mechanics*, **3**(2), pp.141-150, 1985.
14. Kunin I., Gommerstadt B., On Elastic Crack-Inclusion Interaction, *International Journal of Solids and Structures*, **21**(7), pp.757-766, 1985.
15. Hasebe N., Okumura M., Nakumura T., Stress-Analysis of a debonding and a crack Around a Circular Rigid Inclusion, *International Journal of Fracture.*, **32**(3), pp.169-183, Nov 1986.
16. Patton E. M., Santare M. H., The effect of a rigid elliptical inclusion on a straight crack, *International Journal of Fracture*, **46**, pp.71-79, 1990.
17. Li R. and Chudnovsky A., Energy analysis of crack interaction with an elastic inclusion, *International Journal of Fracture*, **63**, pp.247-261, 1993.
18. Li R., and Chudnovsky A., The stress intensity factor Green's function for a crack interacting with a circular inclusion, *International Journal of Fracture*, **67**, pp.169-177, 1994.
19. Bush M., The interaction between a crack and a particle cluster, *International Journal of Fracture*, **88**, pp.215-232, 1997.
20. Knight M. G., Wrobel L. C., Henshall J. L., De Lacerda L. A., A study of the interaction between a propagating crack and an uncoated/coated elastic inclusion using BE technique, *International Journal of Fracture.*, **114**, pp.47-61, 2002.
21. Kitey R., Phan A. V. Tippur H. V., Kaplan T., Modeling of crack growth through particulate clusters in brittle matrix by symmetric-Galerkin boundary element method, *International Journal of Fracture*, 2005 (Article in press).
22. Kitey R., Microstructural effects on Fracture behavior of particulate composites: Investigation of toughening mechanism using optical and boundary element methods, Doctoral thesis and dissertation, Auburn University, 2006.
23. O'Toole B. J., Santare M. H., Photoelastic Investigation of Crack-inclusion Interaction, *Experimental Mechanics*, **30**(3), pp.253-257, 1990.

24. Li R., Wu S., Ivanova E., Chudnovsky A., Sehaobish K., and Bosnyak C.P., Finite Element Model and Experimental Analysis of Crack-Inclusion Interaction, *Journal of Applied Polymer Sciences*, **50**, pp.1233-1238, 1993.
25. Easley T. C., Faber K. T., Shah S. P., Moiré interferometry analysis of fiber debonding, *Journal of Engineering Mechanics*, **127**, pp.625-629, 2001.
26. Jaeger R. C., Introduction to Microelectronic Fabrication, Second Edition, Vol. 5, Prentice Hall, NJ, 2002.
27. Post D., Han B., Ifju P., High sensitivity moiré, Springer–Verlag, New York, 1994.
28. Post D. and Barakat W. A., High-sensitivity moiré interferometry – A simplified approach, *Exp. Mech.*, **21**(3), pp100-104, 1981.
29. Krishnamoorthy H., Estimation of fracture parameters in solder-copper joints using moiré interferometry, Master's thesis, Auburn University, 1997.
30. Tippur H., Optical methods in mechanics, Lecture notes, Auburn University, Spring 2005.
31. Chiang F. P., Doyle J. F., Phillips J. W., Manual on Experimental Stress Analysis, Society of Experimental Mechanics, Connecticut, 1989.
32. Williams M. L., On the stress distribution at the base of a stationary crack, *Journal of Applied Mechanics*, **24**, pp.109-104, 1957.
33. Rousseau C. –E., Tippur H. V., Influence of elastic gradient profiles on dynamically loaded functionally graded materials: Cracks along the gradient, *International Journal of Solids and Structures*, **38**, pp7839-7856, 2001.
34. Kirugulige M. S., Kitey R., Tippur H. V., Dynamic fracture behavior of model sandwich structures with functionally graded core: a feasibility study., *Composite Science and Technology*, **65**, pp1052-1068, 2005.
35. Al-Ostaz A., Jasiuk I., Crack initiation and propagation in materials with randomly distributed holes, *Engineering Fracture Mechanics*, **58**(5-6). pp.95-420, 1997.
36. Ko D., Kim B., Choi J., Finite-element simulation of the shear process using the element-kill method, *Journal of Materials Processing Technology*, **72**, pp.129-140, 1997.
37. ANSYSTM User's Manual (Ver.10). ANSYS Inc., Cannonsburg, PA.

APPENDICES

APPENDIX A

List of ANSYS APDL Macros

(1) Macro to generate the crack-inclusion interaction model. (TPB geometry)

```
!-----
!Modeling of 2D circular inclusion specimen with crack
!Global Cartesian coordinate system orientation: crack along x-axis
!-----
/com,structural
/prep7
csys,0
!-----
!   Parameters
!-----
a=8.5      ! Crack length in mm
d=3.8      ! Inclusion diameter in mm
r=d/2      ! Inclusion radius
e=5        ! Distance between inclusion center and crack tip
b=(e-r)/2  ! Tip quarter (square) zone dimension
bt=.01*d! Bonding layer thickness between inclusion and matrix
s=127      ! Span in mm
h=42.5     ! Height in mm
l=152      ! Specimen full length in mm
nw=0       ! Notch width in mm
!-----
!   MATERIAL LIBRARY
!-----
mpdel,all,all
!-----Inclusion property-----
mp,ex,1,68000 ! Young's modulus (Mpa)
mp,prxy,1,.19 ! Major Poisson's ratio
!-----Matrix property-----
mp,ex,2,3500 ! Young's modulus (Mpa)
mp,prxy,2,0.35 ! Major poisson's ratio
!----- Bonding layer property-----
mp,ex,3,3500 ! Young's modulus (MPa)
mp,prxy,3,0.35 ! Poisson's ratio
!-----End Material property definition---
!-----
!           ELEMENT TYPE
!-----
et,1,PLANE82 ! 8 noded iso parametric element
keyopt,1,3,3 ! Plane stress with thickness option
keyopt,itype,knum,value
keyopt,1,5,2 ! Nodal stress solution for extra element output
keyopt,1,6,0 ! Extra surface output as basic element solution
R,1,7.1 ! Real constant set definition
!-----
!   Crack tip Geometry
!-----
k,1,0,0 ! Crack tip zone keypoint definition
k,2,-b,-nw/2 ! k,npt,x,y,z (Npt= kp#, x,y,z(cartesian) or r, q, z
(cylindrical) etc..
```

```

k,3,-b,-b
k,4,0,-b
k,5,b,-b
k,6,b,0
k,7,b,b
k,8,0,b
k,9,-b,b
k,10,-b,nw/2
lstr,1,2 ! (1) !lstr,P1,P2
lstr,1,4 ! (2)
lstr,1,6 ! (3)
lstr,1,8 ! (4)
lstr,1,10 ! (5)
lstr,6,5 ! (6)
lstr,6,7 ! (7)
lstr,8,7 ! (8)
lstr,8,9 ! (9)
lstr,10,9 ! (10)
lstr,2,3 ! (11)
lstr,4,3 ! (12)
lstr,4,5 ! (13)
!-----
!Inclusion geometry
!-----
k,11,e,0 ! center of inclusion
k,12,(e-r),0 ! bottom point
k,13,e,-r ! right point
k,14,(e+r),0 ! top point
k,15,e,r ! left point
k,16,(e-r-bt),0 ! bonding layer bottom point
k,17,e,-(r+bt) ! bonding layer right point
k,18,(e+r+bt),0 ! bonding layer top point
k,19,e,(r+bt) ! bonding layer left point
! inclusion arcs.....
larc,12,13,11,r ! (14)! larc,P1,P2,PC,rad
larc,13,14,11,r ! (15)
larc,14,15,11,r ! (16)
larc,15,12,11,r ! (17)
!bonding layer arcs....
larc,16,17,11,(r+bt) ! (18) ! larc,P1,P2,PC,rad
larc,17,18,11,(r+bt) ! (19)
larc,18,19,11,(r+bt) ! (20)
larc,19,16,11,(r+bt) !(21)

lstr,12,16 ! (22)
lstr,13,17 !(23)
lstr,14,18 ! (24)
lstr,15,19 ! (25)
!-----
! Specimen overall geometry
!-----
k,20,-a,-nw/2 ! crack mouth right(top) side
k,21,-a,-s/2 ! bottom right
k,22,h-a,-s/2 ! top right
k,23,h-a,s/2 ! top left

```

```

k,24,-a,s/2    ! bottom left
k,25,-a,nw/2   ! crack mouth left(bottom) side
k,26,h-a,0     ! load point for TPB

lstr,2,20 ! (26)
lstr,10,25 ! (27)
lstr,20,21 ! (28)
lstr,25,24 ! (29)
lstr,21,22 ! (30)
lstr,24,23 ! (31)
lstr,26,23 ! (32)
lstr,26,22 ! (33)
lstr,18,26 ! (34) line joining bonding layer to load point
lstr,6,16  ! (35) line joining tip area to bonding layer

!-----
! Extended specimen from supports
!-----
k,27,-a,l/2    ! bottom leftmost
k,28,h-a,l/2   ! top leftmost
k,29,-a,-l/2   ! bottom rightmost
k,30,h-a,-l/2  ! top rightmost

lstr,24,27 ! (L36)
lstr,27,28 ! (L37)
lstr,23,28 ! (L38)
lstr,21,29 ! (L39)
lstr,29,30 ! (L40)
lstr,22,30 ! (L41)

! Dividing inclusion into 4 parts
lstr,12,11 ! (42)
lstr,13,11 ! (43)
lstr,14,11 ! (44)
lstr,15,11 ! (45)
!
a,1,2,3,4 ! (A1)
a,1,4,5,6 ! (A2)
a,1,6,7,8 ! (A3)
a,1,8,9,10 ! (A4)
!al,14,15,16,17 ! (A5) inclusion area
al,14,23,18,22 ! (A5) bottom right bonding layer segment
al,15,23,19,24 ! (A6) top right bonding layer segment
al,16,24,20,25 ! (A7) top left bonding layer segment
al,17,22,21,25 ! (A8) bottom left bonding layer segment
! Inclusion areas
al,42,14,43 ! A9(inclusion bottom right)
al,43,15,44 ! A10(inclusion top right)
al,44,16,45 ! A11(inclusion top left)
al,45,17,42 ! A12(inclusion bottom left)
a,10,9,8,7,6,16,19,18,26,23,24,25 ! (A13) left half
a,2,20,21,22,26,18,17,16,6,5,4,3 ! (A14) right half
al,36,37,38,31 ! (A15) left extended specimen
al,30,39,40,41 ! (A16) right extended specimen

```

```

!-----End of Gometry definition-----

!----- Element attributes to selected unmeshed areas-----
! AATT,mat,real,type,esys,secn
asel,all
asel,s,area,,9,12,1 !inclusion
aatt,1,1,1,0
allsel,all
asel,s,area,,5,8,1 ! Bonding layers
aatt,3,1,1,0
allsel,all
asel,u,area,,5,12,1 ! selection of martix areas
aatt,2,1,1,0
allsel,all
!-----End of area attributes-----

!*****
!***** MESHING *****
!*****

!-----
! Line seeding
!-----
!LESIZE,NL1,SIZE,ANGSIZ,NDIV,SPACE,KFORC,LAYER1,LAYER2,KYNDIV
!NL1=numberof line to be modified, can be ALL or P for graphical
picking
!SIZE=if NDIV is is blank, size is division (element edge) length. if
size is zero(or blank),
! use ANGSIZ or NDIV
!ANGSIZ=the division arc ( in degrees) spanned by the element edge.
!NDIV=if positive,NDIV is the number of element divisions per line.
!SPACE=Spacing ratio. If positive, nominal ratio of last division size
to first division size.
! (if > 1.0, sizes increase,if <1.0, sizes decrease)
!KFORC

!Tip-zone seeding
nd1=20
sr1=3
lesize,1,,nd1,sr1
lesize,2,,nd1,sr1
lesize,3,,nd1,sr1
lesize,4,,nd1,sr1
lesize,5,,nd1,sr1

lesize,8,,nd1,1
lesize,7,,nd1,1
lesize,6,,nd1,1
lesize,13,,nd1,1
lesize,12,,nd1,1
lesize,11,,nd1,1
lesize,10,,nd1,1
lesize,9,,nd1,1
type,1

```

```

real,1
mshape,0,2d
amesh,1,4,1

!inclusion and bonding layer seeding
nd2=58 ! number of divisions
lesize,14,,,nd2,1
lesize,15,,,nd2,1
lesize,16,,,nd2,1
lesize,17,,,nd2,1
lesize,18,,,nd2,1
lesize,19,,,nd2,1
lesize,20,,,nd2,1
lesize,21,,,nd2,1
lesize,22,,,1,1
lesize,23,,,1,1
lesize,24,,,1,1
lesize,25,,,1,1
! seeding of lines inside inclusion
ndinclu=12
srinclu=10
lesize,42,,,ndinclu,srinclu
lesize,43,,,ndinclu,srinclu
lesize,44,,,ndinclu,srinclu
lesize,45,,,ndinclu,srinclu
type,1
real,1
mshape,0,2d ! 0 = quadrilateral, 1= trianglular, and 2d = area mesh,
3d= volume mesh
amesh,5,12,1
!( 4 bonding layer 5-8 + 4 inclusion 9-12 areas)

!seeding line joining bonding layer and tip zone
lesize,34,,,50,25 ! inclusion top to top of specimen
lesize,35,,,30,1 ! crack tip zone to inclusion

!seeding line on top edge left and top right
lesize,32,,,30,3
lesize,33,,,30,3

!seeding of bottom left and bottom right lines joined to crack mouth
lesize,29,,,30,3
lesize,28,,,30,3

!seeding of crack flanks
lesize,26,,,30,10
lesize,27,,,30,10

!seeding right and left vertical edges near to supports
lesize,31,,,18,1
lesize,30,,,18,1

! meshing left and right half matrix areas
type,1
real,1

```



```

mshape,0,2d
amesh,13,14,1

!mesing extended parts # 12 & 13
lesize,37,,,18,1 !left most edge
lesize,40,,,18,1 ! right most edge
lesize,38,,,5,1 !left top
lesize,36,,,5,1 ! left bottom
lesize,41,,,5,1 ! right top
lesize,39,,,5,1 ! right bottom
type,1
real,1
amesh,15,16,1
!*****
!      End of seeding+ meshing
!*****

!-----
!      CONSTRAINTS
!-----
ddel,all,all
nselect,s,loc,x,-a,-a
nselect,r,loc,y,-s/2,-s/2
d,all,ux
!d,all,uy
allselect,all
nselect,s,loc,x,-a,-a
nselect,r,loc,y,s/2,s/2
d,all,ux
d,all,uy
allselect,all
!-----END Constraints-----
save,inclu2,db,all
finish
!
!*****
!***** SOLUTION PROC *****
!*****
/solu
allselect,all
!
!---cylindrical coordinate system for bonding layer elements-----
allselect,all
cskip,21,1,11,14,19
csys,21
dsys,21
nselect,s,loc,x,(d/2+.001),(d/2+bt-.001) ! regard x here as r coordinate
csys,0
dsys,0
nplo
esln,s,0 ! 0=select ele if any of its node is selected set, 1=only if
all nodes are in set
eplo      ! plot selected elements
!
!
```

```

!***** ARRAY and variables NAMES EXPLANATION*****
! NAME          ATTRIBUTE
! e_count      -    total number of elements in bonding layer
! e_list       -    array containing all bonding layer element numbers
! k_list       -    array to store killed element numbers
!*****END ARRAY EXPLANATION*****
!----WRITE ALL BONDING LAYER ELEMENT NUMBERS IN ARRAY e_list-----
cm,e_fail,elem    ! Making a componenet of selected bl element
*get,e_count,elem,0,count ! counting number of selected elements
*dim,e_list,,1,e_count
*do,i,1,e_count,1
    *get,e_list(1,i),elem,0,num,min
    e_min=e_list(1,i)!dummy variable to unselect last element
    esel,u,,e_min    !unselect last element from the set
*enddo
allsel,all
!-----writing complete-----
*dim,k_list,,100,80 ! Define array to store killed element numbers
*dim,ek_aray,,100,80! Write all to be killed element in an array
list=1 !dummy variable initiation for later storing of killed element
list
!*****
!***** Application of load and solving *****
!*****
!-----selecting node to apply load at-----
allsel,all
ksel,s,loc,x,h-a,h-a
ksel,r,loc,y,0,0
nslk,r
*get,l_pn,node,0,num,max    ! Variable 'load_pointnode' stores load
application node num.
allsel,all
eplo
!-----
!           Solution Parameters and solving methods
!-----
/solu
nlgeom,on    ! Nonlinear geometry on
nropt,full  ! Newton-Raphson full
solcontrol,off ! no auto time stepping
outres,all,all
autots,0
!*****

```

(2) Solution macro.

```

!-----
!           ANSYS MACRO FOR CRACK PARTICLE INTERACTION SIMULATION
!-----
/prep7
allsel,all
fdel,all    ! Delete all previously defined force
!---cylindrical coordinate system for bonding layer elements-----
allsel,all
cskp,21,1,11,14,19
csys,21

```

```

dsys,21
nsel,s,loc,x,(d/2+.001),(d/2+bt-.001) ! regard x here as r coordinate
csys,0
dsys,0
nplo
esln,s,0 ! 0=select ele if any of its node is selected set, 1=only if
all nodes are in set
eplo      ! plot selected elements
nodeset
cm,e_fail,elem ! Writing the selected element set into a component
*get,e_cou,elem,0,count ! Counting number of selected elements
*dim,e_aray,,8,e_cou      !Writing selected bonding layer element
numbers in an array
*do,i,1,e_cou,1
    *get,e_aray(1,i),elem,0,num,min
    e_min=e_aray(1,i)
    esel,u,,,e_min
*enddo
allsel,all
/solu
ddel,all,uy
!-----
!           CONSTRAINTS
!-----
ddel,all,all
nsel,s,loc,x,-a,-a
nsel,r,loc,y,-s/2,-s/2
d,all,ux
!d,all,uy
allsel,all
nsel,s,loc,x,-a,-a
nsel,r,loc,y,s/2,s/2
d,all,ux
d,all,uy
allsel,all
!-----END Constraints-----
!-----
!           DEFINING FORCE HISTORY TABLE
!-----
*dim,force1,table,18,1 ! Defining load history table step 1-18
*dim,force2,table,18,1 ! Defining load history table step 19-36
*dim,force3,table,18,1 ! Defining load history table step 37-54
*dim,force4,table,18,1 ! Defining load history table step 55-62
force1(1,1)=-1,-20,-40,-60,-80,-100,-120,-140,-160,-180,-200,-220,-
240,-260,-280,-300,-320,-340
force1(1,0)=1,2,3,4,5,6,7,8,9,10,11,12,13,14,15,16,17,18
force2(1,1)=-360,-380,-400,-420,-440,-460,-480,-500,-520,-540,-560,-
580,-600,-620,-640,-660,-680,-700
force2(1,0)=19,20,21,22,23,24,25,26,27,28,29,30,31,32,33,34,35,36
force3(1,1)=-720,-740,-760,-780,-800,-820,-840,-860,-880,-900,-920,-
940,-960,-980,-1000,-1020,-1040,-1060
force3(1,0)=37,38,39,40,41,42,43,44,45,46,47,48,49,50,51,52,53,54
force4(1,1)=-1080,-1100,-1120,-1140,-1160,-1180,-1200,-1220,-1240,-
1260,-1280,-1300
force4(1,0)=55,56,57,58,59,60,61,62,63,64,65,66

```

```

!-----End force history definition-----
!
nlgeom,on      ! Nonlinear geometry on
nropt,full    ! Newton-Raphson full
outres,all,all
*dim,killed_list,,200,200 ! Define array to store killed element
numbers
list=1!Initiating the array dimension variable defined in previous line
*dim,e_killarray,,70,150! Write all to be killed element in an array

tm_start=1      ! Start time ( must be >0)
tm_end=66       ! End time  of the fictitious static time scale of load
application
tm_incr=1       ! Time increment
*do,tm,tm_start,tm_end,tm_incr !Do for tm from tm_start t tm_end in
  *if,tm,eq,1,then           ! steps of tm_incr
  *c fopen,time_ch,txt,,append
  *c fwrite,time1=tm
  *c fclose
  antype,0,new              ! Start new analysis if first time step
  *else
  *c fopen,time_ch,txt,,append
  *c fwrite,time_b=tm
  *c fclose
  antype,0,rest! Restart if subsequent timesteps
  *c fopen,time_ch,txt,,append
  *c fwrite,time_a=tm
  *c fclose
  *endif

  /solu
  time,tm                  ! Time value
  Force application during subsequent loadsteps...
  *if,tm,le,18,then
    f,l_pn,fx,force1(tm)   ! Time-varying force
  *elseif,tm,le,36,then
    f,l_pn,fx,force2(tm)
  *elseif,tm,le,54,then
    f,l_pn,fx,force3(tm)
  *else
    f,l_pn,fx,force4(tm)
  *endif
  allsel,all
  solve
  /post1
!-----
!killing seected element on inclusion-matrix interface
!-----
  allsel,all
  rsys,21
  cmsel,s,e_fail,elem ! Select the bonding layer element set component
  etable,s_rr,s,x      ! Read the radial stress for those elements
  esel,r,etab,s_rr,9 ! Reselect element with SEQV >9
  *get,ekill_count,elem,0,count ! Count reselected elements
  *do,k,1,ekill_count,1
    *if,k,eq,1,then

```

```

        *get,e_n,elem,0,num,max
        e_killarray(1,k)=e_n
        e_high=e_n
    *else
        *get,e_n,elem,e_high,nxth
        e_killarray(1,k)=e_n
        e_high=e_n
    *endif
*enddo
/solu
*cfopen,deactive_elem,txt,,append
*cfwrite,t_step=tm
*cfwrite,tot_tokil=ekill_count
*cfclos
*do,kil,1,ekill_count,1 !Do for killing the elements in e_killarray
    ekill,e_killarray(1,kil)
    *cfopen,deactive_elem,txt,,append
    *cfwrite,kiled_elem=e_killarray(1,kil)
    *cfclos

    killed_list(list,kil)=e_killarray(1,kil)!Populating killed list
*enddo
estif,1e-8
allsel,all
!-----
!End of interface element killing
!-----
    allsel,all
    list=list+1
    esel,all

    /post1
    rsys,0
    allsel,all          ! Post time-step analysis to kill elements
    set,last            ! bonding layer
    /device,vector,1
    /contour,,128,-.375276,.002964,.004154
    plnsol,u,y
    /solu
*enddo

```

(3) Macro to calculate and store crack mouth opening displacements.

```

/post1
!--SELECTIONG CRACK MOUTH TOP AND BOTTOM NODES TO CALCULATE CMOD----
!-----selection of node from line number----
allsel,all
lssel,s,line,,27
allsel,below,line
nsl1,s,1
nssel,r,loc,x,-a,-a
*get,kf_top,node,0,num,max    !crack flank top node.
allsel,all
lssel,s,line,,26
allsel,below,line

```

```

allsel,below,line
nsl1,s,1
nsl,r,loc,x,-a,-a
*get,kf_bot,node,0,num,max !crack flank bottom node.
!-----end selection from line-----
!-----END SECECTION OF NODE FOR CMOD-----

```

```

n=66 ! Number of load steps
*do,setno,1,n,1
set,setno

```

```

!-----WRITING CMOD VALUES -----
*get,u21,node,kf_top,u,y
*get,u22,node,kf_bot,u,y
*cfopen,COD_VAL,txt,,append
COD=(u21-u22)*1000 ! COD in Micrometer
*cfwrite,cmod=cod
*cfclos
!-----END COD VALUES WRITING-----

```

(4) Macro to calculate mode – I stress intensity factors.

```

!Macro to calculate Mode 1 Stress intensity factor K1 from crack
!opening displacements using linear regression.

```

```

!Parameters:

```

```

E_epo=3500 ! Young's modulus in MPa

```

```

pi=3.142857

```

```

n_set=66 ! number of load steps

```

```

B=7.1 ! Specimen thickness

```

```

rb=0.5 ! r/B ratio limits

```

```

!End Parameters

```

```

/post1

```

```

allsel,all

```

```

!Writing node numbers of top crack flank

```

```

lsl,s,line,,5

```

```

lsl,a,line,,27

```

```

allsel,below,line

```

```

nsl1,s,1

```

```

cm,top_nod,node

```

```

*get,nt_cou,node,0,count

```

```

*dim,top_nodes,,8,nt_cou

```

```

!top_nodes(1,i)=x location of all nodes from tip to mouth

```

```

!top_nodes(2,i)=node numbers from tip to mouth

```

```

!top_nodes(3,1)=node opening displacement

```

```

*do,i,1,nt_cou,1

```

```

    *get,top_nodes(1,i),node,0,mxloc,x

```

```

    nod=node(top_nodes(1,i),0,0)

```

```

    top_nodes(2,i)=nod

```

```

    !*get,top_nodes(3,i),node,n,u,y

```

```

    nsl,u,node,,top_nodes(2,i)

```

```

*enddo

```

```

!Writing node numbers of bottom crack flank

```

```

lssel,s,line,,1
lssel,a,line,,26
allsel,below,line
nsl1,s,1
cm,bot_nod,node
*get,nb_cou,node,0,count
*dim,bot_nodes,,8,nt_cou
!bot_nodes(1,i)=x location of all nodes from tip to mouth
!bot_nodes(2,i)=node numbers from tip to mouth
!bot_nodes(3,1)=node opening displacement
*do,i,1,nb_cou,1
    *get,bot_nodes(1,i),node,0,mxloc,x
    nod=node(bot_nodes(1,i),0,0)
    bot_nodes(2,i)=nod
    !*get,bot_nodes(3,i),node,n,u,y
    nsel,u,node,,bot_nodes(2,i)
*enddo

! Limits of data to be considered for linear fit
*dim,klsif,,nt_cou
*dim,rsif,,nt_cou
*dim,aaa,,66
*dim,bbb,,66
!*dim,klsif,,8,count    ! K1 apperant for cropped range
!*dim,rsif,,8,count    ! radius data of cropped range

*do,setno,1,n_set,1
set,setno

x_max=a
x_min=rb*B
lim_cou=0
*do,jj,1,nt_cou,1
    cmsel,s,top_nod,node
    nsel,r,node,,top_nodes(2,jj)
    *get,top_nodes(3,jj),node,top_nodes(2,jj),u,y
    allsel,all
    cmsel,s,bot_nod,node
    nsel,r,node,,bot_nodes(2,jj)
    *get,bot_nodes(3,jj),node,bot_nodes(2,jj),u,y
    allsel,all
*enddo

*do,l,1,nt_cou,1
*if,abs(top_nodes(1,l)),gt,x_min,and,abs(top_nodes(1,l)),lt,x_max,then
    lim_cou=lim_cou+1
    *cfoopen,delta,txt,,append
    *cfwrite,del=top_nodes(3,1)-bot_nodes(3,1)
    *cfclos
    *cfoopen,r_value,txt,,append
    *cfwrite,r_val=abs(top_nodes(1,l))
    *cfclos
    klsif(lim_cou)=(E_epo*(top_nodes(3,1)-
bot_nodes(3,1))*sqrt(2*pi*0.001))/(8*sqrt(abs(top_nodes(1,l))))
    rsif(lim_cou)=abs(top_nodes(1,l))

```

```

        *else
          *cycle
        *endif
      *enddo

sigx=0.0 ! Initiation of values
sigy=0.0
sigxy=0.0
sigxx=0.0

*do,i,1,lim_cou,1
sigx=sigx+rsif(i)
sigy=sigy+klsif(i)
sigxy=sigxy+(rsif(i)*klsif(i))
sigxx=sigxx+(rsif(i)*rsif(i))
*enddo
aaa(setno)=((sigx*sigy)-(lim_cou*sigxy))/((sigx*sigx)-(lim_cou*sigxx))
bbb(setno)=(sigy-(aaa(setno)*sigx))/lim_cou
*cfopen,k1_fromuy,txt,,append
*cfwrite,SIF=bbb(setno)
*cfclos

*enddo

```

(5) Macro to write displacements, stresses and strains data in text files.

```

/post1
!n= number of sets for which results are to be written
! Path definition
! P3= on y=(e-r) between points (e-r,10), (e-r,-10)
padel,all
path,P3,2,30,100
ppath,1,,e-r,10,,0
ppath,2,,e-r,-10,,0
n=66
*cfopen,P3_data,txt,,append
*do,setno,1,n,1
*cfwrite,set=setno
set,setno
path,P3
pdef,exx_p3,epto,x,avg
pdef,eyy_p3,epto,y,avg
pdef,exy_p3,epto,xy,avg
pdef,sxx_p3,s,x,avg
pdef,syy_p3,s,y,avg
pdef,sxy_p3,s,xy,avg
paget,datap3_,table
! order in table array XG, YG, ZG, S, data1,data2,data3,.....
*do,m,1,1,1
*vwrite,datap3_(m,2),datap3_(m,5),datap3_(m,6),datap3_(m,7),datap3_(m,8)
,datap3_(m,9),datap3_(m,10)
(F9.5,' ',F15.8,' ',F15.8,' ',F15.8,' ',F9.3,' ',F9.3,' ',F9.3)
*enddo
*del,,prm_
*enddo
*cfclos

```


APPENDIX B

Analysis of uncracked beam with inclusion

To examine the effect of presence of crack on debonding of an inclusion in a beam specimen with same geometry as the experimental model was modeled and simulated. For completeness some of these results are presented here. Figure B.1 shows radial stress σ_r around the inclusion. The distribution is continuous before debonding and σ_r vanish upon debonding in the range of $\pm 80^\circ$ to $\pm 120^\circ$. Further, initiation of debonding in uncracked beam was at a comparably higher load as it can be seen from the plots of

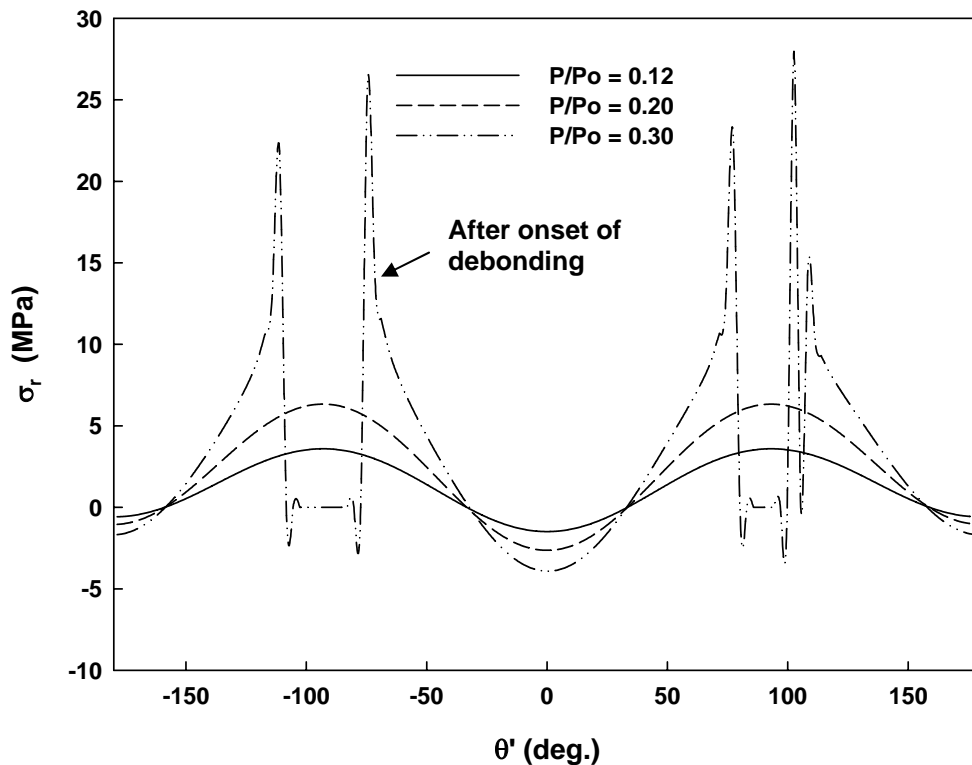


Figure B.1: Radial stress in the bond layer elements at different load levels.

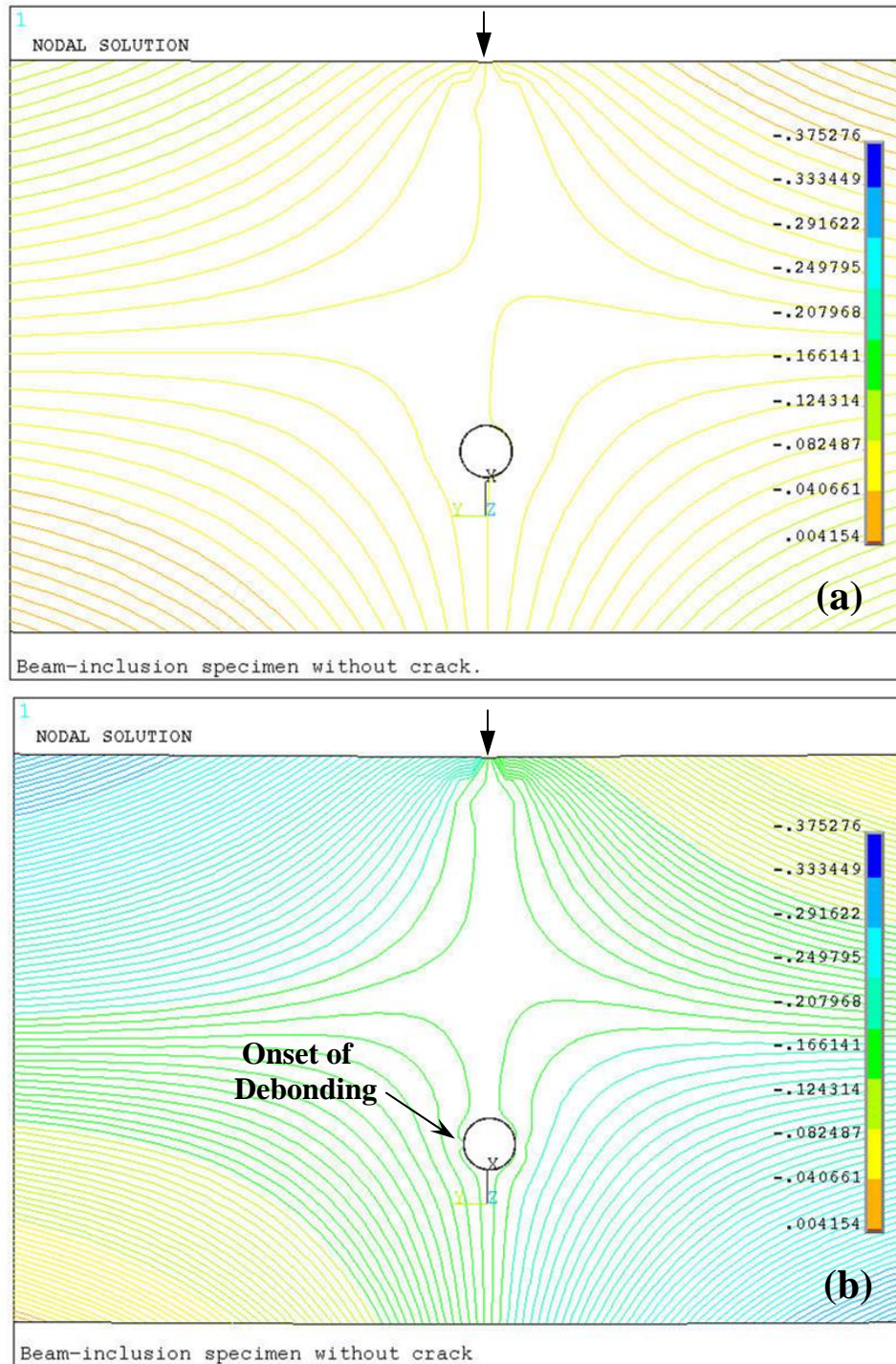


Figure B.2: Opening displacement field in uncracked beam with inclusion. (a) Before debonding ($P/P_o = 0.12$) (b) After onset of debonding ($P/P_o = 0.30$).

radial stresses in the bond layer elements in Fig. B.1. Stress intensification is evident where debonding occurs in the bonding layer and it can be seen in the radial stress plot. The opening displacement contours are shown in Fig. B.2(a) and (b) which corresponds to load levels of $(P/P_o = 0.12)$ and $(P/P_o = 0.3)$ respectively. Here, P_o is the load at which an uncracked neat epoxy beam would fail under tension based on ultimate strength of epoxy ($\sigma_o = 63$ MPa). Thus in the absence of crack debonding takes place much later in the loading phase and it is evident that a crack in the vicinity of the inclusion accelerates the process of debonding between an inclusion and matrix.